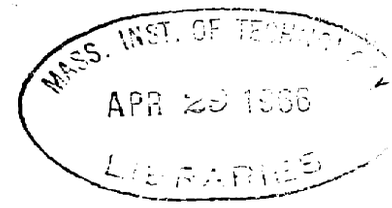

THE (α,p) REACTION ON NUCLEI IN THE $f_{7/2}$ SHELL

by

Robert O. Ginaven

B.A., Ohio Wesleyan University

(1961)

SUBMITTED IN PARTIAL FULFILLMENT

OF THE REQUIREMENTS FOR THE

DEGREE OF DOCTOR OF

PHILOSOPHY

at the

MASSACHUSETTS INSTITUTE OF

TECHNOLOGY

May, 1966

Signature of Author_____

Department of Physics, May 6, 1966

Certified by_____

Thesis Supervisor

Accepted by_____

Chairman, Departmental Committee

on Graduate Students

THE (α,p) REACTION ON NUCLEI IN THE $f_{7/2}$ SHELL

by

Robert O. Ginaven

Submitted to the Department of Physics on May 6, 1966
in partial fulfillment of the requirement for the degree of
Doctor of Philosophy

ABSTRACT

The (α,p) reaction on Ca^{40}, Ca^{42}, Ca^{44}, Ca^{48} and Ti^{48} has been investigated using 30.8 Mev alpha particles. The targets used were all isotopically enriched except Ca^{40} for which natural calcium was used. Proton spectra were recorded at 5 degree intervals between 20 and about 90 degrees, using a ΔE-E arrangement of solid state detectors. The overall resolution was about 150 kev FWHM. Differential cross-sections were obtained for transitions to the ground state and several excited states in each final nucleus. The differential cross-sections for the transitions to the ground states of Sc^{47}, Sc^{51} and V^{51} were measured in to 5 degrees using a gold absorber to stop the scattered alpha particles.

The five ground state (0+ to 7/2-) angular distributions observed were very similar in shape. For the transitions in which the neutrons as well as the proton can go into the f7/2 shell (all except $Ca^{48}(\alpha,p)Sc^{51}$) the shapes and the relative magnitudes were satisfactorily accounted for by DWBA calculations based on a stripping model for the (α,p) reaction. Details of the model and the DWBA calculations are presented.

The experimental (α,p) spectra (all except that for Sc^{51}) are compared to shell model calculations for pure f7/2 configurations. In going from Sc^{43} to V^{51} (i.e. as the f7/2 neutron shell fills), the main strength of the (α,p) reaction to excited states shifts from low lying levels to higher levels (above 2.4 Mev). The decrease in intensity of the low lying states is predicted by the shell model. However, the relatively large number of experimental states in Sc^{43} and Sc^{45} prevents detailed agreement. The implications of the present results concerning configuration mixing are discussed.

Based on DWBA fits to the (α,p) differential cross-sections, spin assignments are suggested for several excited states in each final nucleus. In particular, many strongly excited states are assigned spin and parity 3/2-.

The $d_{3/2}$ hole states in Sc^{43}, Sc^{45} and Sc^{47} were weakly excited by the (α,p) reaction, indicating that the dominant mechanism is stripping.

Three new levels in Sc^{51} are suggested at 1.36, 3.95, and 5.62 ± .05 Mev. Below 3.5 Mev excitation the $Ca^{48}(\alpha,p)Sc^{51}$ spectrum is qualitatively similar to that for the $Ca^{40}(\alpha,p)Sc^{43}$ reaction.

Thesis Supervisor: Aron M. Bernstein

Title: Assistant Professor of Physics

ACKNOWLEDGEMENTS

I am especially indebted to my thesis advisor, Professor Aron Bernstein, for suggesting this work and for many helpful discussions relating to the experimental results and their interpretation. After reading the first draft of this thesis, he made suggestions which led to many improvements in the final copy.

Dr. W. J. Kossler calculated the theoretical spectroscopic factors, and proof read this thesis. This assistance as well as many pertinent discussions throughout the course of this work is greatly appreciated. I also wish to thank Dr. P. G. Roos for assistance with many of the DWBA calculations.

Help with the application of the DWBA theory to the present results was obtained from Dr. B. Bayman, Dr. R. Bassel and Dr. R. Drisko, and is gratefully acknowledged. Dr. Bayman was especially helpful in explaining his (p,α) theory, and in performing some initial DWBA calculations. He also supplied us with a routine to calculate form factors for $f_{7/2}$ shell configurations.

The data analysis for this experiment was simplified by computer programs written by T. Provost, E. P. Lippincott and S. Smith. I am also grateful to E. P. Lippincott for his elastic alpha particle scattering results, and help in measuring the beam energy.

The competence of the M.I.T. Cyclotron Staff in maintaining the cyclotron and other experimental equipment was apparent throughout this experiment. For their help I wish to thank W. Bucelewicz, R. Burgess, J. Byrne, F. DesLauriers and especially, E. F. White and F. Fay.

For the first four years of my post-graduate education I received National Science Foundation graduate fellowships and I want to express my appreciation for this financial assistance.

I am very grateful to my wife for typing the rough draft of this thesis and to Mrs. Patricia Parkes for typing the final copy.

Most of the DWBA calculations for this work were carried out using the facilities of the M.I.T. Computation Center.

This dissertation is dedicated to my father.

CONTENTS

List of Figures

List of Tables

CHAPTER 1

INTRODUCTION

Single particle transfer reactions, especially the (d,p) reaction, have been used extensively in nuclear spectroscopy. Their usefulness is partially due to the fact that the angular distributions are often characteristic of the orbital angular momentum of the transferred particle. In addition, single particle transfer reactions are usually highly selective, and therefore, if the reaction mechanism is understood, information about nuclear wave functions can be obtained from the relative intensities of particle groups corresponding to different states in the final nucleus. The (d,p) reaction, for example, strongly populates only those states in the final nucleus that can be obtained by simply adding a neutron to the ground state of the target nucleus.

Both of the above attributes of single particle transfer reactions are dependent on their direct reaction character. Direct reaction theories, in particular the distorted wave Born approximation, have been quite successful in describing the angular distributions showing strong forward peaking characteristic of direct reaction processes. By fitting such angular distributions with DWBA calculations the transferred orbital angular momentum can often be determined. Sometimes, even the total angular momentum transfer can be determined from the shape and magnitude of the cross-section. The DWBA description of the $Ca^{40}(d,p)Ca^{41}$ reaction has been discussed by Lee et al. (L4).

In recent years, many reactions have been investigated in which more than one particle is transferred, including (α,p) and (p,α) reactions. Much of the earlier (α,p) work is summarized by Yamazaki, Kondo and Yamabe (Y3) and many references may be found in their paper. As indicated there,

several (α,p) and (α,n) reactions (e.g. on Be^9, C^{12}, Al^{27} and Si^{28} show considerable backward peaking and energy dependence at alpha energies as high as 15-18 Mev. At higher energies the cross-sections become forward peaked and vary slowly with energy, characteristic of direct reactions.

Similarly, angular distributions from the (p,α) reactions on F^{19}, Al^{27}, Mn^{55} and Co^{59} exhibit a pronounced energy dependence and the total cross-sections have resonances for proton energies below 10 or 11 Mev. At higher energies, their behavior is more consistent with a direct reaction mechanism.

Some (α,p) angular distributions for very light target nuclei (e.g. Li^6 and Li^7) show pronounced backward peaking at an alpha energy of 30 Mev (K2). This behavior suggests that heavy particle stripping may be important for light nuclei.

Compound nuclear (α,p) reactions on A^{40} and Ca^{40} with alpha particles of maximum energy 20 Mev, were studied by N. O. Lassen and Clive Larsen (L6 and L8). The main proton spectrum in each case was an evaporation spectrum. The spectra were approximately isotropic except for protons which left the final nucleus in its low lying energy levels. These protons had angular distributions which were strongly forward peaked, characteristic of direct reactions.

For alpha energies above 22 Mev and target nuclei heavier than F^{19}, (α,p) reactions to low lying excited states of the final nuclei show none of the pronounced backward peaking and energy dependence discussed above. A similar statement seems to hold for (p,α) reactions at proton energies of about 18 Mev and above. Because of the direct reaction nature of these higher energy (α,p) cross-sections, several attempts were made to fit them with plane wave Born approximation calculations (H4, L6, Y3), but in general the plane wave theory could not satisfactorily account for the

angular distributions.

DWBA calculations were carried out by B. F. Bayman and E. Rost to fit the $f_{7/2}$ shell (p,α) data of R. Sherr, F. P. Brady, H. O. Funsten and N. R. Roberson (S4). For the pickup mechanism they assumed that the incoming proton interacted with the center of mass of a triton cluster consisting of two neutrons coupled to spin zero and an $f_{7/2}$ proton. The cluster wave function was simplified by integrating out the relative coordinates of the product of three oscillator wave functions (for the picked up nucleons) and a simple alpha particle wave function. With this simplification and using the zero range approximation a standard DWBA code could be used. This model gave satisfactory fits to the $f_{7/2}$ shell (p,α) angular distributions. The above model is essentially the same as that presented in chapter 5 and used for the present (α,p) calculations except that, in the present case, the neutrons can couple to spins other than zero and spin orbit effects are included in the proton channel.

Using the DWBA calculations, Sherr et al. extracted relative spectroscopic factors from the observed cross-sections, and compared them to values calculated assuming separate neutron and proton seniority. Satisfactory agreement was obtained. The experimental cross-sections, at small angles, varied by a factor of about 100 over the range of targets studied, and the ratio to the calculated cross-section varied by about a factor of 4. The use of coupled spectroscopic factors (calculated assuming the neutrons and protons are coupled) for several nuclei reduced the spread slightly.

The pickup model also explains, the very weak ground state transition in the $Mn^{55}(p,\alpha)Cr^{52}$ reaction. The ground state spin of Mn^{55} is 5/2, and is thus assumed to have proton seniority, $v_p = 3$. The ground state of Cr^{52},

with an even number of protons, is assumed to have $v_p = 0$. However, a change in proton seniority of 3 is forbidden by the pickup model. A similar situation exists for the $Na^{23}(\alpha,p)Mg^{26}$ reaction, and the ground state transition is found to be quite weak (H4, Y3).

Thus, the pickup model has been quite successful in accounting for the ground state (p,α) reactions in the $f_{7/2}$ shell. The model was successful in accounting for some excited state transitions also. For example, the relative (p,α) cross-sections to the 2^+, 4^+ and 6^+ levels in Fe^{56} were in good agreement with predictions of the model.

Essentially the same model, but with spin orbit coupling in the proton channel, was applied to the reactions $Y^{89}(p,\alpha)Sr^{86}$ and $Zr^{90}(p,\alpha)Y^{87}$ at proton energies of 20.2 and 22.5 Mev by Fulmer and Ball (F2). They obtained good fits to $J\pi = \frac{1}{2}^-$ and $9/2^+$ angular distributions, and the relative intensities of the ground state transitions and the transition to the .38 Mev level in Y^{87} were found to be consistent with triton pickup as the dominant mechanism for these (p,α) reactions.

The inclusion of spin-orbit coupling in the proton optical potential causes a striking J dependence in the $L = 1$ (α,p) DWBA calculations. This J dependence has been discussed by Lee et al. (L5) who obtained qualitative agreement between the calculated cross-sections and those observed in (α,p) reactions on Ni^{58} and Ni^{60}. Specifically, the $3/2^-$ angular distributions showed a smooth variation with angle, while those for $J\pi = \frac{1}{2}^-$ showed pronounced oscillatory structure. Somewhat similar behavior was found for $L = 2$ transitions in the 1d shell, the $3/2^+$ angular distributions showing oscillations and the $5/2^+$ ones being smooth functions of angle. Much weaker J dependences were predicted for $L = 3$ transitions in the 1f shell and $L = 2$ transitions in the 2d shell. The pronounced J dependence of the $L = 1$ transitions suggests that the (α,p)

reaction may be particularly useful in assigning J values to states whose L = 1 character is known from other information (e.g. single particle transfer reactions).

The interpretation of the (α,p) reaction is potentially very complicated due to the fact that three particles are transferred. As pointed out by B. F. Bayman (B4), the (α,p) reaction is coherent in the single particle states of the three transferred nucleons. Even if all three nucleons enter the same shell, the reaction is still coherent in the angular momentum of the neutron pair. This coherence may be useful in that it makes the (α,p) reaction sensitive to the relative phases of the components of the wave functions involved (see section 5.4). The usefulness of the (α,p) reaction in determining signs of amplitudes in a wave function is, however, largely dependent on a knowledge of the magnitudes of the amplitudes from other information. Single particle transfer reactions, for example, are sensitive to the magnitudes but not the phases of the wave function amplitudes.

The present dissertation is a study, using the 30.8 Mev alpha particles, of the (α,p) reaction on the Ca isotopes of mass 40, 42, 44, 48 and Ti^{48} and thus the final nuclei are Sc isotopes 43, 45, 47, 51 and V^{51}. For all of these nuclei except Sc^{51}, energy levels and wave functions have been calculated, assuming pure $f_{7/2}$ shell configurations, by McCullen, Bayman, and Zamick (M1, hereafter referred to as MBZ). The agreement between the experimental and theoretical (MBZ) energy levels was very good for V^{51}, but rather poor for Sc^{43}, Sc^{45} and Sc^{47}. Specifically, there are many more low lying levels known in these nuclei than predicted by MBZ. This apparently indicates the participation of other configurations in the low lying states. Since the (α,p) spectroscopic factors to the $f_{7/2}$ shell states can be calculated (from the MBZ wave functions) a comparison

between these calculations and the experimental (α,p) spectra yields some information about the configuration mixing.

Very few spins and parities are known for states in Sc^{43}, Sc^{45} and Sc^{47}. One low lying state in each of these nuclei has been identified as a $d_{3/2}$ hole state (formed by promoting a $d_{3/2}$ proton to the $f_{7/2}$ shell) and thus these states have spin and parity $3/2+$ (H2). The relative intensities of the (α,p) reaction to these states compared with the ground state transitions yields information about the (α,p) reaction mechanism. For a stripping mechanism, in which a triton cluster is stripped from the incident alpha particle and captured by the target nucleus, the hole states can only be populated via a two particle-two hole admixture in the target ground state wave function. Such admixtures are sufficiently small that weak excitation of the hole states would be expected. However, for a knockout mechanism, in which the incident alpha particle interacts with a proton in the target, ejects it and is subsequently captured, there seems to be no reason why the hole states should not be strongly populated.

The DWBA model for (α,p) stripping reactions is presented in chapter 5. This is essentially the same as the model of B. F. Bayman and E. Rost, although spin-orbit coupling in the proton channel was used for the present calculations. No radial cutoff was used. Satisfactory fits were obtained for the ground state angular distributions, and several excited state spins were suggested on the basis of DWBA fits.

The (α,p) energy resolution in this experiment was about 150 kev FWHM. This resolution was made possible by recent improvements to the M.I.T. cyclotron and the availability of thick, high resolution solid state detectors. The main improvement to the cyclotron was the installation of a momentum analysing magnet in the beam handling system. This, and other improvements are described in chapter 2. The most important solid state

detectors were two 2.3 mm. thick surface barrier silicon transmission detectors each of which had a noise level (including electronics) of about 25 kev. These detectors were made by the Oak Ridge Technical Enterprises Corporation. The proton detection system, including these detectors, is described in chapter 3.

CHAPTER 2

CYCLOTRON AND ASSOCIATED EQUIPMENT

2.1 Cyclotron and Beam Handling System

The M.I.T. cyclotron and scattering room setup is shown in figure 2.1. The alpha beam was produced by accelerating doubly-ionized helium ions to about 30.7 Mev in the cyclotron (L1).

The beam was electrostatically deflected into the cyclotron target chamber where it was defined by a plate with a 3/8 inch high by 7/8 inch wide hole which allowed only the central portion of the beam to pass into the steering magnet (A in figure 2.1). This magnet deflected the beam horizontally, and was used to center the beam entering the bending magnet (B). The current through the steering magnet coil was set initially by centering the beam on a piece of plastic scintillator placed across the entrance to the bending magnet and viewed by a television camera wired to a monitor near the cyclotron console.

The first pair of quadrupole focusing magnets (Q1 and Q2) helped to counteract the divergence of the beam and the coil currents were adjusted to maximize the intensity of the beam entering the Faraday cup (with all magnets on).

The 30 degree bending magnet (B) served to create a momentum-position correlation at the slits (about 12 feet from B) so that the horizontal slits could be used to select a narrow range of momenta for the final beam. The vertical slits limited the height of the beam so that it would

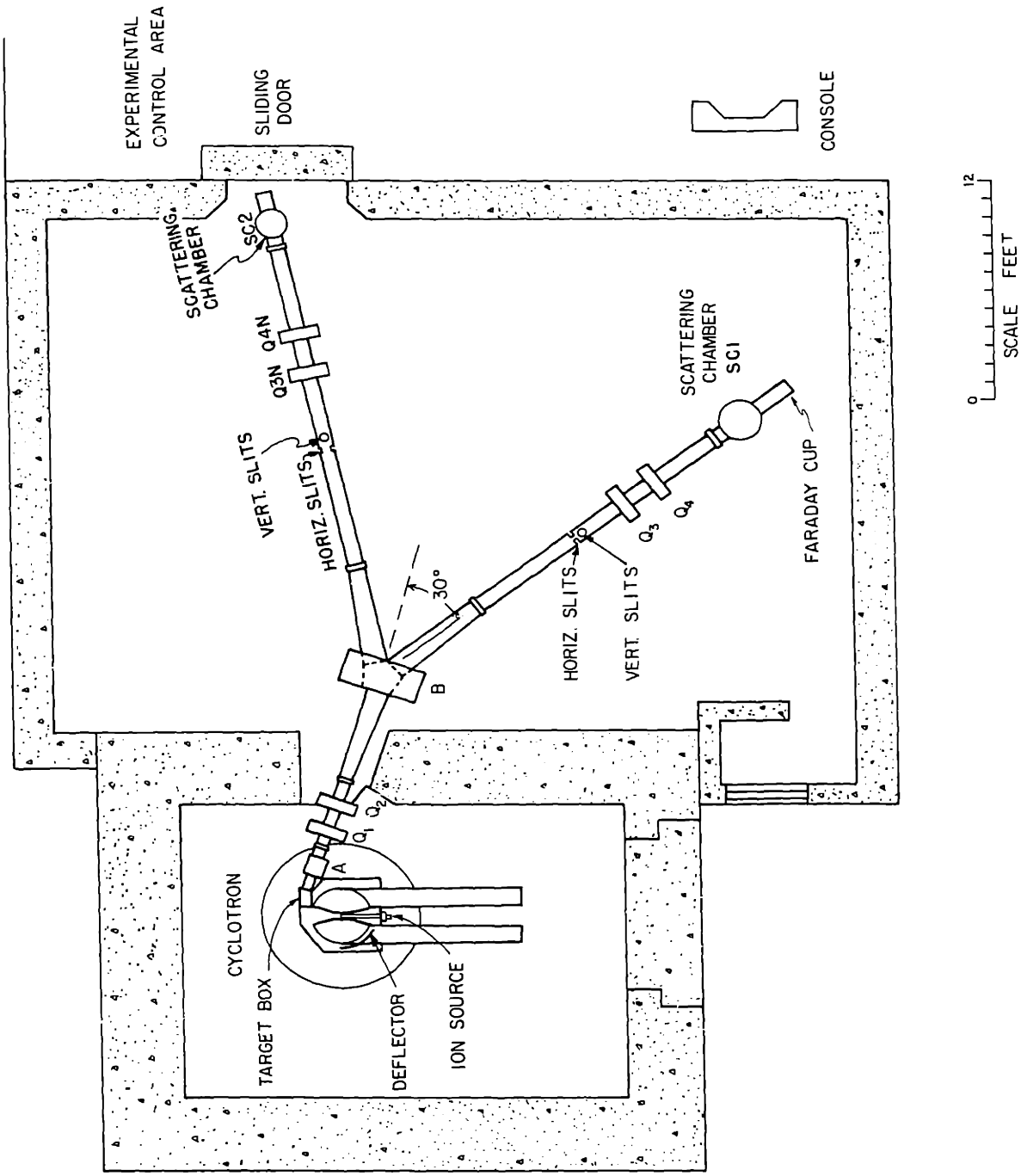

Figure 2.1 Cyclotron and Scattering Room Setup

not strike the beam pipe after the slits. Normally the separation of the vertical slits was about 0.5 inches and that of the horizontal slits was between .050 and .100 inches. With these settings the beam intensity was typically .10 to .15 microampere and the energy resolution (FWHM of the peak corresponding to alpha particles elastically scattered from a thin gold target) was about 80 kev.

The beam was focused on the target at the center of the scattering chamber (SC1) by the second pair of quadrupole magnets (Q3 and Q4). The coil currents for these magnets were adjusted to produce a well-focused beam on a piece of thin plastic scintillator (.005 inch thick Pilot B) placed in the target position and viewed by the television camera. With the slit setting described above the beam spot on target was usually about 1/8 inch wide and 1/2 inch high.

After passing through the scattering chamber, the beam stopped in a Faraday cup. The current striking the cup was measured by a sensitive microammeter (Keithley Model 610R) situated outside the scattering room near the experimental control area. A slave meter (monitoring the Keithley output) on the cyclotron console facilitated the adjustment of the cyclotron and beam handling system.

2.2 Scattering Chamber

The scattering chamber used in this experiment was basically the same as that described previously by Hunting (H1), but with several modifications most of which were related to the use of solid state particle detectors.

The chamber itself was a vertical cylinder with a 24 inch inside

diameter and a 22 inch inside height. Most of the walls consisted of thick transparent plexiglass windows, permitting observation of the contents of the chamber. The ability to see into the chamber was especially useful for adjusting the beam since the television camera, focused on a plastic scintillator placed in the target position, could view the beam spot directly.

The entire lid of the chamber was easily removed for access to the inside of the chamber. Figure 2.2 shows the scattering chamber, with the top removed. The Faraday cup opening can be seen just to the right of the center of the photograph. The two moveable counter arms are shown, the one on the near side of the beam holding the proton detection system (described later in Chapter 3). The target holder is shown at the left-hand side of the picture. The target support held four 1 1/8 inch square target frames any one of which could be positioned in the beam remotely by means of a hydraulic system. The scintillator used to view the beam was placed in the lowest target position. The one-sided target support (shown also in figure 2.3) was specially built to allow detection of protons leaving the target at the grazing angles necessary for optimum resolution for the (α,p) reaction (see section 4.3). To facilitate remote control of the target angle, a variable speed target rotation motor and an improved angle readout system (see below) were installed.

In the center of the top of the scattering chamber was a $2\frac{1}{2}$ inch diameter hole which was normally covered by a bell jar. For changing targets, the hydraulic system could push the target post up to the top of the chamber, where an O-ring around the base of the target support sealed the hole in the chamber lid and the target support extended into the bell jar.

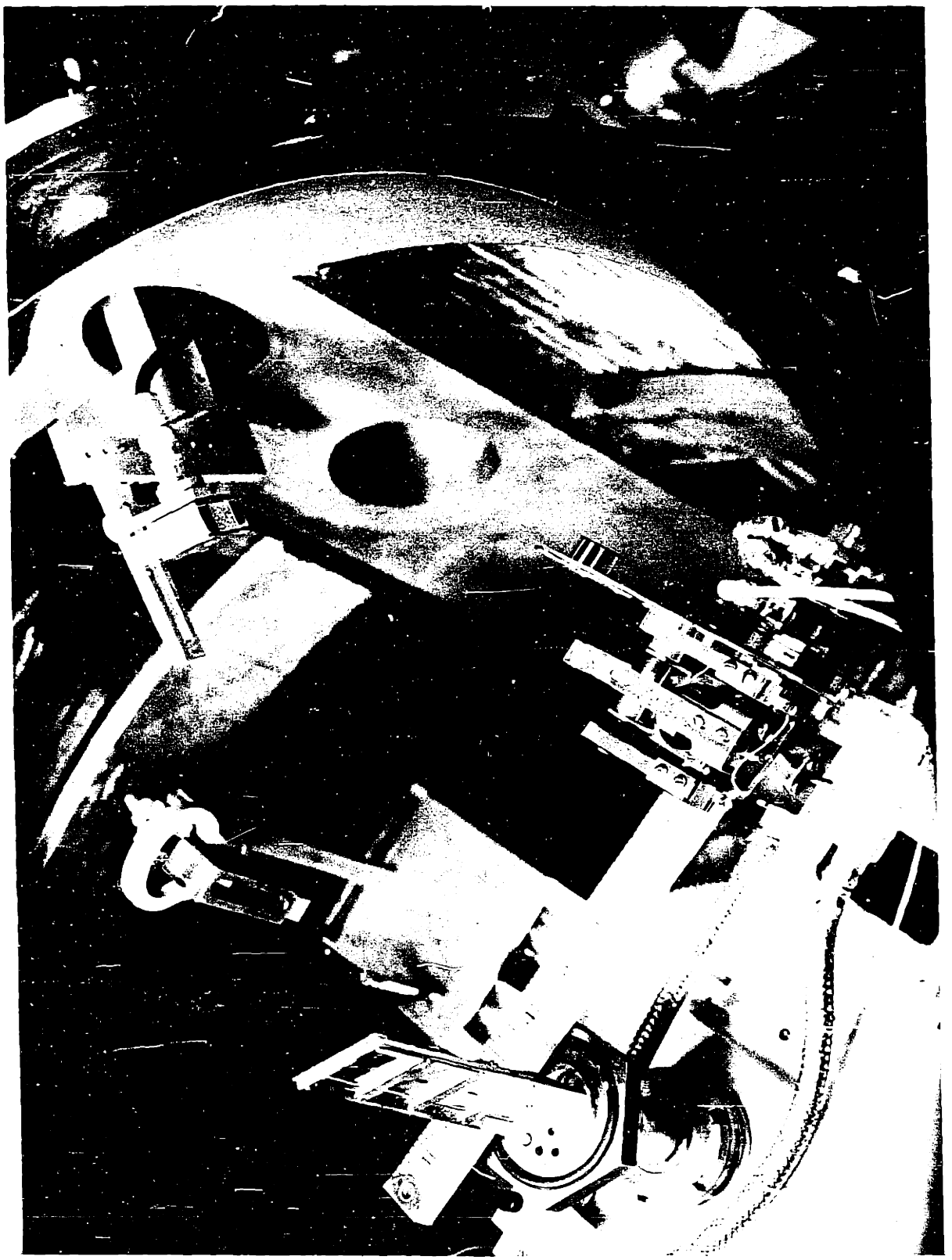

Figure 2.2 Inside the Scattering Chamber

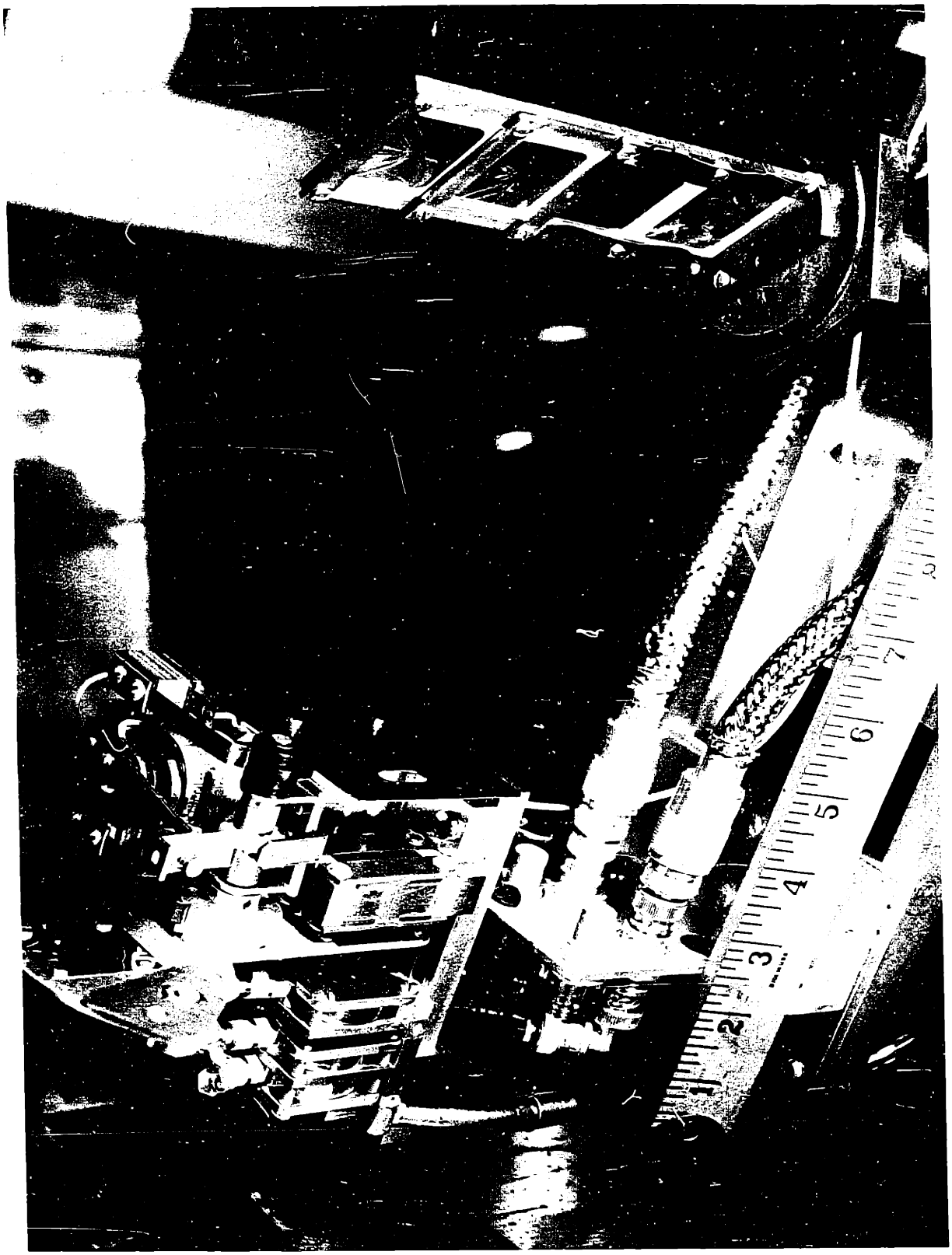

Figure 2.3 Proton Detector System

Thus, the targets could be changed without disturbing the vacuum in the main chamber.

Target selection, rotation of target, and rotation of counters could be accomplished from either a panel mounted near the scattering chamber or a remote panel mounted outside the scattering room in the experimental control area. In addition, the two counter angles and the target angle could be determined from the remote panel by three helipot bridge circuits. Recently, the angle readout system was improved by the addition of anti-backlash gears driving the sensing helipots, and improved linearity helipots: .05 per cent linearity on both counter arms, and 0.1 per cent linearity on the target. Thus the counter angles could be determined to within about 0.2 degrees and the target angle to within about 0.4 degrees.

Two counters were used to monitor the alpha particles elastically scattered by the target. They were both surface barrier type silicon solid state detectors with 0.5 mm depletion depths. One monitor counter was mounted vertically above the entrance to the Faraday cup (see figure 2.2) and could be set (with chamber open) in one of ten possible positions corresponding to scattering angles between 19 and 37 degrees in two degree steps. The other monitor was mounted on one of the moveable arms.

Since oil is detrimental to targets and detectors, several additional improvements were added to reduce the amount of oil vapor in the scattering chamber. Near the vacuum pumps two traps were installed. The first, a cold trap, was placed between the oil diffusion pump and the chamber, and was cooled to about -40° C by a mechanical refrigeration system. The second trap was a molecular sieve type and was inserted in the line to the mechanical pump which was used for roughing as well as backing the

diffusion pump.

To trap any oil vapor which did get into the chamber a liquid-nitrogen cooled circular plate was suspended from the top of the chamber. This copper plate was covered with aluminum foil which reduced absorbtion of heat by the plate, and collected any oil which condensed. This foil covering was replaced when the chamber was opened. Besides trapping oil vapor, this plate also greatly improved the vacuum in the scattering chamber and shortened the pump-down time. These last two benefits were not unexpected since the plate, when cold, acts as a very efficient trap for water vapor.

Using the same refrigeration system that cooled the diffusion pump baffle (described above) a system was set up to cool the proton detectors. Alcohol was cooled to about -20° and circulated through the copper detector mount by a small electric pump. Inside the chamber the alcohol flowed through Tygon tubing which was flexible enough to allow the detector to rotate. Cooling the detectors reduced their leakage currents and improved their resolution (see section 3.2).

CHAPTER 3

PROTON DETECTION SYSTEM

3.1 Proton Identification

The method of proton identification used in this experiment was very simple. A transmission (ΔE) detector was used in front of a thick (E) detector. The ΔE detector was thick enough to stop the scattered alpha particles, and so only protons, deutrons, tritons and He^3 particles reach the E detector, and of these the protons (of interest in this experiment) had considerably more energy than the other particles. The Q values for the pertinent reactions are listed in table 3.1. Based on these Q values the energy differences between the (α,p) ground state proton group and the ground state groups from different reactions were calculated. These energy differences are given in table 3.2 for the five targets used in the experiment.

The rate of ionization energy loss $(-dE/dx)$ for charged particles varies roughly as mz^2/E, where m is the mass of the particle, z is its charge, and E its energy. Thus the heavier (and lower energy) particles were separated even further from the protons after passing through the ΔE detector. In the experiment, the protons were identified by their relatively large energy loss in the E detector (see section 3.3).

3.2 Detector System

As shown in figure 2.3, the detector system (solid state detectors,

TARGET	PRODUCT PARTICLE(S)					
	Proton	Deuteron	Triton	He^3	2p	α + p
C^{12}	-4.965*	-13.57	-17.87	-15.63	-15.17	-15.96
Ca^{40}	-3.470*	-13.00	-18.18	-12.22	- 8.46	- 8.34
Ca^{42}	-2.343*	-11.44	-14.89	-12.65	- 9.23	-10.28
Ca^{44}	-1.988	-10.42	-12.92	-13.16	-10.48	-12.17
Ca^{48}	-5.860**	- 9.80	-10.26	-15.43		
Ti^{48}	-1.162*	- 9.98	-13.06	-12.43	- 9.21	-11.44

All Q values (in Mev) taken from reference N2 except:

* From: Tl

** From: El

Table 3.1

Q Values of Alpha Induced Reactions

TARGET	Ca^{40}	Ca^{42}	Ca^{44}	Ca^{48}	Ti^{48}
Ep	26.28	27.44	27.84	23.96	28.76
Ep-Ed	9.42	8.94	8.25	3.68	8.66
Ep-Et	14.60	12.28	10.62	3.96	11.62
Ep-EHe^3	8.38	9.96	10.86	9.36	10.10
Ep-E2p	5.13	7.06	8.69		8.20
Ep-Eαp	5.00	8.14	10.42		10.48

All energies are in Mev

Ex = Energy of particle x from the (α,x) reaction

E2p = Maximum Energy of protons from the (α,2p) reaction

Eαp = Maximum Energy of protons from the (α,αp) reaction

Table 3.2

Energies of Alpha Induced Reactions at 20 degrees

absorber wheel, and slits) was mounted on one of the moveable arms in the scattering chamber.

At the end nearest the target the system was shielded by a .015 inch thick tantalum plate with a 1/4 inch by 1/2 inch hole in the center. This plate was to insure that only particles coming from the direction of the target and passing through the slits would enter the detectors.

To avoid edge effects in the detectors, a slit system was placed between the detectors and the target. The slits consisted of two rectangular apertures formed by pieces of 1/16 inch lead sheet. The aperture nearest the target was .140 inches by .250 inches and served to define that portion of the detector which could "see" the target. The center of the target was 7.5 inches from this slit and so the angular acceptance in the plane of scattering was 1.07 degrees and the solid angle subtended was 6.2×10^{-4} steradians. The second slit, 1/2 inch behind the first, was .166 inches by .308 inches and served to stop many of the particles which had been scattered by or had penetrated the edge of the first slit.

Between the slits and the detectors was a wheel which could be remotely advanced to any one of eight possible positions. For this experiment the wheel held:

(1) Th^{228} alpha source, to check the extent of the depletion region in the ΔE detector. Since this detector had its "back" face towards the target, a thin dead layer on this side meant that the detector was fully depleted. The dead layer was checked by the resolution of the lower energy peaks in the Th^{228} spectrum.

(2) Bi^{207} conversion electron source, with its .972 Mev and 1.044 Mev lines provided a fast determination of the beta resolution (noise) of

the detection system.

(3) Au absorber thick enough (284 mg/cm^2) to stop the scattered alpha particles. This absorber was used for proton detection at small angles (less than 15 degrees) where the intensity of the scattered alpha particles made the use of the normal system impossible. Gold was used since it would not melt when struck by the direct beam, and also because its high coulomb barrier for alpha particles resulted in low cross-sections for α-induced reactions in the absorber.

The detectors used in this experiment were fully depleted silicon surface barrier solid state detectors manufactured by the Oak Ridge Technical Enterprises Corporation (ORTEC). The detectors were held in identical transmission type mounts and each had an active area of 100 sq. mm. Other details on the detectors are given in table 3.3.

The 0.5 mm detector was used as the ΔE detector for all spectra except $Ti^{48}(\alpha,p)\ V^{51}$ at angles less than 35 degrees. For this case the 1.0 mm detector was required so that the ground state proton group would stop in the E detector. The E detector itself consisted of the two 2.3 mm detectors connected to the same preamplifier and bias voltage supply. Thus, with the .5 mm ΔE detector the total detector thickness was 5.1 mm, capable of stopping protons with an energy of about 29 Mev, and with the 1.0 mm ΔE detector the total thickness of 5.6 mm could stop protons with an energy of about 30.5 Mev.

The ΔE detector and the first half of the E detector were placed so that the side towards the target was the one with the thickest dead layer. This orientation had two advantages:

1.) The thicker dead layers were crossed by higher energy protons

Model Number	TMEJ 100 -500	TMDJ 100 -1000	TMEJ 100 -2000	TMEJ 100 -2000
Serial Number	3-357F	5-774	4-552B	4-550B
Depletion Depth (Microns)	505	1025	2300	2320
Bias Voltage (Volts)	190	400*	400	400
Reverse Current (μamp)	.78	.46	.91	1.09
Electron** Resolution (kev FWHM)	20	25	25	25

*400 volts was specified by ORTEC. 500 volts was required to fully deplete the detector.

**Measured with conversion electron sources: Ba^{133} for 505 and 1025 micron detectors and Bi^{207} for thicker detectors.

Table 3.3

Detector Data

than the thin ones, thus minimizing the energy lost in the insensitive portions of the detector.

2.) Since the detectors depleted from the thin window towards the thick one, incomplete depletion would show up as a large dead layer. Thus, by checking this dead layer on the ΔE detector (with Th^{228} alpha particle source) the extent of the depletion region was also checked.

The detectors were mounted on a copper holder which was thermally insulated from the rest of the detector arm and cooled by the system described in section 2.2. The effect of the cooling was (1) to reduce the detector leakage currents by at least a factor of 10; (2) to reduce the total (E + ΔE) beta resolution (FWHM of the Bi^{207} 0.972 Mev conversion electron peak) from about 40 kev to about 25 kev.

The detectors were connected to the preamplifiers outside the scattering chamber by about 2 feet of RG 114/U coaxial cable (chosen for its low capacitance). These cables had extra braided copper shields over them to reduce noise pickup.

3.3 Electronics

3.3.1 Preliminary Considerations

Besides having the usual requirements of linearity and resolution, the electronic system for this experiment had to separate the relatively small number of proton pulses from an intense background of pulses from scattered alpha particles. Interference from the alpha particles appeared as a nearly constant "background" in the proton spectra as well as unsymmetric proton peaks extended towards higher energy by pile up (proton pulses partially overlapping with α pulses). Several systems were tried

and modified as experience was gained and new electronics became available.

A discriminator on the signal from the E detector was used to identify high energy protons (and some other particles, see section 3.1). The pulse from this discriminator opened a linear gate allowing the associated sum (E + ΔE) pulse to pass through into the multichannel analyzer. In earlier setups the anlyzer internal linear gate was used (i.e. the analyzer in the coincidence mode) necessitating the use of rather long and slow rise time energy pulses. It was found, however, that shortening the energy pulses and therefore the amount of time the gate needed to be open resulted in more complete exclusion of alpha particle pulses and less pile-up. In order to achieve the above situation the energy pulse was shortened by differentiation, passed through a linear gate and then lengthened again by integration before being fed to the analyzer.

Several other pile-up reduction schemes were tried which involved rejection of proton pulses closely preceded or followed by other pulses (in particular α particle pulses). For example, in one method proton pulses were rejected whenever they occurred in slow coincidence (2τ about 4 μsec) with a large pulse in the ΔE detector (larger than those corresponding to the lowest energy protons of interest).

This method, as well as other similar ones, made the electronics more complicated without significantly improving the short energy pulse system (described in detail below).

3.3.2 Final Setup

Figure 3.1 shows a block diagram of the final electronics system and table 3.4 gives details of the various components. For clarity the

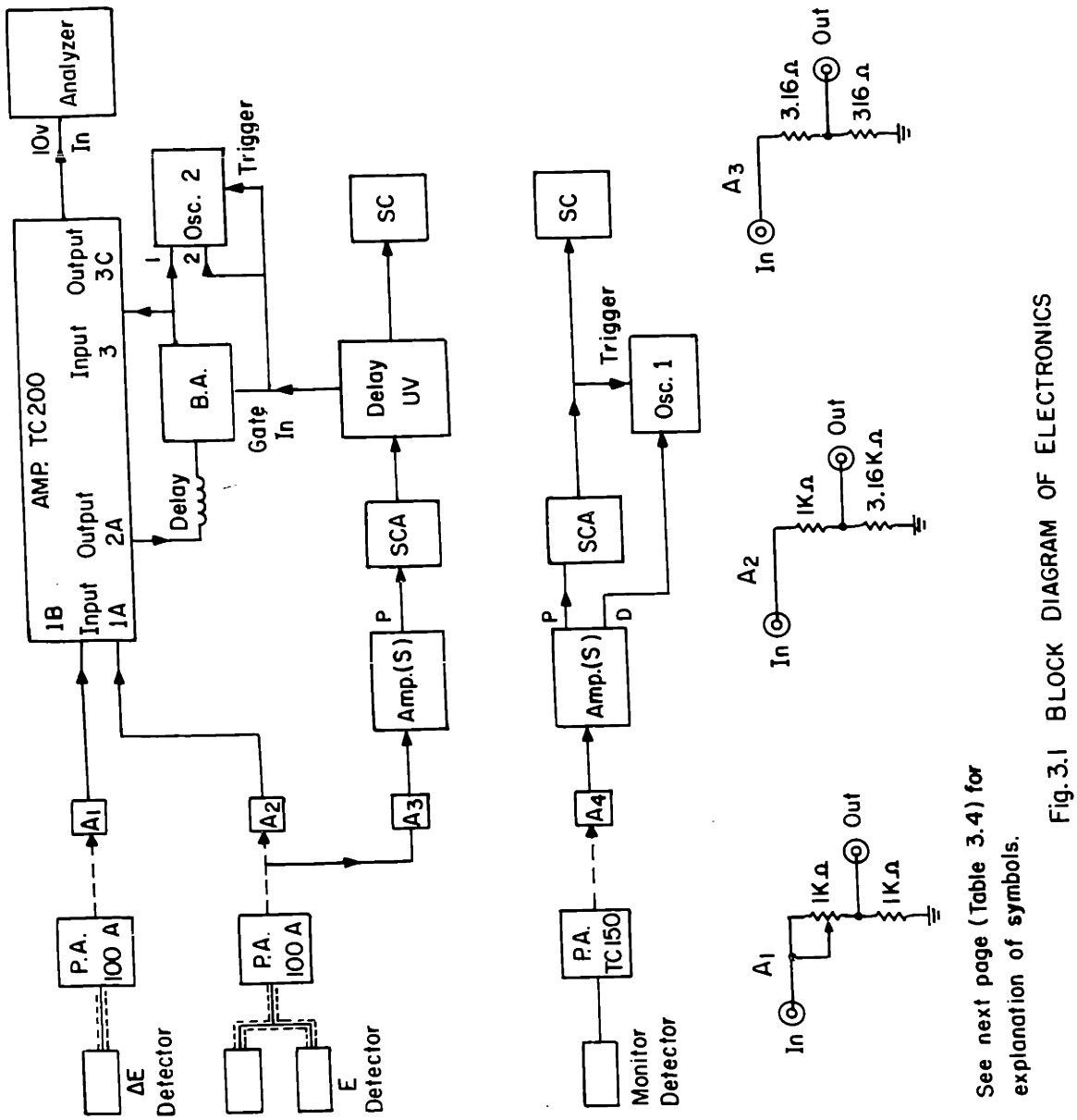

Fig. 3.1 BLOCK DIAGRAM OF ELECTRONICS

See next page (Table 3.4) for explanation of symbols.

=========	About 2 feet RG 114/U coaxial cable with extra shield
- - - - - -▶	About 100 feet RG 71B/U coaxial cable
A_1, A_2, A_3	Attenuators (Circuit diagrams shown)
A_4	93Ω Attenuator
P.A.	Preamplifiers. Tennelec model numbers given directly under P.A.
AMP TC200	Linear amplifier. Tennelec model TC 200
AMP(S)	Linear amplifier. Sturrup model 101. Used in double delay-line pulse shaping mode. P = promp output; D = delayed output.
SCA	Single channel analyzer. Sturrup model 501.
DELAY UV	Univibrator with a variable time delay between input and output pulses.
DELAY	4 sec. delay. Two CTC C729-2000 delay lines in series, with Valor 35LB 61 pulse transformers at each end.
B.A.	Biased amplifier with linear gate. Sturrup model 401.
OSC 1	Oscilloscope
OSC 2	Dual trace oscilloscope

Table 3.4

Explanation of Symbols Used in Figure 3.1

detector biasing connections have been omitted from the diagram. The bias power supply, situated in the experimental control area, had four independently variable voltage outputs each of which was connected to a preamplifier by about 100 feet of RG59/U coaxial cable. Inside each preamp the bias voltage was filtered to eliminate noise and connected to the detector through a 22 megohm resistor.

The pulses produced by the charge sensitive preamps had rise times of about .15 μsec. and decay times of about 50 μsec. The pulse from the ΔE preamplifier was of opposite polarity to that from the E preamplifier. This was necessary since the ΔE pulse was inverted in the main amplifier before being added to the E pulse.

Just before the input to the main amplifier (T ennelec Model TC200) the two pulses were attenuated in such a way as to compensate for any difference in gain between the E and ΔE preamplifiers. The variable attenuator was used to set the ΔE gain equal to that of the E system.

The gains were equated using the following procedure:

1.) The gate in the biased amplifier was switched to the always open position.

2.) A pulser was connected in parallel with the E detector through a 2 pf. capacitor and the detector biases were turned on. The pulser and electronics were adjusted to give a pulse of about 5 volts into the analyzer and a peak was accumulated.

3.) With the bias voltages off, the 2 pf. coupling capacitor was transferred to the ΔE preamplifier input (in parallel with the ΔE detector). With the detector biases on again and the pulser and amplifier gain settings unchanged, the variable attenuator was adjusted to give a peak in the same

position (within about one channel) as the peak obtained in step 2.

After the addition (in the TC 200 amplifier) the sum (E + ΔE) pulse was differentiated with a time constant of 0.2 μsec. producing a pulse at output 2A which was less than 1 μsec. long. This pulse was delayed for four μsec. to allow time for a gate pulse to reach the linear gate (in the biased amplifier) just ahead of the associated sum pulse. The time difference between the arrivals of the two pulses was set to about .2 μsec. by varying the delay in the univibrator which produced the gate pulse. To make this adjustment, both pulses were displayed on a dual trace oscilloscope which was triggered by the gate pulse.

Gate pulses were produced whenever the amplitude of the signal from from the E detector (after amplification and double delay line shaping) exceeded a lower level set by the single channel analyzer. This lower level was set higher than the bias level in the biased amplifier to prevent gate signals for which there were no sum pulses transmitted to the analyzer. Also, for very small output pulses the biased amplifier became non-linear and so the proton pulses of interest were always greater than about 0.5 volt out of the biased amplifier. The delay-line and biased amplifier combination had nearly unity gain since the delay-line attenuated by about a factor of two and the biased amplifier was used with a gain of two.

Following the biased amplifier the pulses were integrated with a time constant of 0.4 μsec. in the final stage of the TC 200 amplifier (accessible through input 3). The second differentiator was not needed since the count rate after the biased amplifier was very low (usually less than 100 counts /sec. total.)

The output pulses from the amplifier were analyzed by a Nuclear Data

4096 2-dimensional pulse height analyzer which was used for this experiment as a 1-dimensional 1024 channel analyzer.

The linearity of the system was checked using a pulse generator (Sturrup Model 1501) connected to the test inputs of the preamplifiers. Besides checking the linearity of the sum signals, a separate check was made on the E signal alone since it was usually over 80% of the sum. The pulser was also used to check the noise level of the electronics and detectors. The FWHM of the pulser peak was usually about 35 kev.

The electronics used with the monitor counters is also shown in figure 3.1. The long pulses from the charge-sensitive preamplifier were amplified and shaped (double delay line) by the amplifier. The single channel analyzer (SCA) selected the pulses (corresponding to elastically scattered alpha particles) which were counted by the scaler. The oscilloscope was used to monitor the setting of the SCA by displaying pulses in coincidence with the SCA output. A more accurate check was occasionally made by analyzing the amplifier output pulses with a multichannel analyzer gated by the SCA output.

CHAPTER 4

EXPERIMENTAL CONSIDERATIONS AND PROCEDURES

4.1 Beam Energy Determination

There have been no accurate beam energy measurements since the remodelling of the entire beam handling system (section 2.1), and so an up-to-date measurement of the beam energy was desired.

The alpha beam energy is too high for an accurate measurement based on a direct comparison with alphas of known energy from a radioactive α-source since available source energies are less than 1/3 of the beam energy.

In view of the above difficulty, two distinct approaches were used. The first involved degrading the alpha energy with a Be absorber to the point where it could be accurately measured by direct comparison with the alphas from a Th^{228} source, and then using the range-energy relations for Be to find the energy incident on the known thickness absorber. The accuracy of this method depended on the accuracy of the range-energy calculations and the absorber thickness measurement as well as the uniformity of the absorber.

The second approach involved kinematic measurements which were quite dependent on the scattering angle and which required a separate energy calibration which was accurate at the higher energies (see section 3 below).

The reasons for using different methods were: (1) a more accurate value could be obtained by comparing the results of different methods and (2) the best method could be found not only for an absolute energy determination, but also for relative energy measurements to ensure that the beam energy does not change appreciably during an experiment. The last point is

important since the beam energy is somewhat dependent on the cyclotron and beam handling system conditions.

The proton beam energy was also measured because it provided a check on the Be absorber technique (see below) and also because the proton energy is related to the alpha particle energy. Since the cyclotron oscillator frequency is constant (checked with a frequency meter to be constant within .1%) and the beam extraction radius is constant (within about $\pm$ 0.2 inches or 1%) then all particles leaving the cyclotron must have the same velocity (within the limits imposed above). Thus, the alpha particle energy (E_α) is related to the proton energy (Ep) by: $E_\alpha = (m_\alpha/m_p)Ep = (3.97)Ep \pm 2\%$, where m_α and mp are the α particle mass and the proton mass respectively.

Two energy calibrations were used for the energy measurements. One was a Th^{228} source deposited on aluminum foil. This "home made" source was checked for self absorbtion by comparing it with a thin (less than 8 kev equivalent source thickness) Am^{241} source purchased from ORTEC. The low energy Th^{228} alphas appeared to be degraded about 10 kev more than those from the Am^{241} source. An additional correction of 10 kev (at 5.5 Mev) was made to account for energy lost in the dead layer on the front of the silicon surface barrier detector (from ORTEC) used for all beam energy measurements.

Figure 4.1 shows the Th^{228} spectrum with each strong peak labelled by the parent nucleus, the undegraded energy (from B2 except Po^{212} which was from N1) and the correction used to obtain the energy entering the sensitive portion of the detector. A linear fit to the degraded energies listed in figure 4.1 and the associated peak channel numbers was used to determine the energy slope and zero intercept in the 1024 channel analyzer. None of the

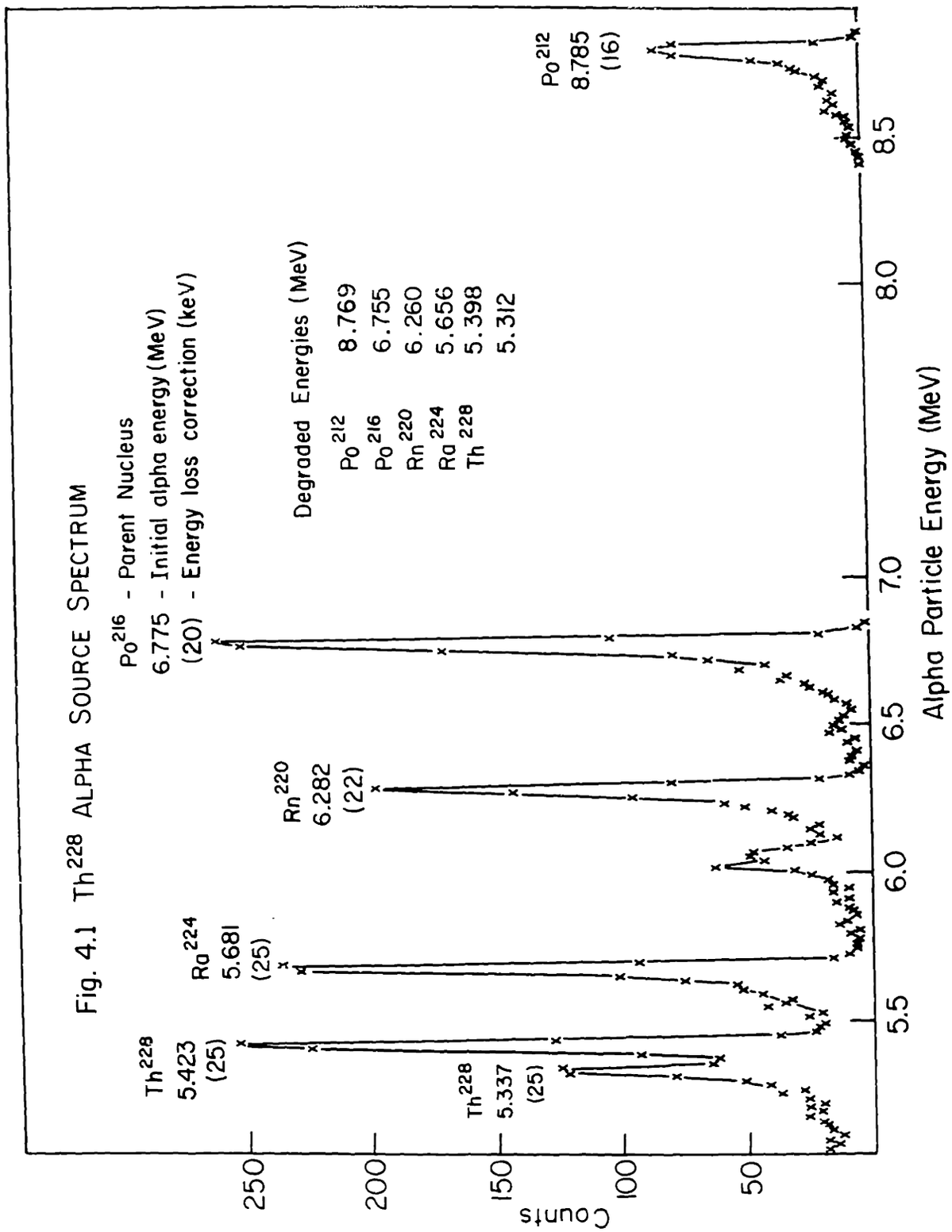
Fig. 4.1 Th228 ALPHA SOURCE SPECTRUM
Po216 - Parent Nucleus
6.775 - Initial alpha energy (MeV)
(20) - Energy loss correction (keV)
Degraded Energies (MeV)
Po212 8.769
Po216 6.755
Rn220 6.260
Ra224 5.656
Th228 5.398
5.312
Th228 5.423 (25)
Ra224 5.681 (25)
Rn220 6.282 (22)
Th228 5.337 (25)
Po212 8.785 (16)
Counts
250
200
150
100
50
5.5
6.0
6.5
7.0
8.0
8.5
Alpha Particle Energy (MeV)

six calibration peaks differed by more than ± 5 kev from the value calculated using the average slope and intercept. The error in the zero energy position was estimated to be ± 15 kev.

The other energy calibration used was the energy difference between alpha particles elastically scattered by C^{12} and those inelastically scattered leaving C^{12} in its 4.433 Mev state. This energy difference, corrected for energy loss in the target, was calculated for each scattering angle using approximately the right beam energy. The error introduced by not using exactly the right beam energy was less than .02% and the error due to angular uncertainty (0.2 degrees) was less than 0.1%.

4.1.1 Proton Beam Energy

The proton energy was measured by two methods, both of which used the known energy alpha particles from the Th^{228} source to determine the energy-channel number relationship in the 1024 channel analyzer. In the first method, the channel number of the peak corresponding to protons elastically scattered from gold was converted to an energy and after adding the kinematic correction for scattering angle (0.5%) the proton beam energy was obtained. The energy loss in the .17 mg/cm^2 gold target was neglected as it amounted to only about 4 kev.

The second proton energy measurement involved placing Be absorbers in front of the detector and measuring both the energy after the absorber and the energy shift due to the absorber. The approximately 1 inch square absorbers (obtained from the Brush Beryllium Company) were measured and weighed and found to have thicknesses of 74.2 ± .5, 66.0 ± .3, 60.2 ± .4,

50.7 ± .4, 44.5 ± .4, and 31.5 ± .3 mg/cm^2. The errors were based on estimated errors in weighing (± 1mg) and measurement (± .002 inch for each side). The 66.0 mg/cm^2 absorber was the only one which consisted of a single piece of Be and thus the error in its thickness is somewhat smaller than the others.

The energy losses in the absorbers were calculated from the range - energy relations for protons in Be. The proton ranges, shown in figure 4.2, were those used as input data by W. H. Barkas and M. J. Berger (Z1) who summarized the stopping-power and range data below 8 Mev using a 9 parameter least squares range formula. These input ranges are slightly smaller (a few percent) than those of Bichsel et al. (B1) and Sternheimer (S1). In order to calculate the energy losses for the absorbers used in this experiment, the ranges were interpolated using a computer program which fit the six points nearest the point of interpolation with a fifth order polynomial. The errors in the energy losses calculated by this method are estimated to be ± 2%.

The energy shift due to each absorber was calculated for various incident energies, and the energy out of each absorber was obtained by subtracting the energy shift from the incident energy. The incident energy corresponding to each measured energy shift and final energy was found by graphical interpolation. This method, as applied to the measurement of the alpha beam energy, is described in more detail below.

4.1.2 Alpha Beam Energy - Be Absorber Method

The Be absorber method (using the same absorbers) was also used to measure the alpha beam energy. The range for alpha particles, R_α, was obtained from that for protons, R_p, in the same material by:

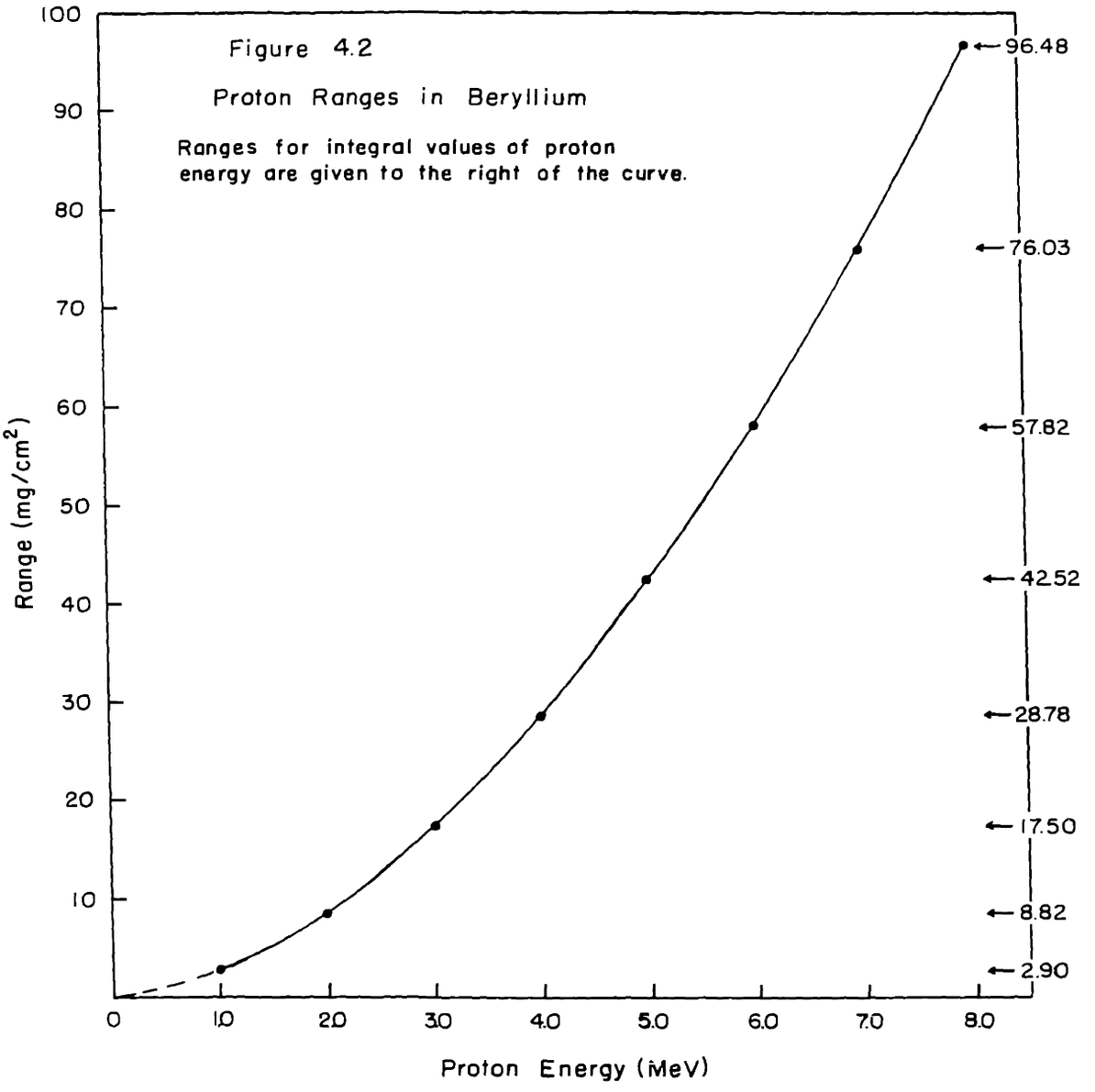
Figure 4.2
Proton Ranges in Beryllium
Ranges for integral values of proton energy are given to the right of the curve.
Range (mg/cm²)
Proton Energy (MeV)
100
90
80
70
60
50
40
30
20
10
0
1.0
2.0
3.0
4.0
5.0
6.0
7.0
8.0
96.48
76.03
57.82
42.52
28.78
17.50
8.82
2.90

$$R_\alpha(E_\alpha) = {}^{m_\alpha}/_{Z_\alpha^2}\, R_p(E_\alpha\, {}^{m_\alpha}/_{m_p}) = .993\, R_p\,({}^{E_\alpha}/_{3.97})$$

where E_α is the α particle energy, m_α is its mass, and m_p is the proton mass. Using this relationship the energy shift (ΔE) and degraded energy (E_{out}) were calculated for each absorber for various values of the energy incident on the absorber. Figure 4.3 shows the results for the 74.2 mg/cm^2 absorber.

Both the Th^{228} and C^{12} scattering energy calibrations were used to determine the measured energy shift, and both values are indicated with estimated ± 1% errors to account for uncertainties in the energy slope and linerarity of the electronics. The corresponding error for the absolute energy (E_{Out}) measurement was taken to be ± 1% of the difference between the measured energy and the "middle" of the Th^{228} spectrum with an additional ± 15 kev for the zero energy error.

The energy incident on the Be absorber, with errors due to energy measurement, was determined graphically as shown in figure 4.3. The beam energy was obtained by adding to this energy the kinematic energy loss (0.65% for α scattering from Au at 32.9 degrees) and the energy lost in the .17 mg/cm^2 Au target (about 15 kev). For this energy measurement the total correction used was 220 kev.

The total error in the beam energy measurement was found by taking the square root of the sum of the squares of the separate errors due to uncertainties in energy measurement, absorber thickness, and specific energy loss. A summary of the results of the Be absorber method is given in table 4.1 for the four thickest absorbers. The measurements using the thinner absorbers were not used because of the large errors involved.

A quick and convenient method of checking the beam energy is illu-

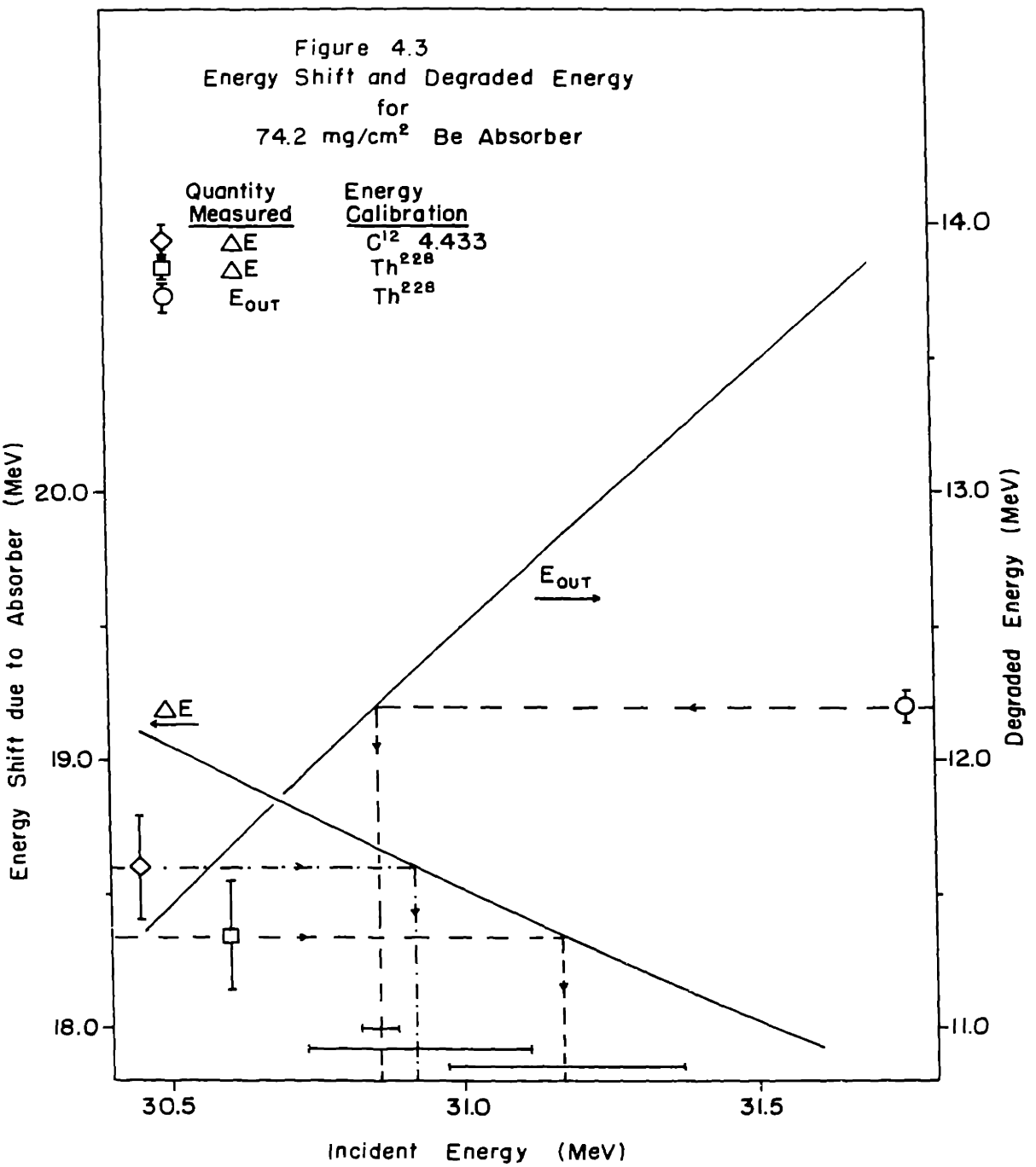
Figure 4.3
Energy Shift and Degraded Energy
for
74.2 mg/cm² Be Absorber
Quantity Measured
Energy Calibration
ΔE
C¹² 4.433
ΔE
Th²²⁸
E_OUT
Th²²⁸
E_OUT
ΔE
20.0
19.0
18.0
14.0
13.0
12.0
11.0
30.5
31.0
31.5
Energy Shift due to Absorber (MeV)
Degraded Energy (MeV)
Incident Energy (MeV)

Absorber Thickness (mg/cm^2)	74.2(.5)	66.0(.3)	60.2(.4)	50.7(.4)
Measured ΔE^*	18.60(.19)	15.43(.16)	18.34(.14)	11.04(.11)
Resultant Beam Energy	31.1 (.5)	31.4 (.4)	31.3 (.6)	31.4 (.6)
Measured ΔE^{**}	18.34(.19)	15.22(.16)	13.65(.14)	10.89(.11)
Resultant Beam Energy	31.4 (.5)	31.7 (.4)	31.4 (.6)	31.7 (.6)
Measured E_{out}^{**}	12.20(.06)	15.32(.10)	16.89(.12)	19.65(.16)
Resultant Beam Energy	31.1 (.3)	31.4 (.3)	31.1 (.3)	31.1 (.3)

All energies are in Mev.

*C^{12} (4.433) Energy calibration

**Th^{228} Energy calibration

Errors are in parenthese. i.e. 31.1 (.3) ≡ 31.1 ±.3 Mev.

Table 4.1

Alpha Beam Energy Results from Beryllium Absorber Method

strated in figure 4.4. The curve was obtained from the following procedure. The measured ratio of the energy shift due to the thickest (74.2 mg/cm^2) absorber to that for the thinnest (31.5 mg/cm^2) was determined from the locations (channel numbers) of the relevant peaks in the analyzer. This ratio was reproduced by varying the thickness of the thinner absorber in the energy loss calculations assuming the thickest absorber was exactly 74.2 mg/cm^2, and the energy incident on the absorbers was 30.64 Mev. In this way the thinner absorber was determined to be 31.78 mg/cm^2 and the curve in figure 4.4 was calculated using this value. The $\pm \frac{1}{2}\%$ error in the measured value of the ratio is an estimate of the uncertainty due to non-linearity of the electronics. The relative accuracy of this method should be considerably better than $\pm \frac{1}{2}\%$ if the same electronics are used and about the same pulse heights are involved in different measurements.

4.1.3 Alpha Beam Energy - Kinematic Method

An independent check on the above methods was made by measuring the difference in energy between elastic alpha scattering from C^{12} and Au. For this measurement the target consisted of .17 mg/cm^2 thickness of gold deposited on a mylar target 0.49 mg/cm^2 thick. Thus, the elastic scattering from both gold and carbon and an energy calibration from inelastic scattering from carbon were obtained simultaneously.

The application of the principles of conservation of energy and momentum to elastic scattering yields for all quantities measured in the laboratory system:

$$K \equiv E/E_o = \left(\frac{m}{M+m}\right)^2 \left\{\cos\theta + \left[(M/m)^2 - \sin^2\theta\right]^{\frac{1}{2}}\right\} \qquad (4.1)$$

where E_o is the initial energy of the particle of mass m, E is its energy

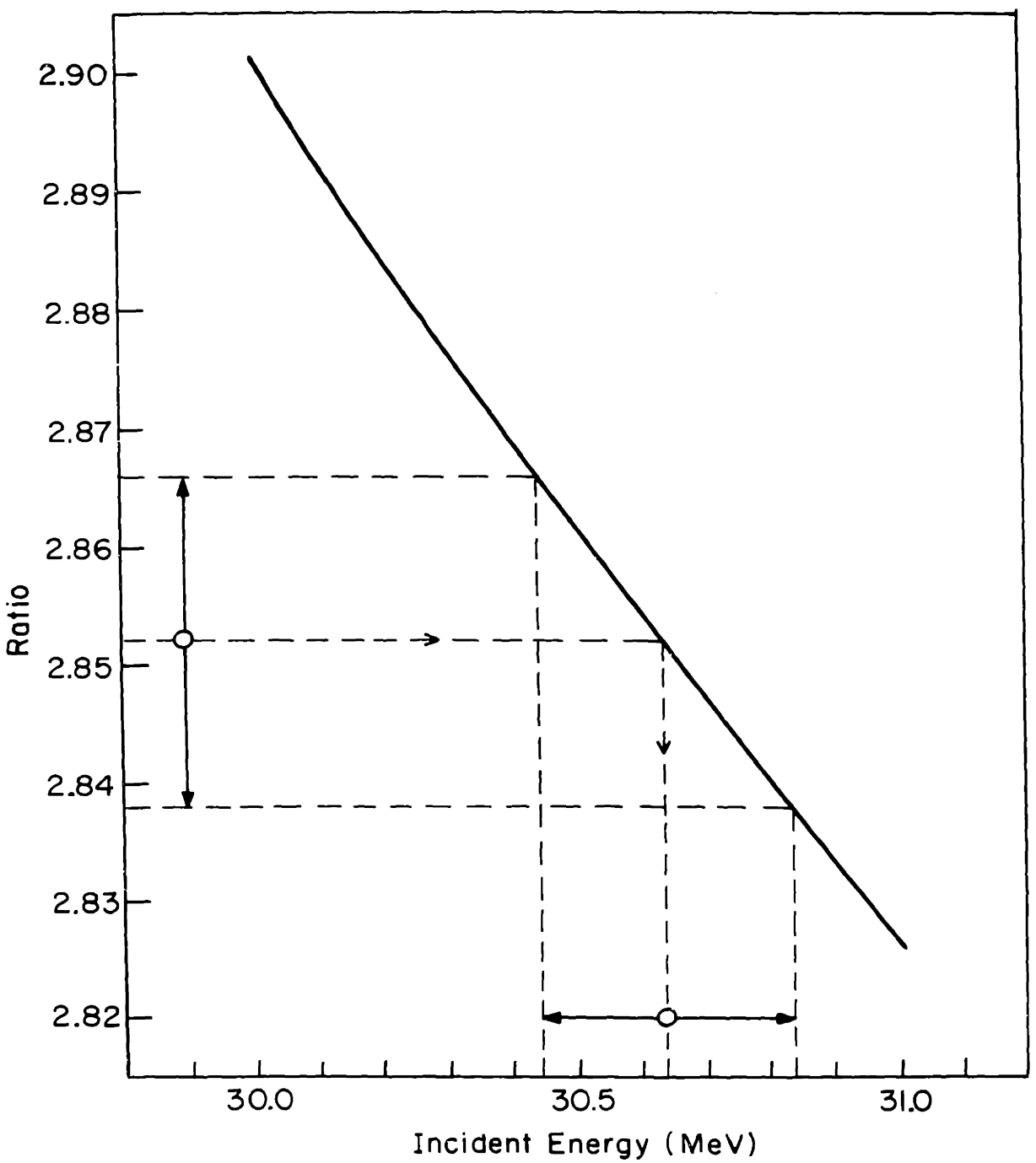

Fig. 4.4. RATIO OF ENERGY SHIFTS FOR 74.2 AND 31.78 mg/cm^2 Be ABSORBERS

after scattering through the angle θ, and M is the target mass ($m<M$). Applying equation (1) to alpha scattering from Au and C^{12} and including energy losses in the target we obtain:

$$E_1 = (E_o - dE_1)\, K_1(\theta) - dE_1' \qquad (4.2)$$

and

$$E_2 = (E_o - dE_2)\, K_2(\theta) - dE_2' \qquad (4.3)$$

where: E_1 is the observed α energy after scattering from Au, dE_1 is the energy lost before scattering, dE_1' is the energy lost after scattering and $K_1(\theta)$ is the ratio given by equation 1, evaluated for α particle scattering from Au. E_2, dE_2, dE_2' and $K_2(\theta)$ are the corresponding quantities for the case of scattering from C^{12}. The energy losses were calculated assuming the gold scattering occurred in the center of the gold target, and the C^{12} scattering occurred in the center of the mylar target, and using the value of the beam energy found in section 2 above.

Subtracting equation (2) from equation (3) and solving for the beam energy we get:

$$E_o = (E_1 - E_2)\, F_1(\theta) + F_2(\theta)$$

where: $F_1(\theta) = \dfrac{1}{K_1(\theta) - K_2(\theta)}$ is dependent only on θ and

$F_2(\theta) = \left[dE_1 K_1(\theta) - dE_2 K_2(\theta) + dE_1' - dE_2'\right] F_1(\theta)$ is a correction for energy loss in the target. Without introducing any significant error, F_2 was assumed to be independent of beam energy over a small range. Figure 4.5 shows F_1 and F_2 plotted versus θ.

In practice, the energy difference $(E_1 - E_2)$ was measured in terms of channel numbers and a calibration energy difference:

$$E_1 - E_2 = \left[\frac{N_{Au} - N_C}{N_C - N_{cal}}\right] E_{cal}$$

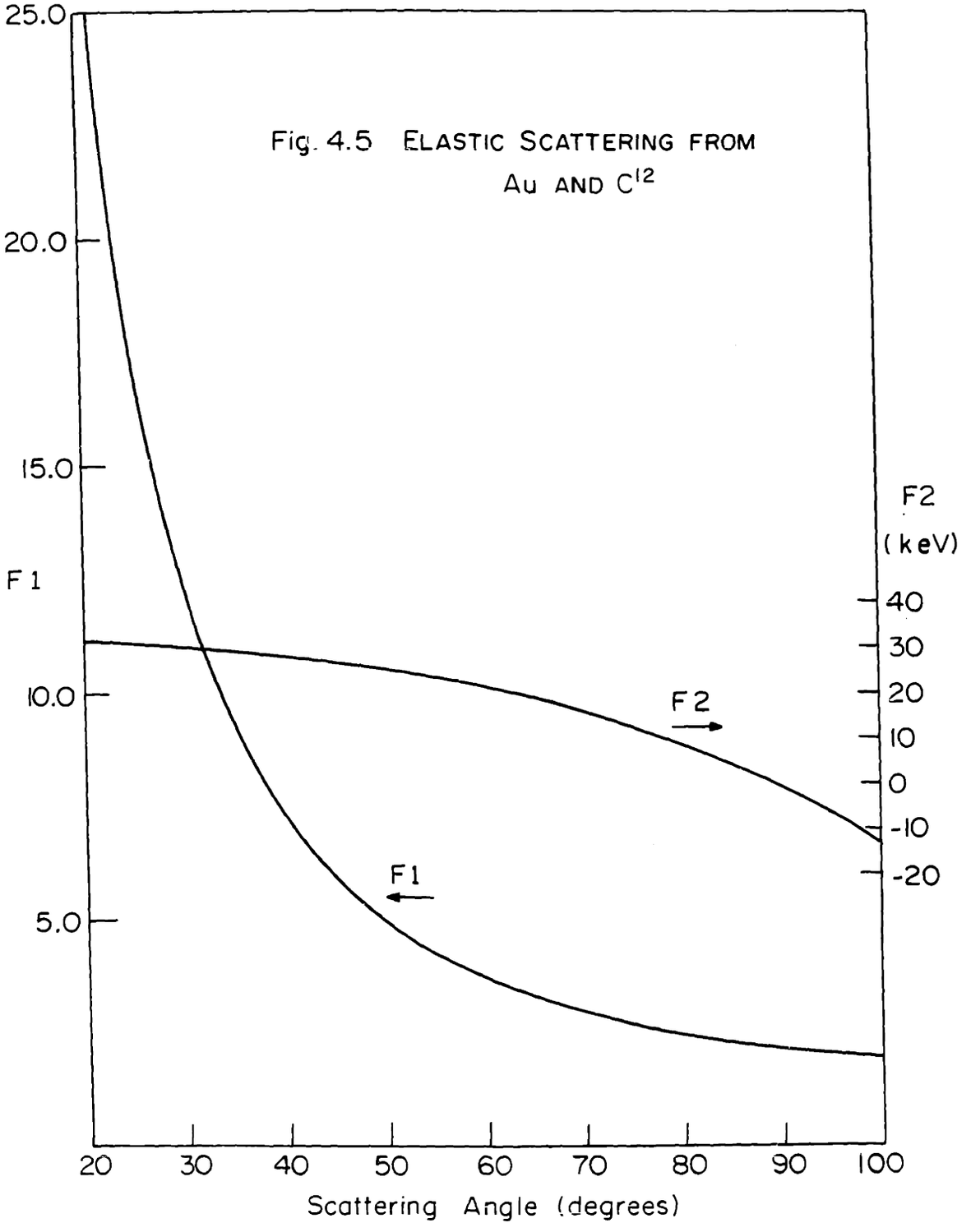

Fig. 4.5 ELASTIC SCATTERING FROM Au AND C^{12}

where N_{Au} and N_C are the channel numbers of the gold and carbon elastic peaks, N_{cal} is the channel number of the inelastic carbon peak used for calibration, and E_{cal} is the calculated energy difference between the carbon elastic peak and the calibration peak.

Thus we have finally:

$$E_o = \left[\frac{N_{Au}-N_C}{N_C-N_{cal}}\right] E_{cal}\, F_1(\theta) + F_2(\theta) \qquad (4.4)$$

A kinematics program (NEWKIN) for the IBM 7044 computer was modified to calculate F_1, E_{cal} the product E_{cal} X F_1, and F_2.

Figure 4.6 shows how equation (4) was used to find both the beam energy and the position of $\theta = 0$. The energy calibration was obtained from the 4.433 state in C^{12}. The ratio $(N_{Au}-N_C)/(N_C-N_{cal})$ was measured at various angles (θ_o) which were determined using an assumed value for the zero angle ($\theta_o=0$). Equation (4) was then used to find the beam energy for $\theta = \theta_o-1^o$, θ_o, and $\theta_o + 1^o$ for each value of θ_o used. The results for $\theta_o = 30^o$, 100^o and -30^o with $\pm$ 0.2 degree angular errors are shown in figure 4.6. The shaded area gives the region of angles ($\theta-\theta_o = 0.1 \pm 0.2$ degrees) and beam energies (30.62 ± 0.15 Mev) consistent with the three curves and their errors. The probable error in the beam energy determined by this method was estimated to be $\pm$ 200 kev. To obtain the final result for the beam energy, several additional large angle ($60^o - 80^o$) measurements were taken into account.

4.1.4 Results and Conclusions

The proton and alpha beam energies determined by the above methods

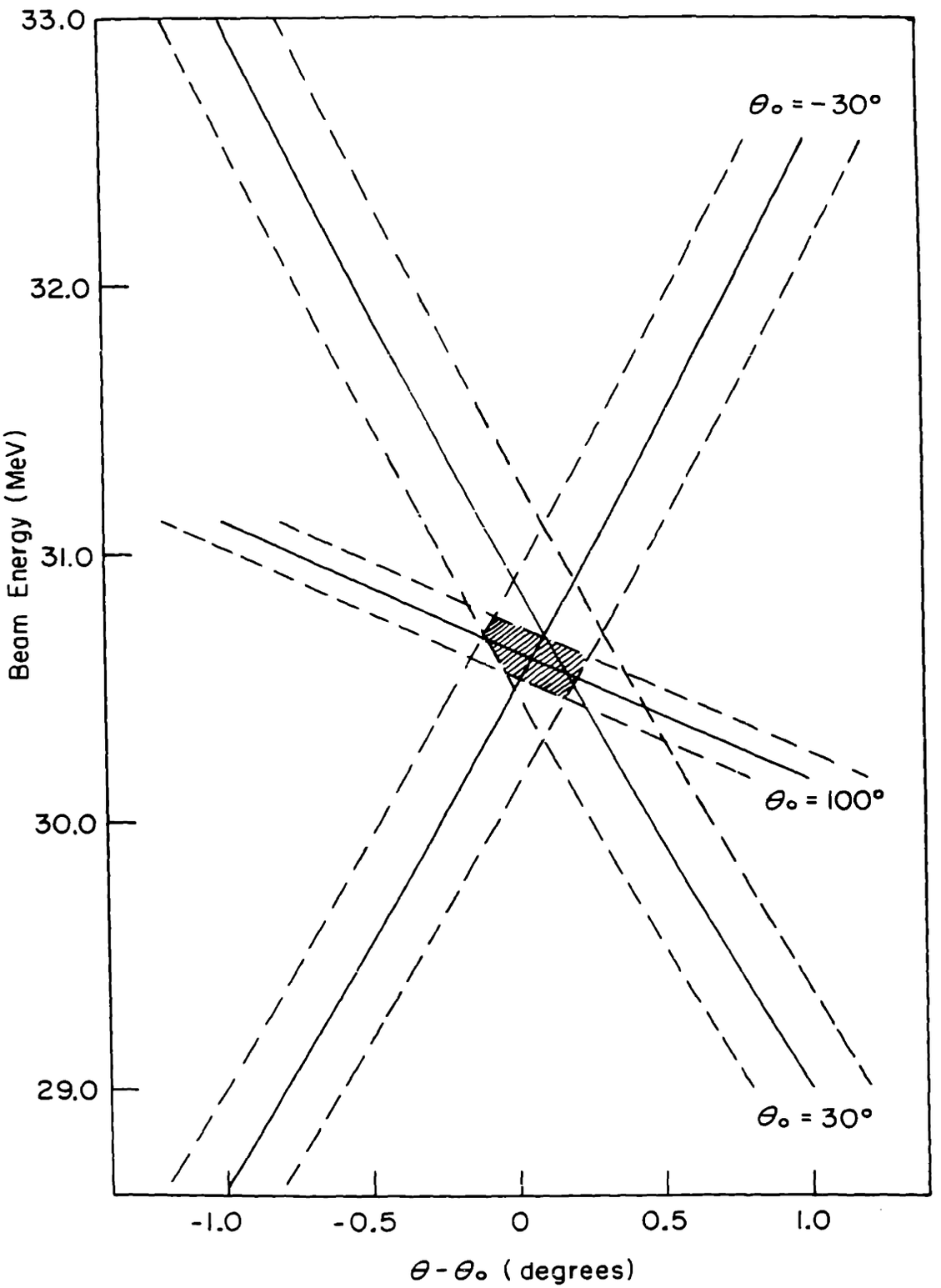

Fig. 4.6 BEAM ENERGY FROM Au AND C^{12} ELASTIC SCATTERING

are presented in table 4.2. The final alpha beam energy (31.0 ± .4 Mev) was determined from a consideration of the various results, their accuracy, and their independence.

The most accurate methods for measuring the alpha beam energy were found to be the Au-C^{12} elastic scattering method and the Be absorber method using a thick (74.2 mg/cm^2) absorber and measuring the energy after the absorber by comparison with the Th^{228} source. The former method also provides a check on the zero scattering angle position, as well as providing an independent calibration of the absorber method.

The large spread in results (table 4.2) may be due in part to beam energy shifts during the measurements. Thus better results might be obtained by monitoring changes in the beam energy while it is being measured. This could be done by an alpha detector which, partially covered by a thick absorber, partially covered by a thin absorber and partially uncovered, would, when exposed to elastically scattered alpha particles, yield three peaks whose relative positions would be sensitive to the beam energy (see figure 4.4).

4.2 (α,p) Energy Resolution

The observed energy spread of the proton groups from the (α,p) reaction to isolated states of the final nucleus is a result of a complicated combination of energy spreads from various sources (e.g. alpha beam spread, target thickness, detector noise, etc.), making an exact calculation of the observed peak width impossible, or at least extremely difficult. However, in order to obtain the best resolution consistent with other requirements (e.g. count rate), it is sufficient to understand the individual contributions from the important sources. The sources of energy spread considered

Particle	Method	Calibration	Energy (Mev)
p	Direct comparison	Th^{228} source	7.77 ± .03
p	Be absorbers - ΔE	Th^{228} source	7.72 ± .06
p	Be absorbers - E_{out}	Th^{228} source	7.75 ± .06
α	From proton energy	Th^{228} source	30.85 ± .60
α	Be absorbers - E_{out}	Th^{228} source	30.87 ± .10
α	Be absorbers - ΔE	Th^{228} source	31.04 ± .22
α	Be absorbers - ΔE	C^{12}(4.433)	30.78 ± .22
α	Au-C^{12} elastic scattering	C^{12}(4.433)	30.71 ± .20
α	Final Value	Both	30.80 ± .10

Table 4.2

Beam Energy Results

important for this experiment were :

1) Alpha Beam Spread with Detector and Electronic Noise.

These were considered together because they were measured together by observing alpha particles elastically scattered by a thin gold target. The F.W.H.M. of the peak obtained in this way was usually about 80 kev. for the horizontal slit settings (0.050 inches) used in this experiment (see section 2.1). At wider slit settings the resolution was poorer (with greater beam current also), but no improvement was noticed when the separation was made less than 0.050 inches (although the beam current decreased).

2) Dependence of Proton Energy on Interaction Depth in the Target.

Neglecting energy losses in the target the observed proton energy (Ep) from an (α,p) reaction can be written:

$$Ep = Ep'(E_\alpha)$$

where the kinematic energy (Ep'), depends on the masses (alpha particle, target nucleus, final nucleus, and proton), the Q value, and the scattering angle as well as the initial alpha particle energy (E_α), as indicated.

The effect of energy losses in the target is to reduce the observed proton energy to:

$$Ep = Ep' \left(E_\alpha - (dE/dx)_\alpha t_\alpha\right) - (dE/dx)_p t_p$$

where t_α and tp are the distances traveled in the target by the alpha particle and the proton respectively (see figure 4.7). The specific energy loss for the alpha particle $(dE/dx)_\alpha$, is evaluated at the energy E_α, and that for the proton $(dE/dx)_p$, is evaluated at Ep. Referring to figure 4.7 we see that:

$$tp = \frac{t - t_\alpha \cos\phi}{\cos(\theta+\phi)}$$

where t is the target thickness, θ is the angle of proton emission and ϕ

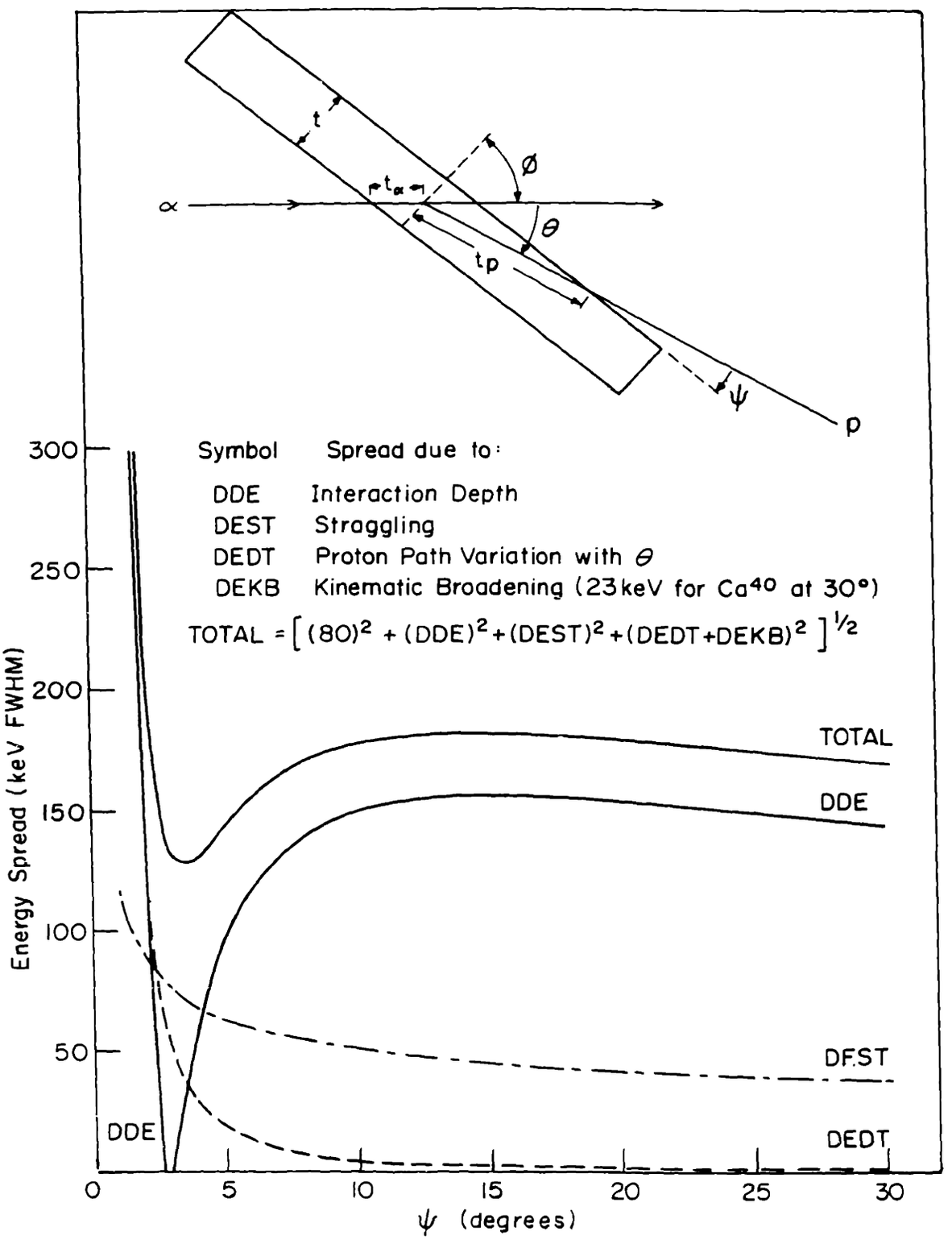

Fig. 4.7 $Ca^{40}(\alpha,p)Sc^{43}_{gnd}$ RESOLUTION CALCULATIONS

is the target angle. Thus:

$$Ep(t_\alpha) = Ep'\ (E_\alpha - (dE/dx)_\alpha t_\alpha) - (\frac{dE}{dx})_p \quad \frac{(t-t_\alpha \cos\phi)}{\cos(\theta+\phi)}$$

Ep' is approximately a linear function of energy and the alpha and proton specific energy losses are very nearly constant for the targets (1.0-1.5 mg/cm^2 thick) used in this experiment. Also, the (α,p) reactions occur uniformly (to a very good approximation) along the path of the incident alpha particles in the target. Therefore, the energy spectrum from this effect alone will have a rectangular shape with a width given by:

$$DDE = Ep(t_\alpha=0) - Ep(t_\alpha = t/\cos\phi)$$

or: $$DDE = Ep'(E_\alpha) - Ep'(E_\alpha - dE_\alpha) = dEp$$

where $dE_\alpha = (dE/dx)_\alpha t/\cos\phi$ and $dEp = (dE/dx)_p\ t/\cos\ (\theta+\phi)$

3) Energy Straggling in the Target

To evaluate the energy spread due to straggling, it was assumed that the reaction took place at the center of the target.

Thus: $$t_\alpha = \frac{t}{2\cos\phi} \text{ and } tp = \frac{t}{2\cos\ (\theta+\phi)}$$

The standard deviation, σ, of the particle energy due to straggling may be found from the approximate formula given by Bethe and Askin (S2):

$$\frac{d}{dx}\sigma^2 = 4\pi e^4\ z^2\ NZ$$

where x is the distance traveled in the target, ze is the charge of the particle, N is the number of atoms per unit volume in the target, and Z is the number of electrons per target atom. This reduces to:

$$\sigma^2 = 156\ z^2\ (Z/A)\ t \quad (kev^2)$$

where A is the atomic weight of the target atoms and t is the distance traveled in the target (in mg/cm^2). Assuming Z/A = 0.5, and converting to the FWHM (FWHM = 2.35σ) we get:

$$\Delta E = 20.7 \quad z\sqrt{t} \qquad \text{(kev FWHM)}$$

For the (α,p) reaction there are contributions from both the α particle and the proton:

$$\Delta E_\alpha = 41.4\sqrt{t_\alpha} \quad \text{and} \quad \Delta Ep = 20.7\sqrt{tp}$$

The proton energy spread due to both of these will be:

$$DEST = \left[K^2(\Delta E_\alpha)^2 + (\Delta E_p)^2\right]^{1/2}$$

where K is the change in proton energy per unit change in α energy, and is usually close to unity.

4) Variation in Proton Paths leaving the Target

With the center of the detector set at an angle θ, protons were detected within an angular region of roughly $\theta \pm 0.5$ degrees. However, the amount of target material traversed by the proton increases with increasing scattering angle (for a fixed target angle). Assuming the reaction takes place at the center of the target, this variation of proton path length within the target causes an energy spread:

$$DEDT = (dE/dx)_p \; t/2 \left[\frac{1}{\cos(\theta+0.5+\phi)} - \frac{1}{\cos(\theta-0.5+\phi)}\right]$$

5) Kinematic Broadening

The angular spread described above causes another energy spread due to the kinematic variation of proton energy with scattering angle. This energy spread will be (for the angle θ):

$$DEKB = Ep'(\theta-0.5) - Ep'(\theta+0.5)$$

where $Ep'(\theta)$ = energy of proton emitted at the angle θ. This effect and DEDT are the only coherent effects, and so an estimate of the total resolution was obtained from:

$$TOTAL = \left[(80)^2 + (DDE)^2 + (DEST)^2 + (DEDT + DEKB)^2\right]^{1/2}$$

All of the above energy spreads were calculated using a modified

kinematics program (NEWKIN) for the IBM 7044 computer. Figure 4.7 shows the results for a 1.0 mg/cm^2 Ca^{40} target and a proton emission angle of 30° lab.

Experimentally, the $Ca^{40}(\alpha,p)Sc^{43}$ resolution was measured for different target angles at $\theta = 30°$. A natural Ca target about 1.0 mg/cm^2 was used. The results for the ground state peak were:

	Resolution (kev FWHM)	
ψ	Experiment	Theory
5°	138	143
10°	148	177
15°	234	182

where $\psi = 90-(\theta+\phi)$

The discrepancy between the calculated and observed values may be due to several factors. The first possible explanation is based on experimental inaccuracies in the target thickness and target angle. The target thickness was measured by a micrometer and found to be 1.1 ± 0.3 mg/cm^2. The target angle uncertainty (possibly as much as a few degrees) was due to the fact that these resolution measurements were made before the improvements to the target angle readout system were installed (see section 2.2). However, later measurements confirm that little or no improvement is seen between $\psi = 10°$ and $\psi = 5°$. Based on these measurements, the value for ψ was usually set at 10°.

The second possible reason for disagreement is that the calculated resolution may be incorrect due either to effects not taken into account (e.g. irregularities in the target) or that the different effects calculated were not combined correctly to obtain the total resolution.

Further resolution measurements were made on the $C^{12}(\alpha,p)N^{15}$ reaction

at 35° using mylar targets of different thickness. The results were:

Thickness (mg/cm^2)	ψ	Resolution (kev FWHM) Experiment	Theory
0.49	5	127	119
0.49	10	128	130
0.49	15	132	134
0.85	10	185	160
1.71	10	236	253

The agreement here is somewhat better although the situation is quite different from Ca. The targets were easier to make (free of wrinkles) and their thicknesses were fairly accurately determined. Also, kinematic broadening was a much greater fraction of the total resolution, especially in the case of the thin mylar target.

Thus, while these calculations cannot be taken too seriously, it seems that most of the contributions have been accounted for with reasonable accuracy.

4.3 Targets

The five targets used in this experiment were all self-supporting metallic foils, and all except Ca^{40} were isotopically enriched. Table 4.3 gives the isotopic analysis and thickness of each target.

The Ca^{40} target was made by evaporating natural calcium on to a thin tantalum sheet. The tantalum sheet was bent to loosen the layer of calcium which was picked up by double-sided masking tape (Scotch No. 410). The thickness of this target was measured by a micrometer and is therefore only approximate (± 30%). The thickness of each of the other calcium targets was measured by the extent to which it degraded the energy of 5.48 Mev alpha particles from Am^{241}. These thicknesses have probable errors of ± 10%.

The Ca^{44} target was made by an evaporation process similar to that described above (for the Ca^{40} target), but starting from $Ca^{44}CO_3$ obtained from the Oak Ridge National Laboratory.

The Ca^{42}, Ca^{48} and Ti^{48} targets were obtained as foils from Oak Ridge and so they were simply mounted on target frames before being used. The approximate thickness of the Ti^{48} target was obtained from a measurement of the area and the weight of the target as specified by Oak Ridge.

To minimize oxidation of the calcium targets, they were stored under high vaccuum when not in use and were transported to the scattering chamber in an atmosphere of argon gas.

4.4 Proton Spectrum Measurement

Before each (α,p) run the detectors and electronic system (see Chapter 3) were set up and checked for noise and linearity. The monitor

Target	Isotopic Percentage (by Mass number)						Thickness mg/cm^2
	40	42	43	44	46	48	
Ca^{40}	96.97	0.64	0.145	2.06	0.0033	0.18	1.1
Ca^{42}	4.96	93.7	0.19	1.18	.02	.02	1.19
Ca^{44}	1.30	0.04	0.04	98.61	.002	0.01	0.68
Ca^{48}	1.93	0.03	.01	0.06	.01	97.98	0.94

	46	47	48	49	50	
Ti^{48}	0.16	0.29	99.22	0.23	0.11	1.48

Table 4.3

Target Data

counters were set up to count elastically scattered alpha particles from the target being used. The remotely controlled monitor was positioned at an angle where the elastic cross section was not rapidly varying with angle, usually about 30°.

Next, the zero scattering angle was determined for the proton detector. With a discriminator set to count elastic alphas in the ΔE detector, the angular distribution of elastic alpha particles was recorded for an angular region between about 15° and 25° (using an approximate value for the zero angle). The angles were read in terms of the dial setting on the 10 turn helipot used on the angle readout system. The alphas were counted every 5 helipot units (1.8 degrees) and the different angles were normalized by dividing by the number of counts recorded by the in-plane monitor.

The angular distribution measurement was repeated for about the same angular range on the other side of the beam. Both angular distributions were plotted versus the scattering angle in helipot units, and the symmetry angle (0 degrees) was determined from the graph. This method was checked by measurements of the energy difference between elastic scattering from C^{12} and Au (see Section 4.1.3 and Figure 4.6). The two methods gave the same answer to within the accuracy of the angle readout helipots (0.2 degrees).

With the zero angle known, the proton detector was set at an angle of 35 degrees and a proton spectrum was recorded using a 0.49 mg/cm^2 Mylar target. Besides providing a check on the total (α,p) resolution, this spectrum also gave a convenient energy calibration. Figure 4.8 shows the (α,p) spectrum from Mylar ($C_{10}H_8O_4$) at 35° with positions (relative to the $C^{12}(\alpha,p)N^{15}$ ground state peak) of several states in N^{15} and F^{19}. The intense peak just below 16 Mev proton energy was identified with one or both of

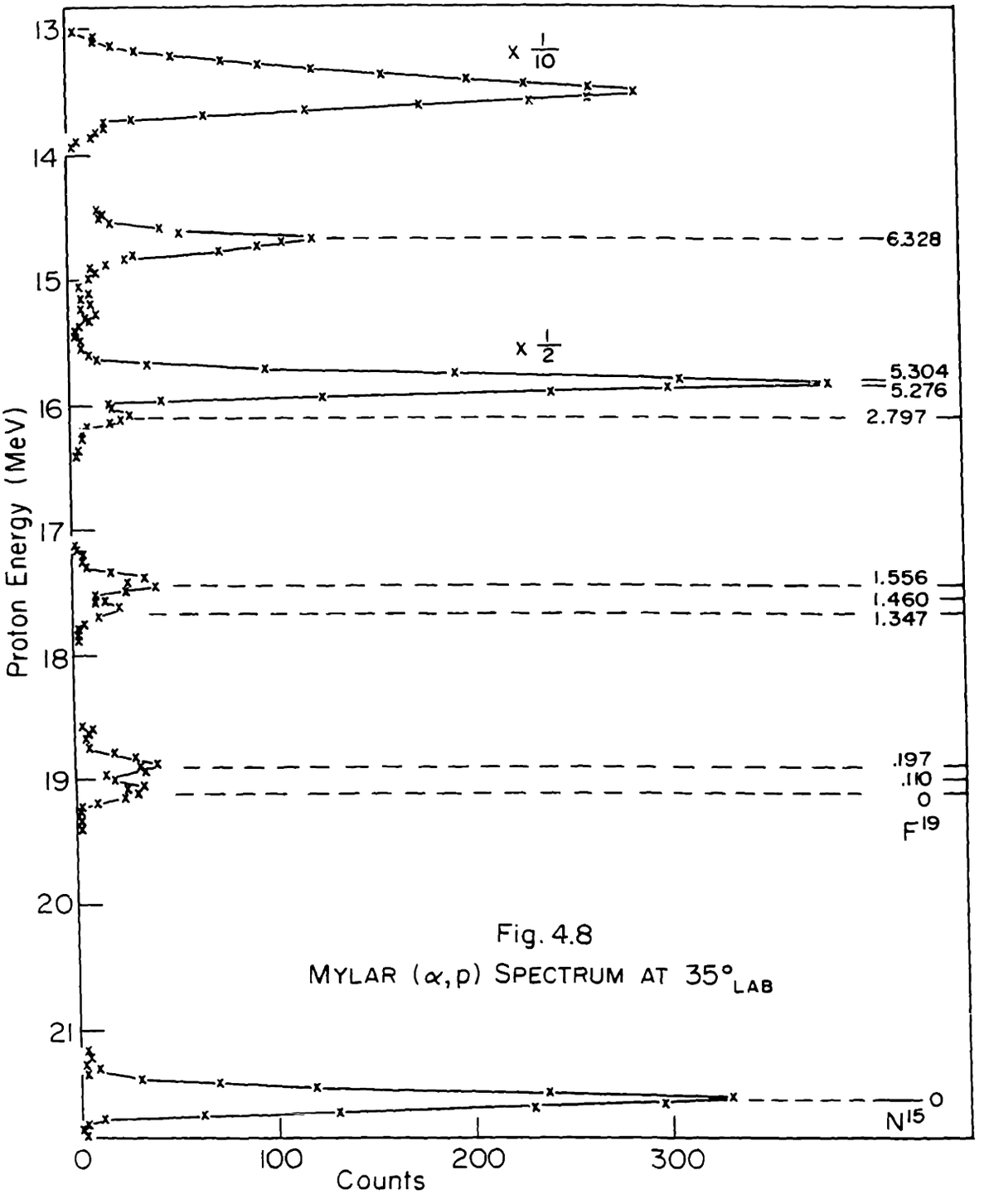

Fig. 4.8

MYLAR (α, p) SPECTRUM AT $35°_{LAB}$

the energy levels in N^{15} at 5.276 and 5.304 Mev. Since it was not possible to resolve these levels, the average energy (5.290 Mev) was associated with the peak. Using this excitation energy, the energy difference between this peak and the N^{15} ground state peak was calculated from kinematics (including energy losses in the target). At 35 degrees this energy difference, which was used as an energy calibration, was $5.715 \pm .015$ Mev where the error is due to the uncertainty in the peak assignment. The broad peak between 13 and 14 Mev was due to protons ejected from the Mylar target by elastic collisions with alpha particles.

For the five targets studied in this experiment, (α,p) spectra were recorded every 5 degrees from 20 degrees to about 90 degrees. To obtain the best resolution (see Section 4.2) the target was rotated along with the detector so that the angle between the emitted proton path and the plane of the target was maintained at 10 degrees.

The spectra were recorded while a preset amount of charge entered the Faraday cup. Charge was measured by a current integrator fed by the beam microammeter. The integrator produced pulses whose number was proportional to the input charge. These pulses were counted by a register connected to a system which automatically stopped the multichannel analyzer when a preset number of register counts was reached. In addition, the pulses were counted in the first channel of the 1024 channel analyzer. Since these pulses were subject to essentially the same dead time losses as any other pulse, the ratio of the counts in the first channel to the number preset on the register gave the average live time of the analyzer during the run.

The relative normalization of different proton spectra for the angular distribution measurements was accomplished using the number of elastic alphas recorded by the in-plane monitor. The in-plane monitor was

used rather than the integrator or fixed monitor (at 90° to the (α,p) scattering plane) because: 1) Using a monitor counter automatically took into account the target angle and any inhomogeneities in the target; 2) The moveable monitor (in-plane) could be easily checked to ensure that it was centered on a relatively flat part of the elastic cross-section; 3) The probability for scattering into the fixed monitor would be sensitive to vertical fluctuations in the position of the beam, while such fluctuations would have very little effect on the (α,p) reaction or elastic α scattering in the horizontal plane. The ratio of the two monitors was normally constant to about ± 5% during a run. Also, the ratio of the number of counts in the in-plane monitor multiplied by the cosine of the target angle to the number of integrator counts was normally constant within about ± 5%.

At the end of each (α,p) run, alpha particle spectra were recorded over a small angular region around the position of the first relative maximum in the elastic cross-section (at about 30°). These spectra were taken with the ΔE counter using the same setup (slits and target) that was used for the (α,p) spectra. In this way, the (α,p) normalization was determined relative to the elastic alpha scattering cross-section for the same target nucleus. The elastic cross-sections for all the target nuclei studied in this experiment have been measured at the M.I.T. cyclotron (L2) using Rutherford scattering from gold as the absolute normalization. The values used for normalization of the (α,p) data are given in Table 4.4.

Target	$\theta_{C.M.}$ (degrees)	$d\sigma/d\Omega$ (mb/steradian)	
		C.M.	LAB
Ca^{40}	32.9	100	118
Ca^{42}	32.7	94.1	110
Ca^{44}	32.6	94	109
Ca^{48}	32.4	93	107
Ti^{48}	32.4	110	126

The errors in the cross-sections are roughly ±10%.

Table 4.4

Elastic Alpha Cross-Sections at 30° LAB

4.5 Data Analysis

The data analysis for this experiment consisted of obtaining from each 1024 channel spectrum the mean positions and areas of the peaks of interest. Q-values and excitation energies were obtained from the positions and differential cross-sections were obtained from the areas.

During the experiment some energy levels and the ground state angular distributions were obtained from a rough analysis of the data. Later, a more complete analysis of the data was carried out using a small digital computer (Digital Equipment Corporation PDP-1).

The data analysis program (originally written by T. Provost) was developed so that the computer could do the purely computational work while the operator made the decisions about the quality of the fit to the data (see below).

For isolated peaks, the areas were easily obtained by summing the data points (minus the background level) in each peak. For multiple peaks, the data must be fit by a sum of peaks whose shapes have been determined from an isolated peak. For the (α,p) data the isolated peaks had a gaussian shape to a good approximation.

Thus, the analysis consisted of visually comparing the data with a computer generated curve consisting of a linear background plus gaussian shaped peaks whose parameters (position, height and width) could be varied by the operator until a good fit was obtained. The width of each gaussian used to fit a spectrum was usually held fixed at the value obtained by fitting an isolated peak in the same spectrum.

The area and other parameters of each gaussian were then calculated by the computer.

The first step in using the computer was to transfer the data from the paper tapes obtained from the analyzer to a magnetic tape. Any spectrum on the magnetic tape could be located quickly by the data analysis program.

Once a particular spectrum had been located, the data was transferred to the computer memory and then displayed on a 10 inch oscilloscope. A 64 channel segment of the data was selected and spread out to fill the screen. The portion of this region to be fit was defined by left and right valley points, and then the background for this region was indicated by adjusting the heights and slopes of two straight lines which corresponded to an upper and lower estimate of the background. Next, the positions (heights and locations) of up to five peaks in the fit region were indicated and the sum of the background (average of upper and lower estimates) and the indicated gaussian curves was displayed with the data. The gaussian parameters and the background height were varied by the operator until a satisfactory fit was obtained. The quality of the fit was judged mainly from the visual display, but two numbers calculated by the computer were also helpful. They were:

$$g = (A_D - A_F)^2/A_D \quad \text{where} \quad A_D = \sum X_D \quad \text{and} \quad A_F = \sum X_F$$

and $$X = \frac{1}{n} \sum (X_D - X_F)^2/X_D$$

X_D and X_F are the values of the data and fit points and n is the number of channels summed. The sums are taken from the left valley to the right valley. The number "g" gave an indication of the agreement between the data and fit areas and for most fits was less than about

0.2. The number "X" was used only to judge between two fits to the same data.

When a satisfactory fit had been obtained it was stored for a plot (see below) and the various parameters were written on to a magnetic tape which was later printed by an IBM 1401 computer. For each gaussian displayed, the output consisted of the area, location, height, and background as well as a percentage error based on the formula:

$$E = (100/A)\left[A + B + (dB)^2 + 2A_{OL}\right]^{1/2} \qquad (4.5)$$

Here A is the area of the gaussian, B is the background area, dB is the uncertainty in the background area ($\frac{1}{2}$ of the difference between the upper and lower estimates) and A_{OL} is the overlap area between the peak of interest and all other peaks displayed (see Figure 4.9). To evaluate dB and B, the peak width at the background was taken to be 2.5 x (F.W.H.M.). Equation 4.5 represents a combination of the statistical error in the measured area (A + B) and the uncertainties due to background subtraction and peak separation. The factor $2A_{OL}$ is simply an estimate of the error involved in fitting multiple peaks and extracting the individual areas.

The final relative errors for the angular distributions include an additional error estimated from the differences between repeated measurements. Because of this error, the minimum relative error was taken to be $\pm$ 10%.

For each fit peak, the scattering angle, target angle, peak location, normalized area (area/monitor), fractional error and the identification number of the spectrum were punched out on paper tape. This information was later transferred to a magnetic tape from which the 1401 computer punched cards which provided the input to a program

Figure 4.9 Errors in Fit Peaks

$$E = \sqrt{A + B + (dB)^2 + 2A_{OL}}$$

$$B = \omega b$$

$$dB = \omega db \qquad \omega = 2.5 \text{ F.W.H.M.}$$

$$db = \frac{1}{2}(b_{max} - b_{min})$$

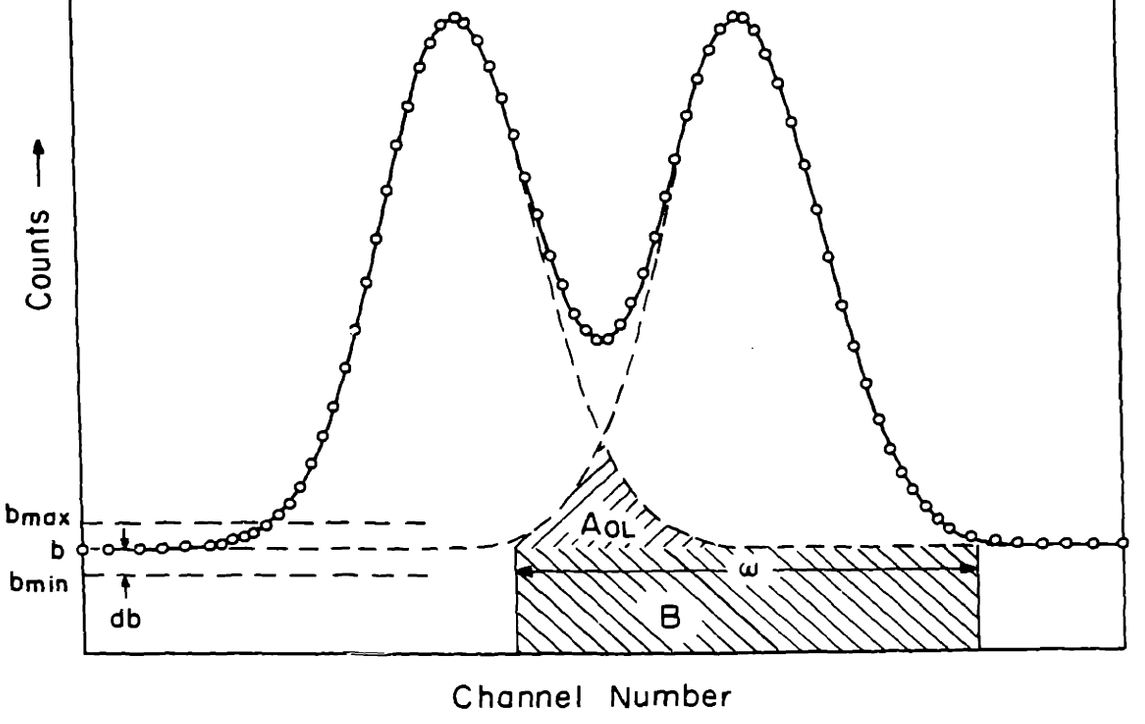

(called MANIB and written by E.P. Lippincott and S. Smith) for the IBM 7044 computer. This program calculated excitation energies and identified the various peaks as well as transforming the differential cross-sections to the center of mass system.

When the output for all the peaks of interest in a spectrum had been obtained, the entire spectrum and the fit peaks (which were stored earlier) were written on to the output magnetic tape. After being printed by the 1401 computer this tape produced a plot of the data and the fit. An example of such a plot is shown in Figure 4.10 for part of the $Ca^{48}(\alpha,p)Sc^{51}$ spectrum. The solid line has been drawn through the fit points.

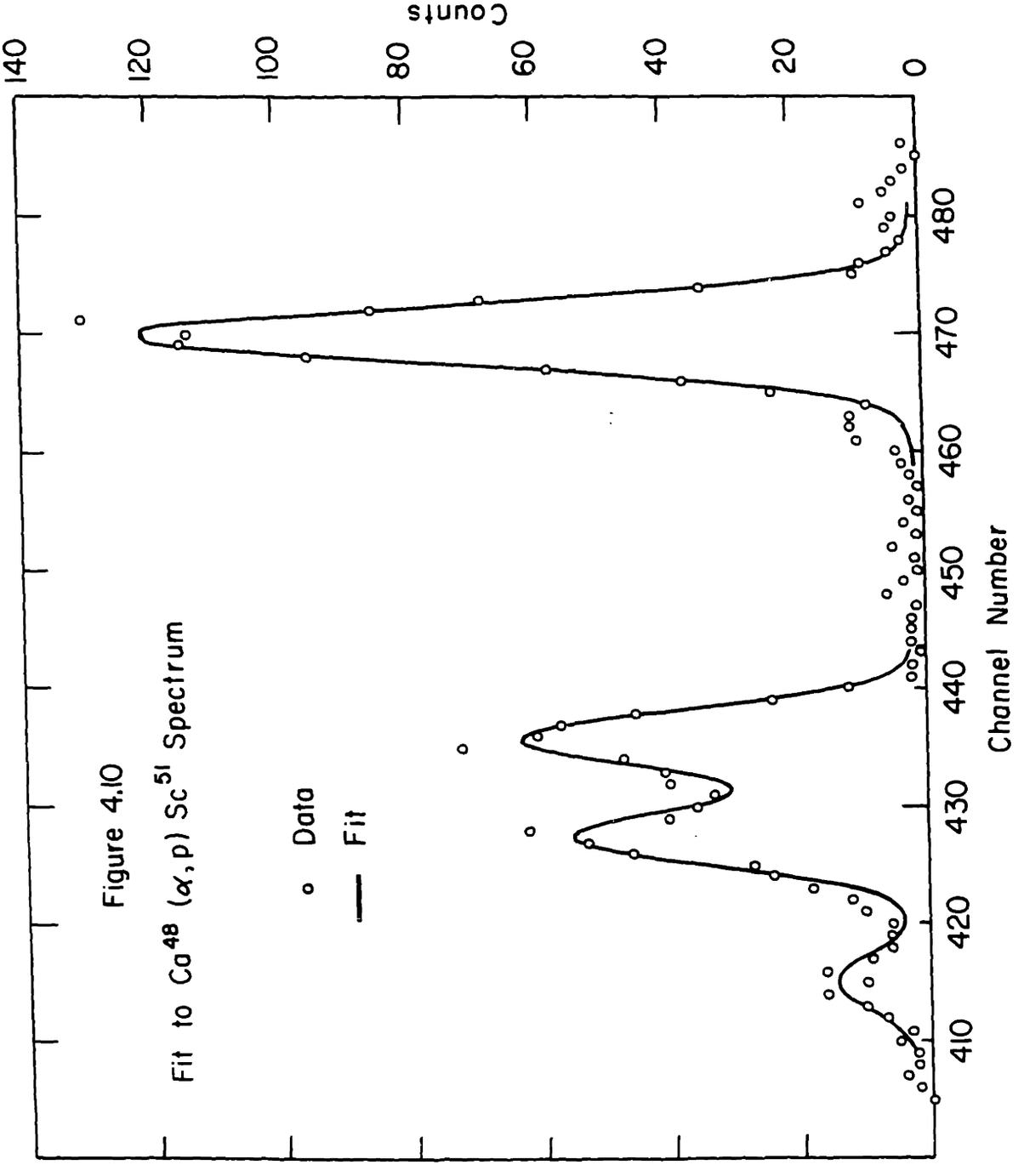

Figure 4.10

Fit to Ca^{48} (α, p) Sc^{51} Spectrum

CHAPTER 5

THEORY

5.1 Distorted Wave Model for (α,p) Stripping Reactions

An expression for the DWBA differential cross-section for pick-up (p,α) reactions has been derived by B.F. Bayman and E. Rost (B3). J.A. Nolan (N3) has summarized their work and has included spin orbit effects in the proton channel. This section gives a summary of this derivation, including spin orbit effects, as applied to (α,p) reactions. Since the DWBA calculations were done with the Oak Ridge code JULIE, the notation used here is consistent with that used by G.R. Satchler in his general formulation of the distorted waves theory of direct nuclear reactions (S3).

In the distorted-wave Born approximation the cross-section for the stripping reaction A(α,p)B is given by:

$$d\sigma/d\Omega = k_p/k_\alpha \frac{\mu_\alpha \mu_p}{(2\pi\hbar^2)^2} \frac{1}{(2J_A+1)} \sum_{\substack{M_A M_B \\ m_p}} |T|^2 \qquad (5.1)$$

where the transition amplitude, T, is:

$$T = \sum_{m_p'} \int d\vec{r}_{\alpha A} \int d\vec{r}_{pB}\, \phi^{(-)*}_{m_p, m_p'}(\vec{k}_p, \vec{r}_{pB})\, \mathcal{J} \langle \psi^{J_B}_{M_B}\, \psi^{s_p}_{m_p'} | V | \psi^{J_A}_{M_A}\, \psi^{0}_{k\,0} \rangle\, \phi^{(+)}_{(\vec{k}_\alpha, \vec{r}_{\alpha A})} \qquad (5.2)$$

For these equations and the rest of this sections the coordinates used are listed and defined in Table 5.1 and the other symbols not explained in the text are explained in Table 5.2. In equation 5.2 the matrix element of the interaction, V, responsible for the (α,p) reaction, involves integrations over the internal coordinates (independent of $\vec{r}_{\alpha A}$ and $\vec{r}_{pB}$) of the target nucleus A, the final nucleus B, and the alpha particle. The proton is assumed to be a point particle and so its internal wave function is simply a spinor: $\psi^{s_p}_{m_p'} = \chi^{1/2}_{m_p'}$. The

Coordinate	1	2	
$\vec{r}_{\alpha A}$	A	α	$\vec{r}_{\alpha A} = \frac{1}{4}(\vec{r}_p + 3\vec{r}_t)$
$\vec{r}_{pB}$	B	p	$\vec{r}_{pB} = \vec{r}_p - \left(\frac{m_B - m_A}{m_B}\right)\vec{r}_t$
$\vec{r}_{n_1}$	A	n_1	} transferred particles
$\vec{r}_{n_2}$	A	n_2	
$\vec{r}_{p_1}$	A	p_1	
$\vec{r}_p$	A	p	
$\vec{r}_t$	A	t	$\vec{r}_t = 1/3\ (\vec{r}_{n1}+\vec{r}_{n2}+\vec{r}_{p1})$
$\vec{s}$	A	t	$\vec{s} = \sqrt{3}\,\vec{r}_t$
$\vec{\rho}_1$	n_1	n_2	$\vec{\rho}_1 = \frac{\vec{r}_{n2}-\vec{r}_{n1}}{\sqrt{2}}$
$\vec{\rho}_2$	(n_1+n_2)	p_1	$\vec{\rho}_2 = \frac{2\vec{r}_{p1}-\vec{r}_{n1}-\vec{r}_{n2}}{\sqrt{6}}$
$\vec{\rho}_3$	t	p	$\vec{\rho}_3 = \frac{\sqrt{3}}{2}(\vec{r}_p - \vec{r}_t)$

Each coordinate represents the separation between the center of mass of the particle(s) in column 1 and the center of mass of those listed in column 2.

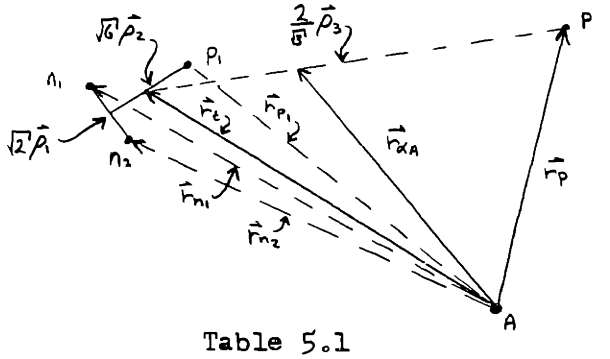

Table 5.1

Coordinates Used in Chapter 5

$\vec{k}_\alpha$, $\vec{k}_p$	Asymptopic relative momenta (units of $\hbar$) of α - target and proton-daughter systems.
μ_α, μ_p	Reduced masses of α - target and proton-daughter systems.
$\Phi^{(+)}$, $\Phi^{(-)}$	Incoming and outgoing distorted waves of relative motion satisfying $\left\{ \nabla^2 + k^2 - \left(2\mu/\hbar^2\right)\left[U(r) + U_c(r)\right] \right\} \Phi(\vec{k};\vec{r}) = 0$ where U(r) is the optical model potential (including spin-orbit coupling) and $U_c(r)$ is the Coulomb potential.
$\mathcal{J}$	Jacobian of the transformation to coordinates $\underset{\sim}{r}_{\alpha A}$ and r_{pB}.
ϕ, χ	Orbital wave functions and spinors.
m_A, m_B	Masses of target and daughter nuclei.
ψ^{jn}	Wave function of neutron in shell j_n.
L,J	Orbital and total angular momentum transfered during the (α,p) reaction. L is that value of $J \pm \frac{1}{2}$ with the correct parity: $(-1)^L = (-1)^{\ell_p}$
n, ℓ	Principle and orbital quantum numbers of nucleons. n = n(shell model) - l; n(shell model) = number of nodes in radial wave function (including origin) minus ℓ.

Table 5.2

Symbols Used in Chapter 5

matrix element also involves sums over the spins of the four nucleons in the alpha particle; the three transferred nucleons (n_1, n_2, and p_1, referred to as the "triton") and the final proton (p). It is assumed that the interaction involves only these four nucleons, with the target nucleus considered inert; i.e. its state is unchanged during the transition. We therefore perform a fractional parentage expansion of the final nuclear wave function in terms of the target wave function:

$$\psi^{J_B}_{M_B} = \sum_{I, J_A', J} \left(J_A' ; ([j_n j_n]^I j_p)^J \right\} J_B \Big) \left[\psi^{J_A'}_{M_A}(\text{core})\, \psi^{IJ}_{M}(\text{triton}) \right]^{J_B}_{M_B} \qquad (5.3)$$

The fractional parentage coefficients, $(\; ; \; \} \;)$, are defined by this equation which, in general, should involve sums over j_n and j_p. These sums have been eliminated by the simplifying assumption that the neutrons go only into the shell j_n and the proton goes only into the shell j_p. The brackets in 5.3 indicate vector coupling of the angular momenta:

$$\left[\psi^{j_1} \psi^{j_2} \right]^K_M \equiv \sum_{m_1 m_2} (j_1 j_2 m_1 m_2 | K M)\, \psi^{j_1}_{m_1} \psi^{j_2}_{m_2}$$

The "triton" wave function is a result of the coupling of the neutron pair and the proton:

$$\psi^{IJ}_{M}(\text{triton}) = \left(\left[\psi^{j_n}(n_1)\, \psi^{j_n}(n_2) \right]^I \psi^{j_p}(p_1) \right)^J_M$$

The introduction of the expansion 5.3 allows us to perform the integration over the "core" internal coordinates in 5.2, leaving us with integrals over the three alpha particle internal coordinates $\vec{\rho}_1, \vec{\rho}_2$ and $\vec{\rho}_3$. In order to do the $\vec{\rho}_1$, and $\vec{\rho}_2$ integrals we assume that the interaction depends only on $\vec{\rho}_3$. That is, we assume that V depends only on the separation between the proton and the center of mass of the "triton":

$$V = V_{pt} = V(|\vec{r}_p - \vec{r}_t|)$$

With this assumption it becomes convenient to transform the cross-section calculation to the coordinates $\vec{r}_p$ and $\vec{r}_t$:

$$\frac{d\sigma}{d\Omega} = \frac{k_p}{k_\alpha}\frac{1}{(2\pi\hbar^2)^2}\frac{(2J_B+1)}{(2J_A+1)} f_p f_n (f_n-1) \sum_{J M m_p}\frac{1}{(2J+1)} \left| \sum_I \left(J_n ; (L j_n j_n)^I j_p)^J \right\} J_B \right)$$

$$\times \sum_{m_p} \int d\vec{r}_p \int d\vec{r}_t \, \phi^{(-)*}_{m_p, m_p'}\left(\vec{k}_p, \vec{r}_p - \frac{m_B - m_A}{m_B}\vec{r}_t\right) \langle \psi^{IJ}_n(\text{triton})\, \chi^{1/2}_{m_p'} | V_{pt} | \phi^0_0 \chi^0_0 \rangle \phi^{(+)}_{\vec{k}_\alpha}\left(\vec{r}_p + \frac{3}{4}\vec{r}_t\right) \Bigg|^2 \quad (5.4)$$

Here f_p is the number of protons in the shell j_p, and f_n is the number of neutrons in the shell j_n of the final nucleus.

The α particle internal wave function is assumed to be:

$$\psi^0_{\alpha 0} = \phi^0_0 \chi^0_0$$

where

$$\phi^0_0 = 2^{-3/2}\left(\frac{\beta}{\pi}\right)^{9/4} \exp\left[-\beta/16 \sum_{i,j=n_1 n_2 p_1 p_2} |\vec{r}_i - \vec{r}_j|^2\right] = 2^{-3/2}\left(\frac{\beta}{\pi}\right)^{9/4} \exp\left[-\beta/2\,(\rho_1^2 + \rho_2^2 + \rho_3^2)\right]$$

The size parameter β is related to the rms radius of the alpha particle.

Also,

$$\chi^0_0 = \left[\chi^{1/2}_{(\sigma_{n1})}\chi^{1/2}_{(\sigma_{n2})}\right]^0_0 \left[\chi^{1/2}_{(\sigma_{p1})}\chi^{1/2}_{(\sigma_{p2})}\right]^0_0$$

We approximate the nuclear radial wave functions by those for a 3-dimensional harmonic oscillator:

$$\phi^{nl}_m(\vec{r}) = U_{nl}(r)\, Y^l_m(\hat{r})$$

where:

$$U_{nl}(r) = \left[\frac{2^{l-n+2}(2l+2n+1)!!\,\alpha^{3/2}}{\sqrt{\pi}\; n!}\right]^{1/2} (\alpha^{1/2} r)^l e^{-\frac{\alpha r^2}{2}} \sum_K (-1)^K 2^K \frac{n!}{K!(n-K)!}\frac{(\alpha r^2)^K}{(2l+2K+1)!!}$$

$\alpha = \frac{m\omega}{\hbar}$ is the oscillator parameter.

In order to carry out the $\vec{\rho}_1$ and $\vec{\rho}_2$ integrations in 5.4, we must transform the "triton" wave function to these coordinates. At the same time, we transform to L-S coupling in order to perform the spin sums. This is done using a technique introduced by Mang (M2). We expand the "triton" wave function in a series of products of spin and orbital functions which are functions of the "triton" internal coordinates $\vec{\rho}_1$

and $\vec{\rho}_2$ and the center of mass coordinate $\vec{S}$:

$$\psi^{IJ}_M(\text{triton}) = \left\{\left[\psi^{j_n}(\vec{r}_{n_1}\sigma_{n_1})\psi^{j_n}(\vec{r}_{n_2}\sigma_{n_2})\right]^I \psi^{j_p}(\vec{r}_{p_1}\sigma_{p_1})\right\}^J_M$$

$$= \sum_{\substack{\nu_1\lambda_1,\nu_2\lambda_2\\ \nu_3\lambda_3\Lambda L}} C^{IJ}_{\nu_1\lambda_1\nu_2\lambda_2\nu_3\lambda_3\Lambda L}\left[\left\{\left[\phi^{\nu_1\lambda_1}(\vec{\rho}_1)\phi^{\nu_2\lambda_2}(\vec{\rho}_2)\right]^\Lambda \phi^{\nu_3\lambda_3}(\vec{S})\right\}^L\left[\chi^{1/2}(\sigma_{n_1})\chi^{1/2}(\sigma_{n_2})\right]^0\chi^{1/2}(\sigma_{p_1})\right]^J_M \quad (5.5)$$

+ neutron spin triplet term.

The neutron spin triplet term makes no contribution to the cross-section since the two neutrons are originally in a singlet state in the α particle and the interaction is assumed to be spin independent. When the expansion (5.5) is introduced into the matrix element in 5.4 and the $\vec{\rho}_1$ and $\vec{\rho}_2$ integrations as well as the sums over the nucleon spins are carried out, the expression obtained involves only certain sums of the C coefficients in 5.5. These sums can be evaluated in the following manner: by setting $\vec{r}_{n_1} = \vec{r}_{n_2} = \vec{r}_{p_1} = r\hat{z}$ and $\sigma_{n_1} = 1/2$; $M = \sigma_{n_2} = \sigma_{p_1} = -1/2$ in 5.5 we obtain an equation of the form:

$$U^2_{n_n\ell_n}(r)\,U_{n_p\ell_p}(r) = \sum_\nu A_{\nu L}\,U_{\frac{N-L}{2}-\nu,L}(\sqrt{3}r) \quad (5.6)$$

Here N is the total number of oscillator quanta: $N = 2n_p + \ell_p + 2(2n_n + \ell_n)$ Then the coefficients $A_{\nu L}$ contain the same sums of C coefficients needed in 5.4 to evaluate the result of the $\vec{\rho}_1, \vec{\rho}_2$ integrations. Thus the final result can be expressed in terms of the coefficients $A_{\nu L}$ which are chosen to satisfy 5.6 for all values of r.

In summary, the cross section can be written:

$$\frac{d\sigma}{d\Omega} = \sum_{\substack{J\\ L = J\pm 1/2\ ;\ (-1)^L = (-1)^{\ell_p}\ ;\ S = 1/2}} S^{J_A}_{J_B J}\ \sigma_{LSJ}(\theta) \quad (5.7)$$

where the spectroscopic factor is given by:

$$S^{J_A}_{J_B J} = f_p f_n (f_n - 1)\,2\frac{(2J_B+1)}{2J_A+1}\left[\sum_I \left(J_A; \left[(j_n j_n)^I j_p\right)^J\right\} J_B\right)\frac{(J_{j_p}\,1/2\,-1/2\,|I\,0)(j_n j_n\,1/2\,-1/2\,|I\,0)}{\sqrt{2I+1}}\right]^2 \quad (5.8)$$

and the reduced cross section is:

$$\sigma_{L S J}(\theta) = \frac{\mu_\alpha \mu_p}{(2\pi\hbar^2)^2} \frac{k_p}{k_\alpha} \sum_{M m_p} \left| \beta_{SJ}^{L M m_p}(\theta) \right|^2 \tag{5.9}$$

where:

$$\beta_{SJ}^{L M m_p}(\theta) = \frac{(i)^{-L}}{\sqrt{2J+1}} \sum_{m' m_p'} (-1)^{1/2 - m_p'} (L S m' - m_p' | J M - m_p)$$

$$\times \int d\vec{r}_p \int d\vec{r}_t \, \phi^{(-)*}_{m_p m_p'}(\vec{k}_p, \vec{r}_p - \tfrac{m_B - m_A}{m_B} \vec{r}_t) \, f^{(\vec{r}_p, \vec{r}_t)}_{L S J m'} \, \phi^{(+)}(k_\alpha, \tfrac{\vec{r}_p + 3\vec{r}_t}{4}) \tag{5.10}$$

The form factor here is:

$$f^{(\vec{r}_p, \vec{r}_t)}_{L S J m'} = \frac{(2j_n+1)\sqrt{2j_p+1}}{16(\alpha+\beta)^3 \pi^{5/4}} \beta^{9/4} V(|\vec{r}_p - \vec{r}_t|) \, e^{-\frac{3\beta}{8}|\vec{r}_p - \vec{r}_t|^2} \left(\sum_{\nu=0}^{\frac{N-L}{2}} A_{\nu L} \left[\tfrac{\beta-\alpha}{\beta+\alpha}\right]^\nu U_{\frac{N-L}{2}-\nu, L}(\sqrt{3}\, r) \right) Y^L_{m'}(\hat{r}_t) \tag{5.11}$$

In order to use the code JULIE we must reduce the 6-dimensional integral in 5.10 to a 3-dimensional one. To do this we use the zero range approximation. That is, we assume:

$$V(|\vec{r}_p - \vec{r}_t|) \, e^{-\frac{3\beta}{8}|\vec{r}_p - \vec{r}_t|^2} = K \, \delta(\vec{r}_p - \vec{r}_t)$$

With this assumption equation 5.10 becomes:

$$\beta_{SJ}^{L M m_p}(\theta)_{ZR} = (i)^{-L} \sum_{m' m_p'} (-1)^{1/2 - m_p'} (L S m' - m_p' | J M - m_p)$$

$$\times \int d\vec{r} \, \phi^{(-)*}_{m_p m_p'}(\vec{k}_p, \tfrac{m_A}{m_B}\vec{r}) \, \frac{F_L(r)}{\sqrt{2J+1}} \, Y^L_{m'}(\hat{r}) \, \phi^{(+)}(\vec{k}_\alpha, \vec{r}) \tag{5.12}$$

with the zero range from factor defined by:

$$F_L(r) = B \frac{(2j_n+1)\sqrt{2j_p+1}}{(\alpha+\beta)^3} \beta^{9/4} \sum_\nu A_{\nu L} \left[\tfrac{\beta-\alpha}{\beta+\alpha}\right]^\nu U_{\frac{N-L}{2}-\nu, L}(\sqrt{3}\, r) \tag{5.13}$$

The factor B is the same for all (α,p) reactions and will be used as an overall normalization of the theory. In practice, the form factor given by equation 5.13 was calculated separately and used as input to JULIE which calculated the reduced cross-section given by equation 5.9 using $\beta_{SJ}^{L M m_p}(\theta)_{ZR}$ as given by 5.12.

5.2 Form Factors

In the previous section it was shown that the (α,p) stripping cross-section could be calculated by the DWBA code JULIE using the form factor:

$$F_L(r) = B\,\frac{(2j_n+1)\sqrt{2j_p+1}\,\beta^{9/4}}{(\alpha+\beta)^3}\sum_\nu A_{\nu L}\left[\frac{\beta-\alpha}{\beta+\alpha}\right]^\nu U_{\frac{N-L}{2}-\nu,L}(\sqrt{3}\,r) \qquad (5.13)$$

with the coefficients $A_{\nu L}$ chosen to satisfy the equations:

$$U^2_{n_n l_n}(r)\,U_{n_p l_p}(r) = \sum_\nu A_{\nu L}\,U_{\frac{N-L}{2}-\nu,L}(\sqrt{3}\,r) \qquad (5.6)$$

For the cases involving particles outside of the $1f_{7/2}$ shell, the DWBA calculations were done at Oak Ridge (by R.M. Drisko and P.G. Roos). Their version of JULIE calculated the form factor (as given in 5.13 except for the factor $(2j_n+1)\sqrt{2j_p+1}$) for any $n_n l_n j_n$ and $n_p l_p j_p$, and then evaluated the DWBA cross-section (equations 5.9 and 5.12).

For the cases involving only $1f_{7/2}$ particles (i.e. $n_n = n_p = 0$; $l_n = l_p = 3$; $j_n = j_p = 7/2$) equation 5.6 can be solved explicitly and the form factor becomes:

$$F_L(r) = B'\,\frac{\beta^{9/4}\alpha^{27/4}2^{4/2}(10+L)!!}{(\alpha+\beta)^{15/2}}\,e^{-\frac{3\alpha}{2}r^2}\sum_K (-2)^K\,\frac{(\frac{9-L}{2})!\,[\frac{3}{2}(\alpha+\beta)r^2]^{\frac{1}{2}+K}}{K!(\frac{9-L}{2}-K)!(2L+2K+1)!!} \qquad (5.14)$$

A program obtained from B.F. Bayman was used to calculate this $(f7/2)^3$ form factor which was then punched out on cards and used as input for the M.I.T. version of JULIE. The two different programs were normalized by doing one $(f7/2)^3$ calculation by both methods.

In order to obtain an estimate for the alpha particle size parameter, β, we can calculate the mean square radius of the alpha

particle using a simple one-dimensional wave function with the same radial dependence as that used in the previous section:

$$\phi = \left(\frac{\beta}{\pi}\right)^{3/4} e^{-\frac{\beta}{2}r^2}$$

The mean square radius is:

$$\langle r^2 \rangle = \int \phi^* r^2 \phi \, d\vec{r}$$

With the above wave function this becomes:

$$\langle r^2 \rangle = \left(\frac{\beta}{\pi}\right)^{3/2} \int_0^\infty r^2 e^{-\beta r^2} 4\pi r^2 dr = \frac{3}{2\beta}$$

Using the value 1.63 fm (F1) for the rms alpha radius, we obtain:

$$\beta = \frac{3}{2\langle r^2 \rangle} = 0.56 \ \text{fm}^{-2}$$

The (α,p) angular distributions were found to be quite insensitive to changes in β, and therefore the value of 0.56 fm^{-2} was used for all the calculations.

The parameter for the single particle harmonic oscillator wave functions is:

$$\alpha = M\omega/\hbar$$

With $\hbar\omega$ = 8 Mev, this gives the value α = 0.19 fm^{-2}.

The calculated (α,p) angular distributions are sensitive to changes in the parameter α. Figure 5.1 shows the Ca^{40} (α,p) Sc^{43} ground state (7/2-) angular distribution calculated for α = .21 and α = .15, along with corresponding form factors calculated from equation 5.14. Values of α between 0.1 and 0.25 were tried and α = 0.15 was selected on the basis of agreement with the experimental $Ca^{40}(\alpha,p)Sc^{43}$ ground state angular distribution. This value of α was used for all of the DWBA calculations. The optical model parameters used for the DWBA calculations are given in Chapter 6.

The dependence of the form factors and the calculated angular distributions on the configurations of the transferred neutrons and

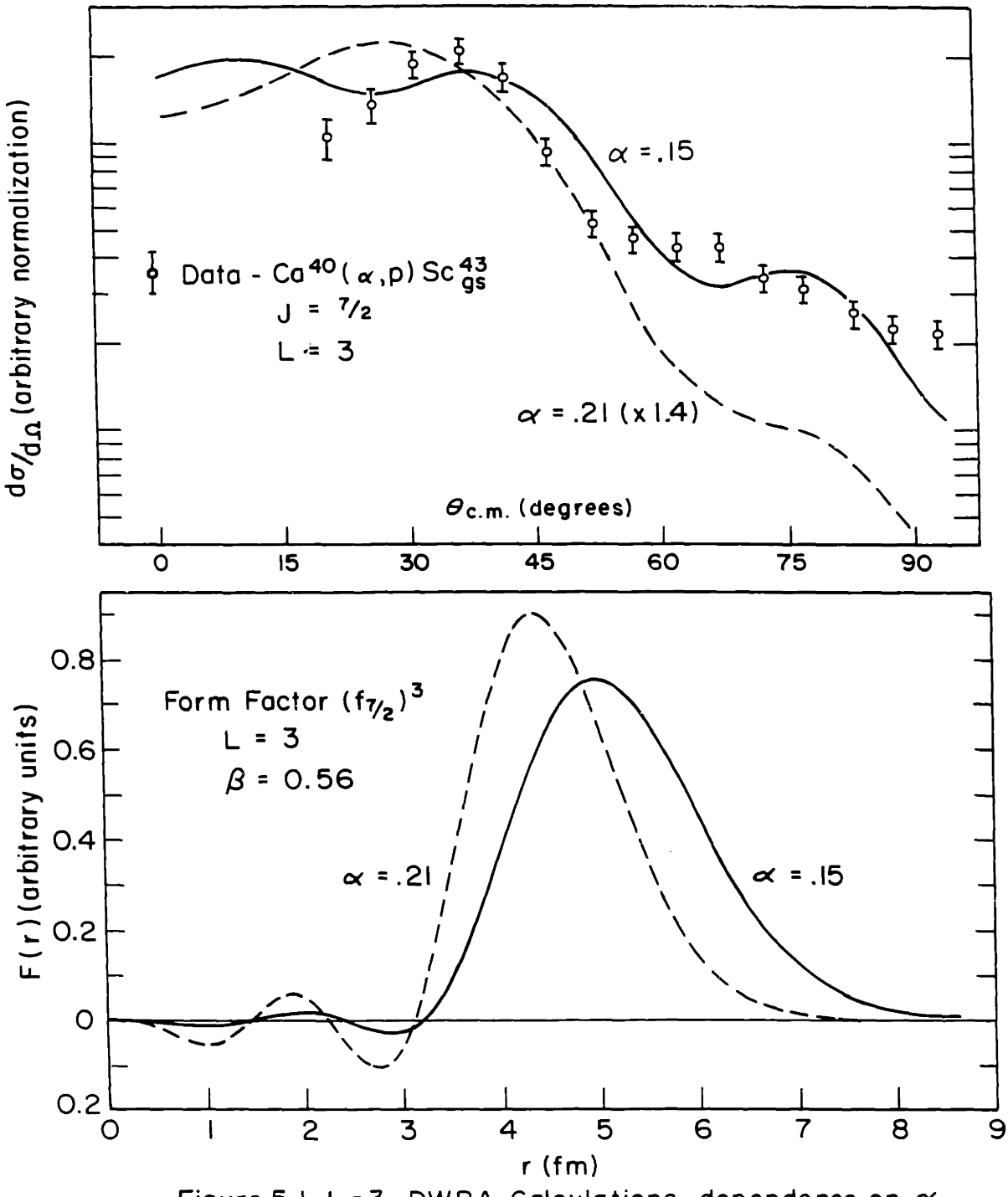

Figure 5.1 L = 3 DWBA Calculations - dependence on α.

proton is illustrated in Figures 5.2 and 5.3. Figure 5.2 shows the effect of putting the neutron pair in different shells with the proton going into the $1f_{7/2}$ shell in both cases. The dashed curve is for the neutrons going into the $1f_{7/2}$ shell, and the solid curve is for the neutrons going into the $2p_{3/2}$ shell. Both curves are for $J = 7/2$, $L = 3$.

Figure 5.3 shows the effect of putting the proton into different shells, with the neutrons going into the $1f_{7/2}$ shell in both cases. The dashed curve is for the proton (coupled with the neutrons to $J = 3/2$) going into the $f_{7/2}$ shell, and the solid curve is for the proton going into the $2p_{3/2}$ shell. In both cases $J = 3/2$ and $L = 1$.

5.3 Spectroscopic Factors

As shown in Section 5.1, when the neutron and proton shells involved in the reaction are both unique, we can write the (α,p) cross-section as an incoherent sum of terms corresponding to different angular momentum transfers (consistent with $|J_A - J_B| \leq J \leq J_A + J_B$):

$$\frac{d\sigma}{d\Omega} = \sum_J S_{J_B J}^{J_A} \, \sigma_{LSJ}(\theta) \tag{5.7}$$

The reduced cross-section $\sigma_{LSJ}(\theta)$, which is relatively independent of nuclear structure, contains the A, Z and Q dependence of the cross-section. The method of evaluating $\sigma_{LSJ}(\theta)$ using the DWBA code JULIE was outlined in Sections 5.1 and 5.2. Most of the nuclear structure information is contained in the spectroscopic factor:

$$S_{J_B J}^{J_A} = f_p f_n (f_n - 1) \frac{2(2J_B+1)}{2J_A+1} \left[\sum_I (J_A; (l_n j_n)^I j_p)^J \{J_B\} \frac{(J j_p \tfrac{1}{2} - \tfrac{1}{2} | I 0)\,(j_n j_n \tfrac{1}{2} - \tfrac{1}{2} | I 0)}{\sqrt{2I+1}} \right]^2 \tag{5.8}$$

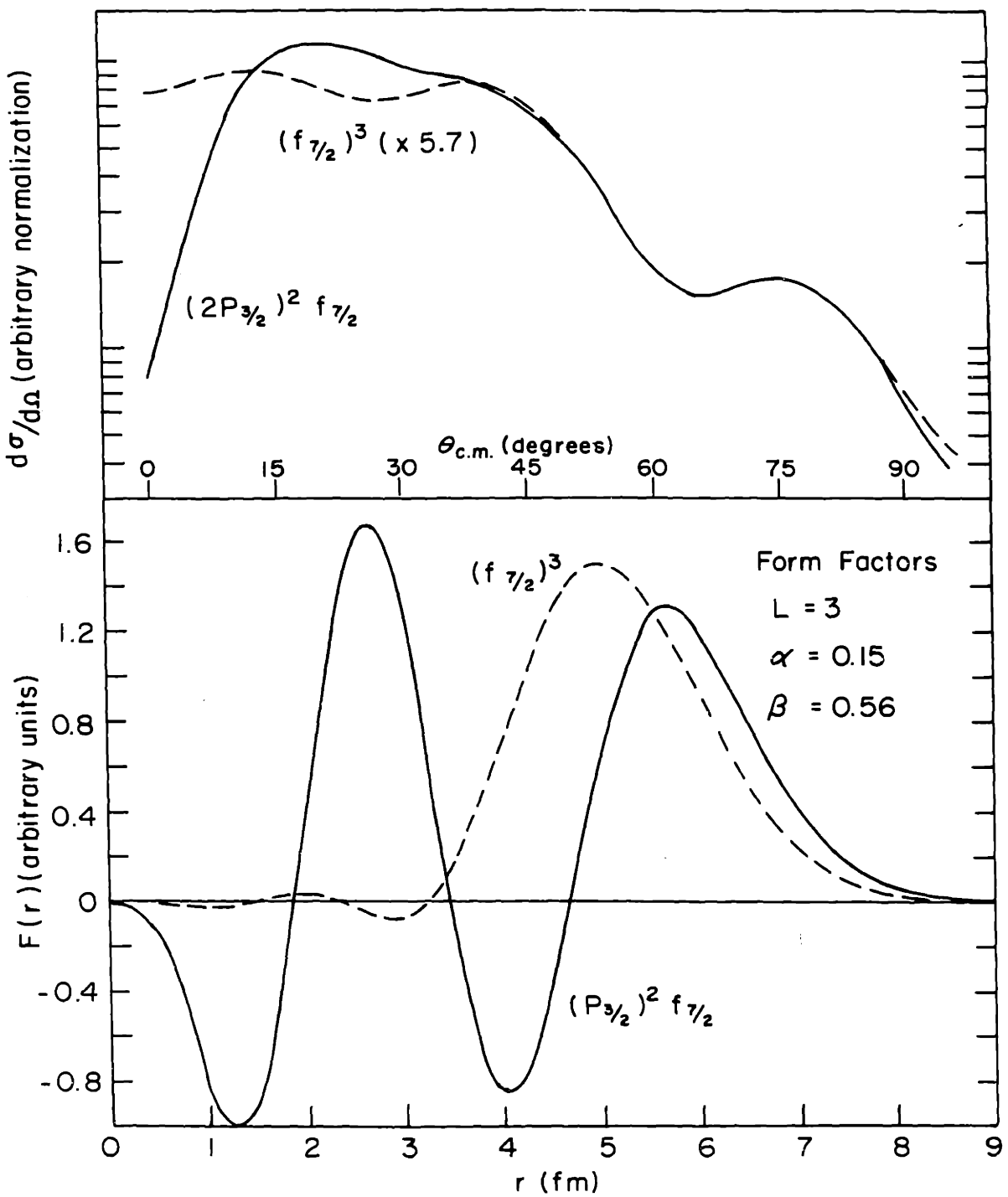

Figure 5.2 L=3 DWBA Calculations - dependence on configuration

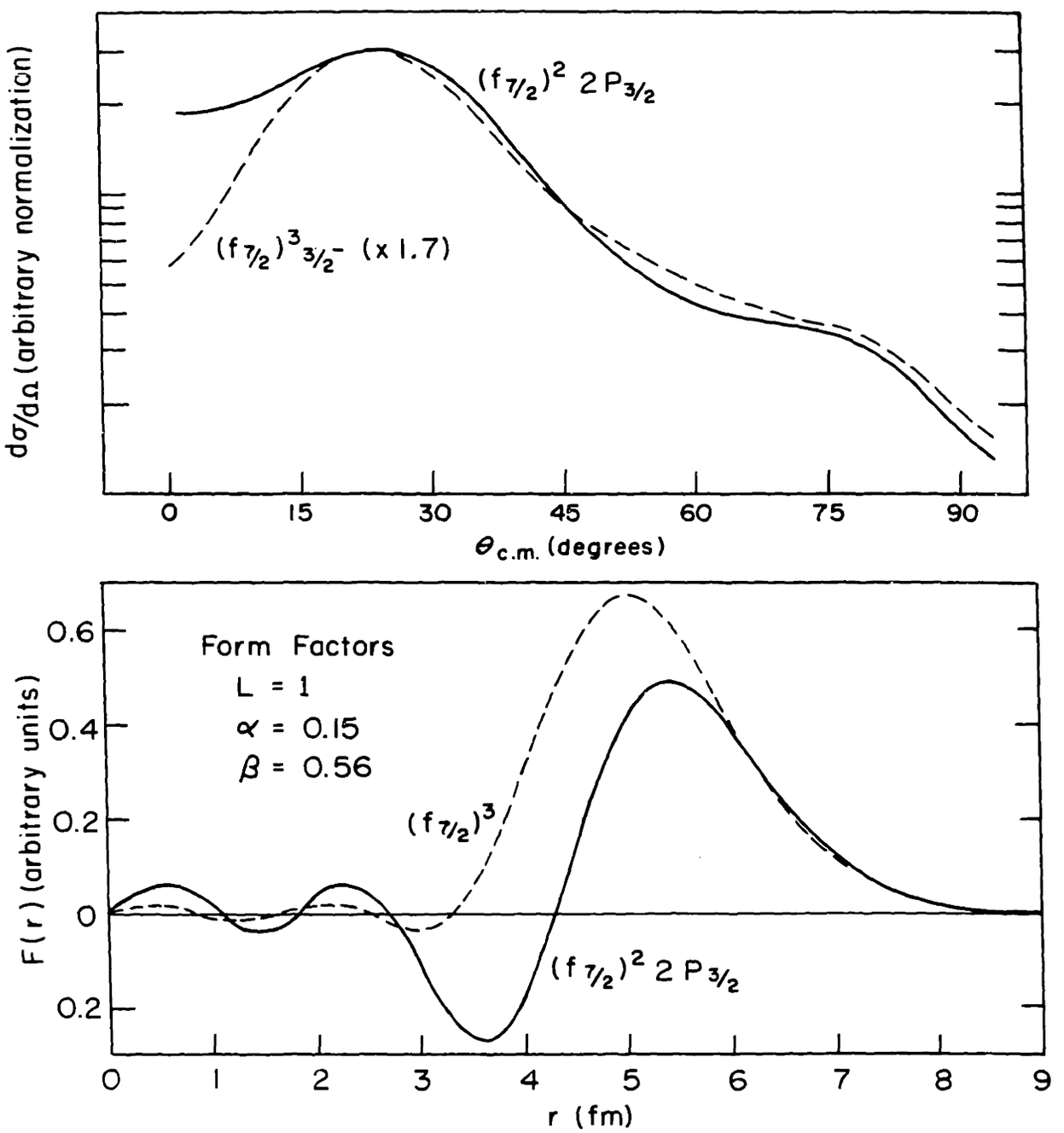

Fig. 5.3. L = 1 DWBA Calculations - dependence on configurations

This factor is a coherent superposition of terms corresponding to different angular momenta, I, of the transferred neutron pair. This type of coherence is the characteristic of many-particle transfer reactions which makes it possible for them to be sensitive to the relative phases of the components of the wave functions of the target and daughter nuclei. Bayman has discussed this type of sensitivity in terms of the Sc^{45} $(p,\alpha)Ca^{42}$ reaction (B4). This point will be illustrated in the next section (5.4) by a calculation of the relative strengths of the Ca^{40} $(\alpha,p)Sc^{43}$ and $Ca^{42}(\alpha,p)Sc^{45}$ ground state transitions.

The fractional parentage coefficient in equation 5.8 is defined by the expansion:

$$\psi^{J_B}_{M_B} = \sum_{I,J_n,J} (J_A; ([j_n j_n]^I j_p)^J\} J_B) \left[\psi^{J_A}_{M_n}(\text{core})\ \psi^{IJ}_{M}(\text{nucleon}) \right]^{J_B}_{M_B} \qquad (5.3)$$

The (α,p) spectroscopic factors will be evaluated using two types of wave functions: the shell-model wave functions of McCullen, Bayman and Zamick (M1, hereafter referred to as MBZ) and wave functions for neutrons and protons separately in states of good seniority.

Assuming Ca^{40} to have closed neutron and proton shells, the nuclei with N and Z between 20 and 28 may be described in terms of closed shells plus f_p=Z-20 protons and f_n= N-20 neutrons in the $f_{7/2}$ shell. Thus we can expand the target and final wave functions in terms of the nucleons outside of closed shells:

$$\psi^{J_A}_{M_A} = \sum_{\substack{J_n J_p \\ v_n v_p}} D_A(J_A; v_n J_n v_p J_p) \left[\psi_{1\ldots f_n-2}(j^{f_n-2}\, v_n J_n)\ \psi_{1\ldots f_p-1}(j^{f_p-1}\, v_p J_p) \right]^{J_A}_{M_A} \qquad (5.15a)$$

$$\psi^{J_B}_{M_B} = \sum_{\substack{J_n' J_p' \\ v_n' v_p'}} D_B(x J_B; v_n' J_n' v_p' J_p') \left[\psi_{1\ldots f_n}(j^{f_n} v_n' J_n')\ \psi_{1\ldots f_p}(j^{f_p} v_p' J_p') \right]^{J_B}_{M_B} \qquad (5.15b)$$

$\psi(j^f v J)$ is the totally antisymmetric state of f particles in the $f_{7/2}$ shell ($j \equiv 7/2$) with seniority v and angular momentum J. The symbol x distinguishes between different final states with the same J_B and M_B. The subscripts on the wave functions are particle variables. The determination of the coefficients D_A and D_B will be described later.

In order to evaluate the coefficients $(J_A; ([j_n j_n]^I \; j_p)^J \} \; x J_B)$, we perform separate fractional parentage expansions on the final state proton and neutron wave functions:

$$\psi_{1\ldots f_n}(j^{f_n} v_n' J_n') = \sum_{v_n J_n I} (j^{f_n-2}\, v_n\, J_n;\, j^2 I \} j^{f_n} v_n' J_n') \left[\psi_{1\ldots f_n-2}(j^{f_n-2} v_n J_n)\; \psi_{f_n-1,\, f_n}(j^2 I) \right]^{J_n'} \tag{5.16a}$$

$$\psi_{1\ldots f_p}(j^{f_p} v_p' J_p') = \sum_{v_p J_p} (j^{f_p-1}\, v_p\, J_p\, j \} j^{f_p} v_p' J_p') \left[\psi_{1\ldots f_p-1}(j^{f_p-1} v_p J_p)\; \psi_{f_p}(j) \right]^{J_p'} \tag{5.16b}$$

Using the 9-j recoupling transformation:

$$\left\{ \left[\psi_{1\ldots f_n-2}(j^{f_n-2} v_n J_n)\; \psi_{f_n-1,\, f_n}(j^2 I) \right]^{J_n'} \left[\psi_{1\ldots f_p-1}(j^{f_p-1} v_p J_p)\; \psi_{f_p}(j) \right]^{J_p'} \right\}^{J_B}_{M_B}$$

$$= \sum_{J_A J} ((J_n I)_{J_n'} (J_p j)_{J_p'} \mid (J_n J_p)_{J_A} (I j)_J)_{J_B}$$

$$\times \left\{ \left[\psi_{1\ldots f_n-2}(j^{f_n-2} v_n J_n)\, \psi_{1\ldots f_p-1}(j^{f_p-1} v_p J_p) \right]^{J_A} \left[\psi_{f_n-1,\, f_n}(j^2 I)\; \psi_{f_p}(j) \right]^{J} \right\}^{J_B}_{M_B} \tag{5.17}$$

and expansions (5.15) and (5.16), we can write the final wave function in the form:

$$\psi^{J_B}_{M_B} = \sum_{\substack{v_n J_n, v_n' J_n' \\ v_p J_p, v_p' J_p' \\ I,\, J,\, J_A}} D_A(J_A; v_n J_n, v_p J_p)\, D_B(J_B; v_n' J_n', v_p' J_p')\, (j^{f_n-2} v_n J_n;\, j^2 I \} j^{f_n} v_n' J_n')$$

$$\times (j^{f_p-1} v_p J_p;\, j \} j^{f_p} v_p' J_p') ((J_n I)_{J_n'} (J_p j)_{J_p'} \mid (J_n J_p)_{J_A} (I j)_J)_{J_B}$$

$$\left\{ \psi^{J_A} \left[\psi_{f_n-1,\, f_n}(j^2 I)\; \psi_{f_p}(j) \right]^{J} \right\}^{J_B}_{M_B} \tag{5.18}$$

By comparison with (5.3) we obtain:

$$(J_A\, j([j_n j_n]^I j_p)^J\, |\}\, x J_B)$$

$$= \sum_{\substack{v_n J_n, v_n' J_n' \\ v_p J_p, v_p' J_p'}} D_A(J_A; v_n J_n, v_p J_p)\, D_B(x J_B; v_n' J_n', v_p' J_p')\, (j^{f_n-2}\, v_n J_n\, j^2\, I\, |\}\, j^{f_n}\, v_n' J_n')$$

$$\times (j^{f_p-1}\, v_p J_p\, j\, |\}\, j^{f_p}\, v_p' J_p')((J_n I)_{J_n'} (J_p j)_{J_p'} \,|\, (J_n J_p)_{J_A} (I j)_J)_{J_B} \qquad (5.19)$$

We obtain the spectroscopic factor by substitution of (5.19) in (5.8).

Shell Model Wave Functions

The coefficients D_A and D_B have been evaluated for pure $(f_{7/2})^n$ configurations by MBZ, (M1), who assumed that the interaction between two nucleons in the $f_{7/2}$ shell is determined by the levels in Sc^{42} which has one neutron and one proton in the $f_{7/2}$ shell. They calculated the matrix of the interaction using a representation composed of states of the form:

$$\left[\psi_{1\ldots f_n}(j^{f_n} v_n J_n)\ \psi_{1\ldots f_p}(j^{f_p} v_p J_p) \right]^J_M$$

The components of the eigenvectors of the interaction matrix gave the coefficients $D(xJ;v_nJ_n,v_pJ_p)$ for the nucleus under consideration. MBZ determined these coefficients and excitation energies for levels in nuclei with Z and N between 20 and 28.

W.J. Kossler has calculated the spectroscopic factors (given by equations 5.8 and 5.19) for the (α,p) reaction to MBZ levels in Sc^{43}, Sc^{45}, Sc^{47} and V^{51}(K1). The results are given in the next chapter with the experimental spectra.

Seniority Wave Functions

Relative cross-sections for (p,α) ground state transitions in the $f_{7/2}$ shell have been satisfactorily accounted for using good

seniority wave functions (B5, S4). All of the target and final nuclei considered here have an even number of neutrons, and so the ground states will be considered to have $v_n = 0$. Also, since all the target nuclei have even Z it will be assumed that $v_p = 0$ for the target nuclei and $v_p = 1$ for the ground states of the final nuclei.

Excited states in the final nuclei will involve higher neutron and proton seniorities. However, since in the stripping model of the (α,p) reaction (Section 5.1) it was assumed that the interaction involves only the four nucleons in the alpha particle, transitions to states of $v_n>2$ or $v_p>1$ are forbidden. Thus we have seniority selection rules:

$$\Delta v_n = 0, 2 \qquad \text{and} \qquad \Delta v_p = 1$$

It will be shown in the next chapter (see $Ti^{48}(\alpha,p)V^{51}$ data) that the proton seniority selection rule is quite good, since transitions to the first few excited states in V^{51} (for which $v_p = 3$) are very weak. The transitions that do occur can be attributed to a small admixture of $v_p = 2$ in the Ti^{48} ground state.

With the assumption of good separate neutron and proton seniority, equation 5.19 becomes very simple, since there is only one term on the right-hand side for each final state. For the target nuclei, J_A, v_n, J_n, v_p, J_p are all zero, and $D_A = 1$. For the final states with $v_n' = 0$, $J_n' = 0$, $v_p' = 1$, $J_B = J_p = j_p$ and $D_B = 1$. Also, $I = 0$ and $J = j_p$ for the transferred particles. Thus equation 5.19 becomes:

$$(J_A=0;([j_n j_n]^0 j_p)^{j_p} \} J_B=j_p) = (j_n^{f_n-2}\, 0\,0;\, j_n^2\, 0 \} j_n^{f_n}\, 0\,0)(j_p^{f_p-1}\, 0\,0;\, j_p \} j_p^{f_p}\, 1\,0) \qquad (5.20)$$

The 9-j symbol is unity for this case. The above cfp are: (T2)

$$(j_n^{f_n-2}\, 0\,0;\, j^2\, 0 \} j_n^{f_n}\, 0\,0) = \left[\frac{2j_n+3-f_n}{(f_n-1)(2j_n+1)}\right]^{1/2}$$

$$(j_p^{f_p-1}\, 0\,0;\, j_p \} j_p^{f_p}\, 1\,0) = \left[\frac{2j_p+2-f_p}{f_p(2j_p+1)}\right]^{1/2}$$

Substituting these in (5.20) and the result into (5.8) we obtain the spectroscopic factor:

$$S^{o}_{j_p j_p} = \frac{2 f_n (2j_n + 3 - f_n)(2j_p + 2 - f_p)}{(2j_n+1)^2 (2j_p+1)} \qquad (5.21)$$

The spectroscopic factors calculated using this formula will be compared with the experimental ground state relative cross-sections in the next chapter.

5.4 Coherence in the (α,p) Reaction

As mentioned in the last section, Bayman has shown how the coherence in I of the spectroscopic factor causes the $Sc^{45}(p,\alpha)Ca^{42}$ reaction to be sensitive to the relative phases of the components of the Sc^{45} wave function (B4). Bayman indicated that the Sc^{45} ground state seems to be well described by the MBZ wave function, the most important terms of which are:

$$\psi^{7/2}_{M}(Sc^{45}_{gs}) \approx 0.821\left[\psi_n(7/2^{+}00)\,\psi_p(7/2)\right]^{7/2}_{M} + 0.543\left[\psi_n(7/2^{+}22)\psi_p(7/2)\right]^{7/2}_{M} \qquad (5.22)$$

The coefficients of the other terms are all less than 0.15. This wave function is reasonably consistent with the single particle transfer reaction $Sc^{45}(d,He^3)\,Ca^{44}$ which tests only the squares of the coefficients. The (p,α) reaction, being coherent in these amplitudes, tests the relative signs and seems to favor the relative plus sign.

With the wave function (5.22) we can calculate the $Ca^{42}(\alpha,p)Sc^{45}$ ground state spectroscopic factor from (5.19) and (5.8):

$$S(Sc^{45}) = 12x2x8\ [+0.821(.0625) + 0.543(.0192)]^2$$
$$= 192(.0514 + .0104)^2 = 0.73$$

Now consider the $Ca^{40}(\alpha,p)Sc^{43}$ ground state transition. The largest terms in the MBZ wave function for Sc^{43} are:

$$\psi^{7/2}_{M}(Sc^{43}_{gs}) \approx -0.761\left[\psi_n(7/2^2 0)\,\psi_p(7/2)\right]^{7/2}_{M} - 0.609\left[\psi_n(7/2^2 2)\,\psi_p(7/2)\right]^{7/2}_{M} \quad (5.23)$$

The coefficients of the other terms are less than 0.21. Using this wave function, the (α,p) spectroscopic factor is:

$$S(Sc^{43}) = 2x2x8\ [-0.761(.125) - 0.609(.0665)]^2$$
$$= 32(-.0951 - .0405)^2 = 0.59$$

If the relative signs of the first two terms in the Sc^{43} wave function were reversed (i.e. amplitudes -0.761 and +0.609) the $Ca^{40}(\alpha,p)Sc^{43}$ ground state spectroscopic factor becomes:

$$S'(Sc^{43}) = 32(-.0951 + .0405)^2 = 0.096$$

Thus, the ratio $S(Sc^{45})/S(Sc^{43})$ is 1.24 for the relative plus sign between the Sc^{43} amplitudes and 7.6 for the relative minus sign. Since the targets have spin zero, only one angular momentum transfer is allowed, and so the spectroscopic factors affect the magnitudes of the cross-sections, but not the shapes. It will be seen in the next chapter that the data favors the relative plus sign.

It must be emphasized here that the magnitudes of the MBZ amplitudes in the Sc^{43} wave function were assumed to be correct without supporting data such as the (d,He^3) data for Sc^{45}. If the magnitudes of the amplitudes are uncertain then the determination of phases by the (α,p) reaction is, at best, uncertain. In general, the (α,p) cross-section depends on the wave functions in a complicated way, making it impossible to obtain unique values for the various amplitudes from the

(α,p) reaction data alone. If, however, the magnitudes of the amplitudes are known from other data (e.g. single particle transfer reactions which, being incoherent in the amplitudes, are easier to interpret) then the (α,p) reaction can be helpful in determining the relative phases.

Another type of coherence arises when more than one neutron (or proton) shell contributes significantly to the (α,p) reaction. When the final states are low lying levels in nuclei with N and Z between 20 and 28, contributions from shells above the well-separated f 7/2 shell are expected to be small, and so the (α,p) model described in this chapter should be applicable.

For the reaction $Ca^{48}(\alpha,p)Sc^{51}$, however, the target consists of a filled 1 f 7/2 neutron shell and so the transferred neutrons must go into a higher shell. Figure 5.4 shows the relevant shell model levels for this region. The 2p 3/2, 1f 5/2 and 2p 1/2 shells are not well isolated. (p,d) reactions in this region have indicated a strong mixing of 1f 5/2 and 2p neutrons in the ground states of nuclei containing 29 to 32 neutrons (L3). Thus, the ground state of Sc^{51} may be expected to consist of a mixture of f 5/2 and 2p neutrons. With more than one neutron shell contributing to the (α,p) reaction, the cross-section cannot be factored into the spectroscopic factor and the reduced cross-section as it was in Section 5.1 (equation 5.7). Instead, we get a coherent sum of terms corresponding to the different neutron shells:

$$\frac{d\sigma}{d\Omega} \propto \sum_{Mmp} \left| \sum_{jn} A_{jn} \beta_{jn}(\theta) \right|^2 \qquad (5.24)$$

Here A_{jn} is the amplitude for the reaction with the neutrons going

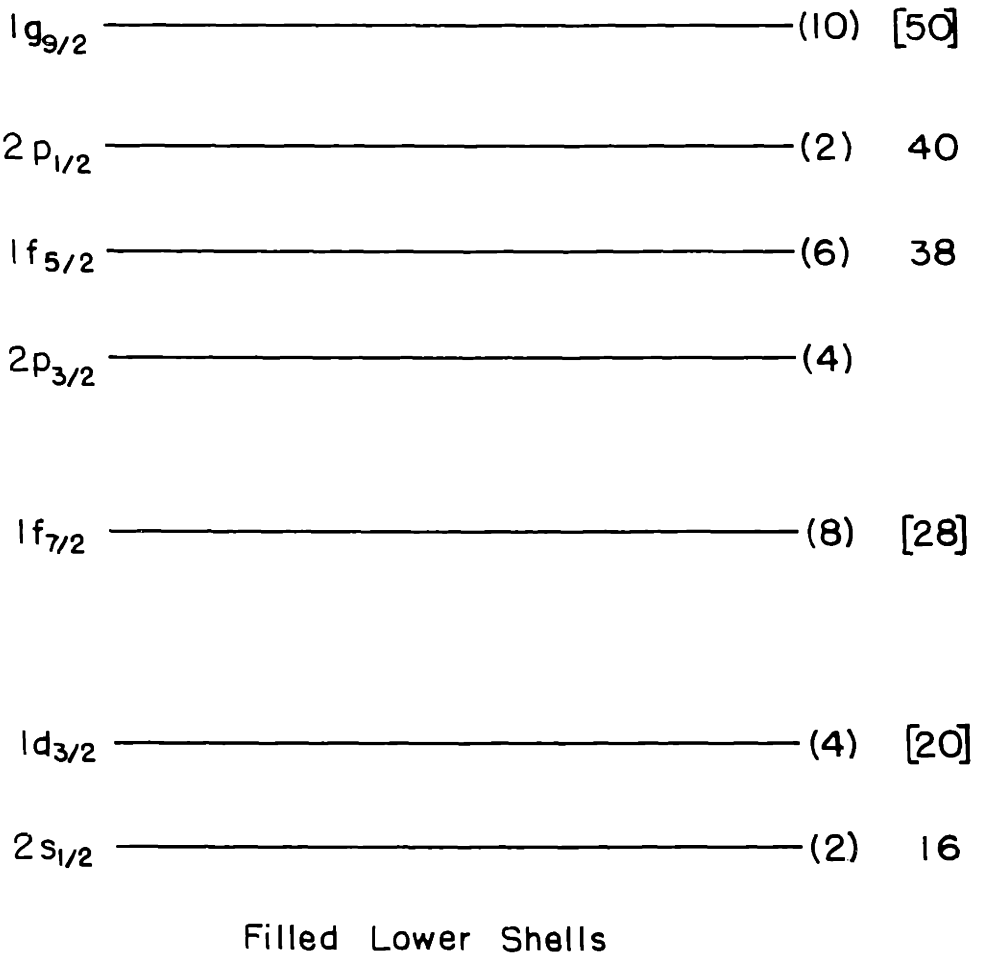

Figure 5.4 Shell Model Levels near the $1f_{7/2}$ Shell

into the shell j_n:

$$A_{j_n} \propto \sum_I (J_A j (\lbrace j_n j_n \rbrace^I j_p)^J | \rbrace J_B)(J j_p \tfrac{1}{2} -\tfrac{1}{2} | I 0)(j_n j_n \tfrac{1}{2} -\tfrac{1}{2} | I 0)(2I+1)^{-\frac{1}{2}} \quad (5.25)$$

and $\beta_{j_n}(\theta)$ is the same as in Section 5.1 (equation 5.12) with the form factor (equation 5.13) evaluated for the appropriate neutron shell.

Thus, the different neutron configurations can affect both the magnitude and the shape of the cross-section. The effects cannot be evaluated quantitatively since a modification of the DWBA code would be necessary. A qualitative discussion of the effect will be given in the next chapter with reference to the $Ca^{48}(\alpha,p)Sc^{51}$ data.

CHAPTER 6

EXPERIMENTAL RESULTS AND COMPARISON WITH THEORY

In this chapter, the experimental (α,p) spectra and differential cross-sections are presented and compared to each other and to theory. In the discussion of the ground state transitions, the case of the $Ca^{48}(\alpha,p)Sc^{51}$ reaction is discussed separately since the target has a closed $f_{7/2}$ neutron shell. The other four targets, in order of increasing mass, have 0,2,4, and 6 neutrons in the $f_{7/2}$ shell, and thus the two neutrons, transferred in the (α,p) reaction on these targets, can go into the $f_{7/2}$ shell. These cases are discussed under the heading "$f_{7/2}$ shell".

The (α,p) transitions to excited states are discussed separately for each nucleus studied. Each experimental spectrum is compared with other results for the same nucleus, and with levels calculated (for the $f_{7/2}$ nuclei) by MBZ.

Finally, in the next chapter, the general conclusions concerning the (α,p) reaction and the nuclei studied are summarized.

6.1 DWBA Calculations

The formalism for the calculation of the (α,p) stripping cross-section was presented in Section 5.1. As mentioned there, the cross-sections were evaluated using the DWBA code JULIE. In Section 5.1 the form factors used in the (α,p) calculations were discussed.

This section contains discussions of the choice of optical potentials for the incident alpha particle and the outgoing proton, and the use of a radial cutoff in the DWBA calculations.

Alpha and Proton Optical Potentials

The optical potentials required for the calculation of the incoming and outgoing distorted waves were obtained from optical model fits to elastic alpha and proton scattering from nuclei in the mass 40 region.

The alpha particle parameters were obtained from the results of fits to elastic scattering from the Ca and Ti isotopes (L2). The data was taken at the M.I.T. cyclotron and thus the incident alpha energy was the same as that used for the (α,p) data. Many sets of alpha parameters were determined including, for Ti^{48}, several different sets which gave equivalent fits to the data. Such ambiguities in the optical parameters for strongly absorbed particles have been investigated (D1,B6) and at present there is no criterion for determining which set of parameters is preferred. Therefore, the $Ti^{48}(\alpha,p)V^{51}$ ground state cross-section was calculated using several optical potentials (each of which gave a good fit to the Ti^{48} elastic alpha scattering) with real well depths, V, from 47.6 to 213 Mev. It was found that the shape of the (α,p) cross-section was about the same for each set of parameters used, but the magnitude using the V = 47.6 Mev set was roughly twice that obtained using the V = 213 Mev set.

Using sets of optical parameters with approximately the same V, but determined from the elastic scattering from different Ca and Ti isotopes, gave about the same (α,p) results for both shape and magnitude.

Therefore, the same alpha optical potential was used for all of the (α,p) calculations presented here. Table 6.1 gives the form of the potentials and the values of the parameters used for both the alpha particle and the proton potentials. The proton parameters, taken from reference L4, were obtained from an analysis of proton scattering from Ar^{40}. These proton parameters differ only slightly from those of Perey (P1), and the differences were found to have very little effect on the (α,p) calculations.

Radial Cutoff

In many DWBA calculations an arbitrary lower limit is placed on the radial integrals (see equation 5.12). The use of such a cutoff radius for (d,p) calculations has been discussed by Lee et al. (L4) who point out that a radial cutoff affects the calculated cross-sections in somewhat the same way as the use of nonlocal optical potentials and finite range effects. For the $Ca^{40}(d,p)Ca^{41}$ reaction, Lee et al. conclude that the use of a radial cutoff cannot produce a consistent set of spectroscopic factors, but its use does improve some features of the calculated angular distributions.

In their paper on the J-dependence of the (α,p) reaction (L5), Lee et al. mentioned that the oscillatory structure of the $2p\frac{1}{2}$ transition was only produced with a radial cutoff on the matrix element in their (α,p) calculations for 18 Mev alpha particles. The (α,p) J-dependence will be discussed later (Section 6.3). However, it should be pointed out here that pronounced oscillatory structure for $J\pi = \frac{1}{2}$-(α,p) transitions appeared in the present calculations without the use of a cutoff.

For the (α,p) calculations presented here, no radial cutoffs were used. In any case, the calculations for the $(1f_{7/2})^3$ configuration are

Optical Potentials

$$U(r) = U_c(r) - V(e^x + 1)^{-1} - i\left[W - 4W_D\,(d/dx')\right]\,(e^{+x'} + 1)^{-1}$$
$$+ (\hbar/m_\pi c)^2\, V_s(\vec{L}\cdot\vec{\sigma})\frac{1}{r}(d/dr)(e^x + 1)^{-1}$$

$$x = \left(\frac{r - r_o\, A^{1/3}}{a}\right) \qquad x' = \left(\frac{r - r_o'\, A^{1/3}}{a'}\right)$$

U_c is the Coulomb potential from a uniform charge of radius $r_c\, A^{1/3}$fm.

PARAMETERS

Parameter	Alpha	Proton
V (Mev)	47.6	48.0
W (Mev)	13.8	0
r_o (fm)	1.585	1.20
r_c (fm)	1.585	1.25
a (fm)	.549	0.65
W_D (Mev)	0	11.0
r_o' (fm)	1.585	1.25
a' (fm)	.549	0.47
V_s (Mev)		8.0

Table 6.1

Alpha and Proton Optical Potentials

rather insensitive to a cutoff since the form factors are very small inside the nucleus (see Figures 5.2 and 5.3). Also, the similarity of the L = 1 curves in Figure 5.3 suggests that the $(1f_{7/2})^2$ 2p cross-sections would not be greatly affected by a radial cutoff. On the other hand, the $(2p)^2 1f$ form factor (Figure 5.2) is very large inside the nucleus ($r \leq 3.5$ fm), and so a radial cutoff could have a significant effect. Thus the $Ca^{48}(\alpha,p)Sc^{51}$ ground state DWBA calculation (see Section 6.2.3) may be affected by a radial cutoff.

6.2 Results for (α,p) Ground State Transitions

Figure 6.1 shows the experimental ground state differential cross-sections together with the DWBA calculations for the five targets studied in this experiment. Each calculated curve has been arbitrarily normalized to produce the best fit to the corresponding data points. The relative magnitudes of these fits compared to the DWBA calculations yield experimental spectroscopic factors which will be discussed in Section 6.2.2.

6.2.1 Ground State Angular Distributions - f7/2 Shell

The most striking feature of the ground state data (Figure 6.1) is the similarity of the shapes of the five ground state angular distributions. All the targets are even-even (spin and parity 0+) and all of the final ground states except Sc^{51} are known to have spin and parity $7/2^-$ and thus the transitions to these states all involve angular momentum transfers of L = 3 and J = 7/2. Also, on the basis of the shell model, the ground state of Sc^{51} is expected to be $7/2^-$. Thus, similarities between the ground

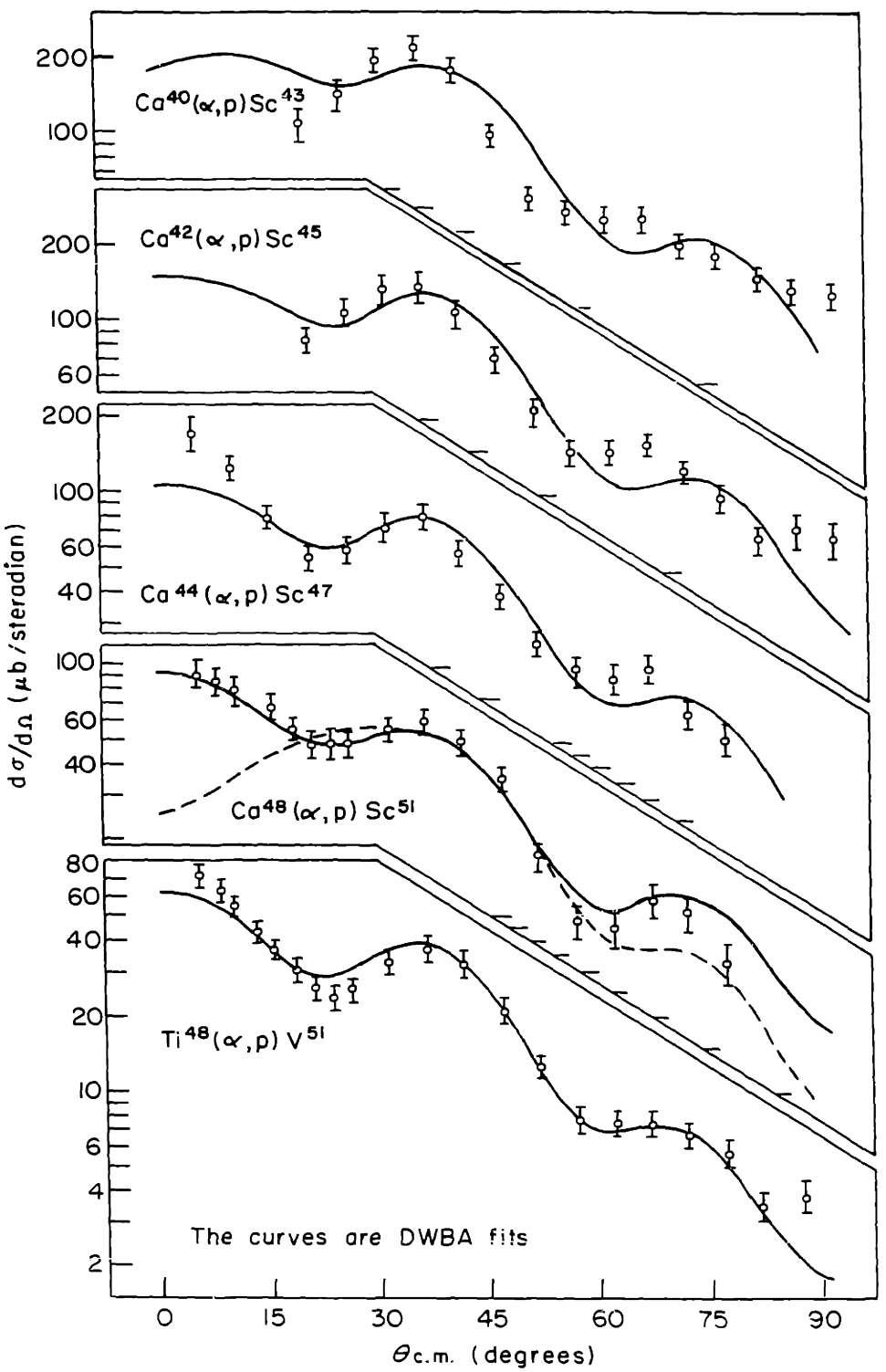

Figure 6.1 (α,p) Ground State Differential Cross Sections (note different scales)

state angular distributions are not surprising. However, there are several effects which could cause differences in the shapes, and the experimental similarity will be interpreted as evidence that these effects are insignificant here (within the limits imposed by experimental and theoretical uncertainties).

These effects are: 1) Compound Nuclear Reactions. Contributions from (α,p) reactions proceeding through the formation of a compound nucleus would be expected to exhibit angular distributions that are much less forward peaked than the observed ground state angular distributions. In addition, such contributions would be expected to show relatively large fluctuations in magnitude (and perhaps shape) over the range of nuclei studied, since, besides the variation in A and Z, the (α,p) ground state Q values varied from -1.17 Mev for Ti^{48} to -5.86 Mev for Ca^{48}. Thus, since significant compound nuclear contributions would probably cause differences in the shapes of the (α,p) differential cross-sections for different targets, it is assumed that these (α,p) transitions proceed predominantly by direct reactions.

2) Excitation of the $d_{3/2}$ Hole State in Sc^{45}. Low lying $d_{3/2}$ hole states (formed by promoting a $d_{3/2}$ proton to the $f_{7/2}$ shell) have been found in Sc^{43}, Sc^{45} and Sc^{47} (Y1, Y2, B7, H2). In Sc^{43} the $d_{3/2}$ hole state occurs at an excitation energy of 150 kev and so would show up in the proton energy spectrum if significantly populated by the (α,p) reaction (see Section 6.3). In Sc^{47} the $d_{3/2}$ hole state is at 760 kev and thus is clearly resolved from the ground state (but not from the 800 kev state, see Section 6.3). In Sc^{45}, however, the $d_{3/2}$ hole state occurs only 13 kev above the ground state and therefore, since the energy resolution was about

150 kev, the experimental $Ca^{42}(\alpha,p)Sc^{45}$ ground state cross-section will include any transitions to this low lying 3/2 + state.

The shape of the angular distribution of the (α,p) reaction to the 3/2 + state is expected to be very similar to that for the $Ca^{44}(p,\alpha)K^{41}$ ground state (3/2+) transition shown in Figure 6.2. The (p,α) data, at an incident proton energy of 26.5 Mev, was taken by A. Bernstein, M. Rickey and S. Smith (S5). The lines in Figure 6.2 are drawn through the data points for visual purposes only, and the normalization of each curve is arbitrary. The two upper curves (both for L = 3, J = 7/2) show that the (α,p) and (p,α) experimental angular distributions are very similar for the same angular momentum transfers. Thus, the $Ca^{42}(\alpha,p)Sc^{45*}(3/2+)$ angular distribution would probably be quite similar in shape to the lower curve in Figure 6.2.

Therefore, if the (α,p) reaction to Sc^{45} populates the 13 kev state significantly compared to the ground state, then the position of the peak near 35 degrees in the $Ca^{42}(\alpha,p)Sc^{45}$ ground state angular distribution would be shifted toward smaller angles compared to that for the $Ca^{44}(\alpha,p)Sc^{47}$ case for which the final state is pure $7/2^-$. Such a shift was seen in the angular distribution for the pickup reaction $Ti^{46}(d,He^3)Sc^{45}$ by Yntema and Satchler (Y1) who inferred the existence of the d3/2 hole state from the position (and magnitude) of the peak.

However, a comparison between the $Ca^{42}(\alpha,p)Sc^{45}$ ground state angular distribution and that for the $Ca^{44}(\alpha,p)Sc^{47}$ reaction (Figure 6.1) reveals no significant contribution from the $d_{3/2}$ hole state in Sc^{45}. The (α,p) transitions to the hole states in Sc^{43} and Sc^{47} are also very weak compared to the ground state transitions (see Section 6.3).

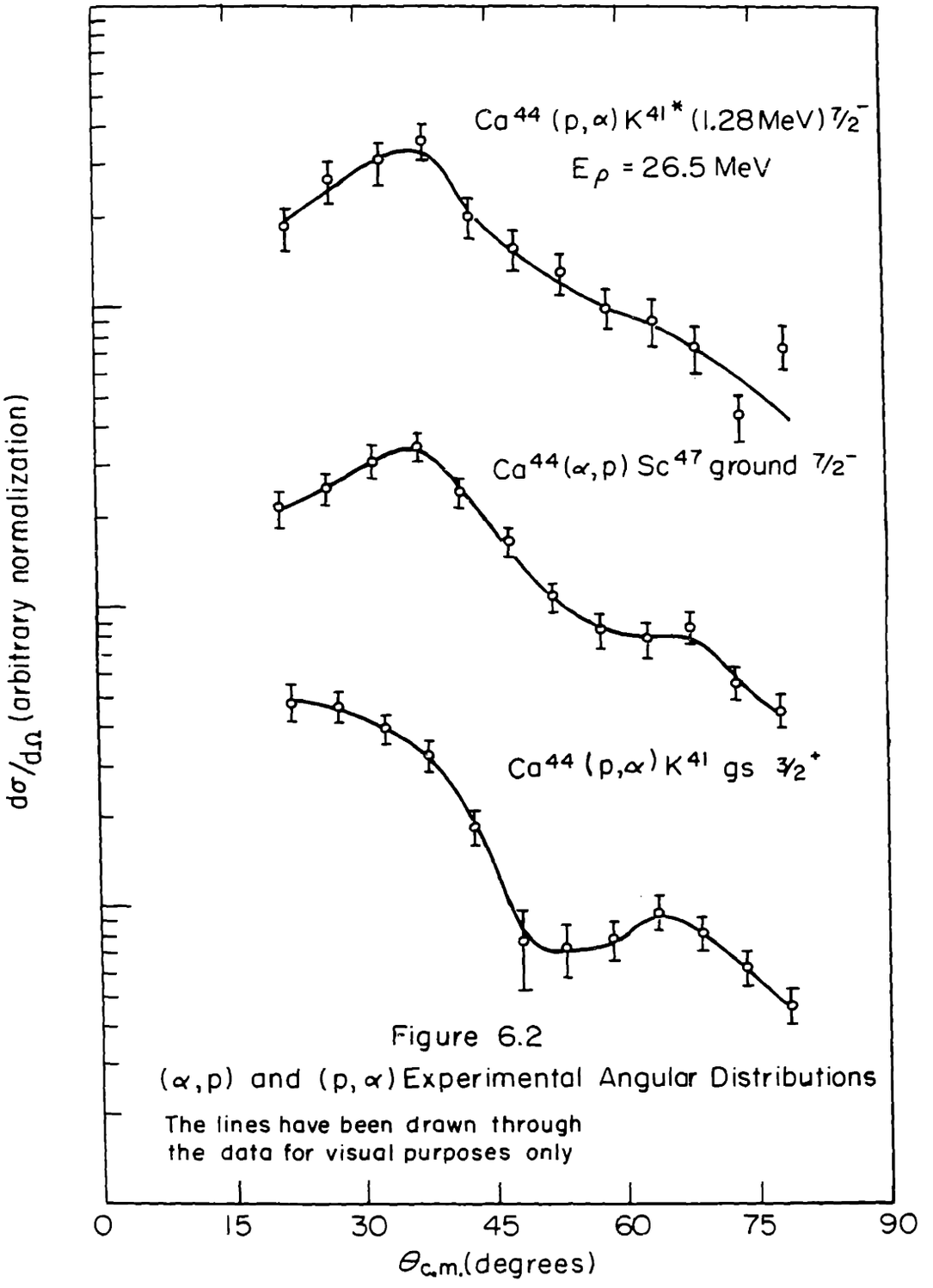

Figure 6.2

(α,p) and (p,α) Experimental Angular Distributions

The lines have been drawn through the data for visual purposes only

Weak excitation of these hole states is consistent with the stripping model of the (α,p) reaction. If the (α,p) reaction goes only by stripping of the incident alpha particle, then the hole states are populated only via the appropriate particle-hole admixture in the ground state of the target nucleus. Such admixtures are sufficiently small for the Ca isotopes so that weak excitation of these hole states is expected.

If, however, the (α,p) reaction goes by knockout of a proton from the target and the subsequent capture of the incident alpha particle, then there is no a priori reason why the hole states cannot be strongly excited. Thus, it appears that in the (α,p) reactions discussed here, the dominant reaction mechanism is stripping.

3) Contributions from Different Neutron Shells. For the ground state (α,p) transitions from all of the targets except Ca^{48}, the transferred neutrons as well as the proton were assumed to go into the $1f_{7/2}$ shell. However, the nuclear states involved may contain admixtures of other configurations and thus the (α,p) cross-sections may have contributions from other shells. The most probable admixture might be the case where the proton goes into the $1f_{7/2}$ shell and the neutrons, coupled to angular momentum $I = 0$, go into the $2p_{3/2}$, $1f_{5/2}$ or $2p_{\frac{1}{2}}$ shells.

As mentioned at the end of Chapter 5, contributions to the (α,p) reaction from different neutron shells are coherent and therefore can, in principle, affect both the shape and magnitude of the cross-section (see Section 5.4). Experimentally, however, the angular distribution for the $Ca^{48}(\alpha,p)Sc^{51}$ ground state transition, for which the neutrons cannot go into the $1f_{7/2}$ shell, is very similar to the angular distributions for the transitions involving mostly $(1f_{7/2})^2$ neutron transfer (see Figure 6.1).

Therefore, no information about the neutron configurations can be obtained from the shapes of the angular distributions. This point will be discussed more fully later (Section 6.2.4) in connection with the $Ca^{48}(\alpha,p)Sc^{51}$ reaction.

6.2.2 Ground State Spectroscopic Factors - $f_{7/2}$ Shell

The experimental spectroscopic factors obtained from the DWBA fits shown in Figure 6.1 are presented in Table 6.2 along with the calculated spectroscopic factors. All the values given for the cross-sections (columns 1-4) are taken at a center of mass angle of about 36.5 degrees. The first column in Table 6.2 gives the experimental magnitude of each (α,p) cross-section, and column two gives this magnitude relative to $Ti^{48}(\alpha,p)V^{51}$. The magnitude of the calculated DWBA cross-section (relative to Ti^{48}) is given in column three and this cross-section normalized by fitting the calculated curve to the appropriate data points (see Figure 6.1) is given in column four. The ratio of σfit (column four) to σDWBA (column three) gives the experimental spectroscopic factor which is given, relative to Ti^{48}, in column five.

The theoretical spectroscopic factors, also relative to Ti^{48}, are given in columns six and seven. Column six gives the spectroscopic factor calculated assuming good separate neutron and proton seniority (equation 5.21) and column seven lists the value obtained using the MBZ shell model wave functions (equations 5.8 and 5.19 with the MBZ wave function coefficients, D_A and D_B).

The agreement between theory and experiment is very good for Ca^{42}

Reaction	(1) σ_{EXP}	(2) σ_{EXP}*	(3) σ_{DWBA}*	(4) σ_{FIT}	(5) S_{EXP}*	(6) S_{Theory}* (Senority)	(7) S_{Theory}* (MBZ)
$Ca^{40}(\alpha,p)Sc^{43}$	220	6.03	1.56	180	2.96	1.33	1.90
$Ca^{42}(\alpha,p)Sc^{45}$	133	3.64	1.57	128	2.08	2.00	2.07
$Ca^{44}(\alpha,p)Sc^{47}$	80.0	2.19	1.29	79	1.57	2.00	2.00
$Ti^{48}(\alpha,p)V^{51}$	36.5	1.00	1.00	39	1.00	1.00	1.00
$Ca^{48}(\alpha,p)Sc^{51}$ (1)	60.0	1.64	1.34	54	1.03	2.67	
$Ca^{48}(\alpha,p)Sc^{51}$ (2)	60.0	1.64	0.29	54	4.82	1.78	

*Relative to $Ti^{48}(\alpha,p)V^{51}$

Sc^{51} (1) Assuming $(2p_{3/2})^2$ neutron transfer

Sc^{51} (2) Assuming $(1f_{5/2})^2$ neutron transfer

All cross-sections are taken at approximately 36.5°C.M.

Table 6.2

Theoretical and Experimental Spectroscopic Factors for the (α,p) Ground State Transitions

and Ca^{44} relative to Ti^{48}. For these targets the seniority and MBZ spectroscopic factors are essentially identical. For Ca^{40} the MBZ spectroscopic factor is somewhat larger than the seniority one, and the agreement with experiment is improved by using the MBZ wave functions.

In Section 5.4 the usefulness of the coherence of the (α,p) reaction in the angular momentum of the transferred neutron pair was illustrated by a calculation of the ratio of the $Ca^{42}(\alpha,p)Sc^{45}$ and the $Ca^{40}(\alpha,p)Sc^{43}$ ground state spectroscopic factors. Using simplified MBZ wave functions, it was shown that the predicted ratio was 1.24 for a relative plus sign between the first two terms of the Sc^{43} wave function, and 7.6 for a relative minus sign. The experimental value of 0.70 favors the relative plus sign (in agreement with MBZ) however, the agreement with the theoretical value of 1.09 (using the complete MBZ wave functions) shows that the present wave functions and/or (α,p) theory are inadequate to explain completely the experimental results.

The results presented in Figure 6.1 and Table 6.2 show that, for the ground state transitions, the overall agreement between the present theory and experiment is rather good for the $f_{7/2}$ shell nuclei. Similar satisfactory agreement was obtained by Sherr et al. (S4) for (p,α) reactions in the $f_{7/2}$ shell at 18 Mev using essentially the same model as was used here.

6.2.3 The $Ca^{48}(\alpha,p)Sc^{51}$ Ground State Transition

The $Ca^{48}(\alpha,p)Sc^{51}$ reaction differs from those described above in that the transferred neutrons cannot go into the $1f_{7/2}$ shell. The shell model level immediately above $1f_{7/2}$ is $2p_{3/2}$, but, as mentioned at the end of Chapter 5, the Sc^{51} ground state may contain a mixture of 2p and $1f_{5/2}$ neutrons.

The calculated curves are compared to the experimental $Ca^{48}(\alpha,p)Sc^{51}$ ground state differential cross-section in Figure 6.1. The dashed curve is for 2p neutron transfer, and the solid curve is for 1f neutron transfer only, the proton going into the $1f_{7/2}$ shell in both cases. The values of j_n have been omitted here since the shape of the form factor (equations 5.13 and 5.6), and therefore also the shape of the calculated angular distribution, depends on the transferred nucleon quantum numbers n and l but not j (for unique neutron and proton shells). The magnitudes of the calculated cross-sections, and therefore also the experimental spectroscopic factors, are dependent on j_n and j_p. The calculation for mixed neutron configurations was not done since it would require modification of the DWBA code (see Section 5.4).

The two $Ca^{48}(\alpha,p)Sc^{51}$ curves in Figure 6.1 have both been normalized to fit the data and the relative magnitudes of the curves are indicated by S_{EXP} (column five) in Table 6.2. Using the good seniority spectroscopic factors we see that, compared to experiment, the theoretical prediction is a factor of 2.6 too large assuming $2p_{3/2}$ neutron transfer and a factor of 2.7 too small assuming that the neutrons go into the $1f_{5/2}$ shell. The large difference (a factor of 7) is mostly due to the enhancement of the calculated DWBA cross-section for the $2p_{3/2}$ neutron case (Table 6.2, column three). The form factor for 2p neutrons peaks at a larger radius than that for 1f neutrons (Figure 5.2), and this apparently causes the enhancement. A similar increase occurs in the magnitude of the cross-section for inelastic alpha particle scattering as the peak of the form factor is moved to larger radii (B8).

Agreement between the theoretical and experimental spectroscopic factors for the $Ca^{48}(\alpha,p)Sc^{51}$ ground state reaction could presumably be pro-

duced by some mixture of 2p and $1f_{5/2}$ neutrons. However, it is difficult to see how the angular distribution, calculated with a reasonable fraction of $2p_{3/2}$ neutrons, could fit the data since the calculation favors the $2p_{3/2}$ neutron case (for which the angular distribution falls off at small angles) by roughly a factor of 7.

Besides the effect of the coherence between the 2p and 1f neutrons there are two additional uncertainties which could influence the fit to the Ca^{48} data. The first, which has already been mentioned in Section 6.1 is the possible sensitivity of the 2p neutron calculation to a radial cutoff.

The second possibility is that more than one state in Sc^{51} is contributing to the observed cross-section. No evidence was seen for any states below 0.86 Mev, but due to the energy resolution of about 150 kev, states very near the ground state would not be resolved. Also, at small angles (less than 15°) the resolution was much worse (about 300-400 kev FWHM) due to the Au absorber used to stop the scattered alpha particles. Erskine et al. (E2) who also studied the $Ca^{48}(\alpha,p)Sc^{51}$ reaction, presumably with better resolution, reported no states in Sc^{51} below 0.86 Mev. Also, it seems unlikely that the sum of the (α,p) cross-sections to the ground state and a low lying excited state would have an angular distribution very similar to the other 0+ to 7/2- transitions observed. Thus, this last possibility is considered remote and further modifications of the theory are necessary in order to account satisfactorily for the $Ca^{48}(\alpha,p)Sc^{51}$ reaction.

6.2.4 Ground State Q Values

The (α,p) ground state Q values were measured relative to that for the $C^{12}(\alpha,p)N^{15}$ reaction which was taken to be -4.965 Mev. (T1). The energy scale was determined from the Mylar (α,p) spectrum (see Figure 4.8 and Section 4.4) corrected for energy losses in the Mylar target. Using this scale, the energy of each ground state proton peak was determined. These energies and the appropriate (α,p) kinematic calculations (including energy losses in the targets) yielded the measured Q values given in Table 6.3. Also shown are previously measuredvalues and the values calculated from the 1964 mass table (M3).

Target	Present Measurement	Previous Measurement	1964 Mass Table
Ca^{40}	$-3.48 \pm .1$	-3.470	-3.537
Ca^{42}	$-2.36 \pm .1$	-2.343	-2.343
Ca^{44}	$-1.80 \pm .2$		-1.998
Ca^{48}	$-5.83 \pm .1$	-5.860	
Ti^{48}	$-1.16 \pm .1$	-1.162	-1.158

All Q values are in Mev

Previous measurements are from reference T1 except Ca^{48} whichis from E1.

Table 6.3

(α,p) Ground State Q Values

6.3 Results for the (α,p) Reaction to Excited States

The use of the (α,p) reaction to identify characteristics of excited states of the final nuclei was limited by several factors. First, the (α,p) energy resolution (about 150 kev FWHM) was a limitation since closely spaced levels could not be resolved. This was especially noticeable above an excitation energy of about 2 to 3 Mev where the levels were closely spaced and many were excited by the (α,p) reaction.

A second limitation was a lack of calibrations for the calculated differential cross-sections. That is, for the energy and mass region studied here, very few experimental (α,p) or (p,α) angular distributions to known spin and parity states have been observed. Exceptions to this are the 7/2- ground state transitions discussed in Section 6.2. Also, qualitative agreement between theory and experiment for 3/2- and $\frac{1}{2}$- (α,p) transitions at 18 Mev has been obtained (L5). Other spin assignments, based on the (α,p) differential cross-sections, must be regarded as uncertain unless there is additional evidence to support the assignments.

6.3.1 $Ti^{48}(\alpha,p)V^{51}$

The experimental proton spectrum from the $Ti^{48}(\alpha,p)V^{51}$ reaction is shown in Figure 6.3 along with a summary of the known levels in V^{51} (B9, S6) and the spectrum calculated by MBZ (M1) assuming a pure $(f_{7/2})^3$ proton configuration (the neutron shell is closed, i.e. N = 28). Opposite each proton peak is shown the present results for spin and parity (brackets indicate an uncertain assignment) and excitation energy of the corresponding state in V^{51}. The probable errors in the excitation energies are ± 30 kev

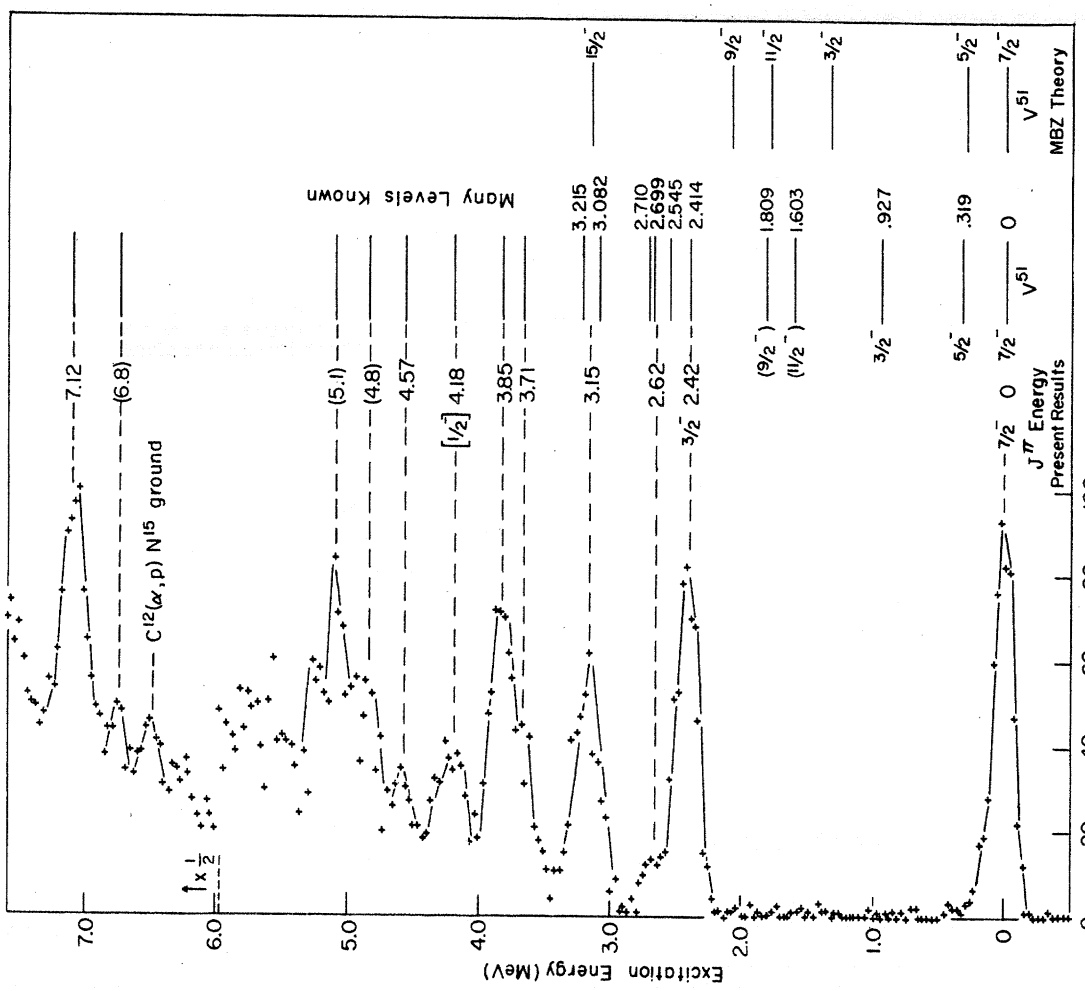

Figure 6.3 $Ti^{48}(\alpha,p)V^{51}$ Proton Spectrum at 30°_{LAB} and V^{51} Energy Levels

for the 2.42 Mev state and ± 50 kev for the rest except those in parentheses which have ± 100 kev errors.

The excellent agreement between the MBZ spectrum and the known V^{51} energy levels suggests that the levels below 2 Mev belong to the $(f_{7/2})^3$ configuration. The MBZ spectroscopic factors for the (α,p) reaction to these levels are not shown since they are all predicted to be less than 2% of the ground state spectroscopic factor. This predicted weak excitation is a direct result of the $(f_{7/2})^3$ character of these states and the model used for the (α,p) reaction. Since the final neutron shell is closed, the neutrons transferred in the (α,p) reaction must couple with the neutrons in Ti^{48} to a total neutron spin of zero. The transferred proton then couples with the two $1f_{7/2}$ protons in Ti^{48} to form the appropriate $(f_{7/2})^3$ state in V^{51}. Since the (α,p) reaction is assumed to go by stripping, the state of Ti^{48} cannot be changed by the reaction. Let us assume that the Ti^{48} ground state wave function is :

$$\psi(Ti^{48}_{gs}) = \alpha \psi[(\pi f_{7/2})^2_0 (\nu f_{7/2})^{-2}_0]_0 + \beta \psi[(\pi f_{7/2})^2_2 (\nu f_{7/2})^{-2}_2]_0 \qquad (6.1)$$

Here $(f_{7/2})^n_J$ represents the state of n $f_{7/2}$ particles coupled to spin J; π stands for protons and ν for neutrons. The MBZ wave function for Ti^{48} ground state has $\alpha = 0.91$, $\beta = 0.40$ and the amplitudes of the other components are less than 0.02.

In contrast to the $Ti^{48}(\alpha,p)V^{51}$ ground state ($J\pi = 7/2^-$) transition which can proceed via either component of the Ti^{48} wave function, the (α,p) reaction to the $(\pi f7/2)^3$ states of spin other than $7/2^-$ (which have no $(\pi f_{7/2})^2_0$ component) can only go via the second term in equation 6.1. This reduces the spectroscopic factor in two ways: 1) Since the initial state has

$J_p = J_n = 2$, the recoupling coefficient in the spectroscopic factor (Section 5.3, equation 5.19) is reduced by a factor of 5 compared to the $J_p = J_n = 0$ case. Thus, even if $\beta = 1$ in equation 6.1, the spectroscopic factor is reduced by $(5)^2 = 25$ due to angular momentum coupling. 2) In addition, the spectroscopic factor is proportional to β^2 and is thus reduced by another factor of about 6 for the wave function given by equation 6.1.

Experimentally (see Figure 6.3), the states discussed above are essentially not excited by the (α,p) reaction at this alpha energy (30.8 Mev). Based on the above discussion, the non-excitation of these states is evidence that: 1) Compound nuclear contributions to the (α,p) reaction at this energy are negligible. This is because the above arguments for weak excitation of the $(\pi f_{7/2})^3$ states apply only for a direct reaction mechanism. If the (α,p) reaction proceeds via the formation and subsequent proton decay of compound nuclear states then there is no a priori reason for the non-excitation of these states in V^{51}.

2) The fact that these states are not seen in the (α,p) reaction provides further evidence that they are well described in terms of a closed neutron shell and a $(\pi f_{7/2})^3$ proton configuration. To be specific, let us consider the 3/2- state at 0.927 Mev. The dominant configuration for this state is $[(\pi f_{7/2})^3_{3/2-} (\nu f_{7/2})^8_0]_{3/2-}$. If the neutron shell were not closed we might expect an admixture of the type:

$$\{(\pi f_{7/2})^2_0 [(\pi 2p_{3/2})(\nu 2p_{3/2})^2_0]_{3/2-} (\nu f_{7/2})^6_0\}_{3/2-}$$

Such an admixture would lead to excitation of the state by the (α,p) reaction.

In view of the closed neutron shell a more likely admixture in the wave function for this 3/2- state might be $\{[(\pi f_{7/2})^2_0 \pi 2p_{3/2}]_{3/2-} (\nu f_{7/2})^8_0\}_{3/2-}$.

A calculation using good seniority spectroscopic factors (equation 5.21) indicates that at 30 degrees LAB the cross-section for the (α,p) reaction to such a state should be about the same magnitude as that for the ground state transition. Thus it appears that the configuration of the 3/2- state is quite pure $(f_{7/2})^3$.

The above discussion gives a strong hint as to the structure of the strongly excited state at 2.42 Mev in the $Ti^{48}(\alpha,p)V^{51}$ spectrum. The angular distribution of this state is shown in Figure 6.4 along with the DWBA calculation for $(1f_{7/2})^2$ neutron transfer and $2p_{3/2}$ proton transfer. As mentioned above, the good seniority spectroscopic factors and the DWBA calculations indicate that the cross-sections for the ground state and a pure $2p_{3/2}$ proton state should be about equal at 30 degrees LAB. The good agreement between the calculated and experimental differential cross-section for both shape and magnitude indicates that the 2.42 Mev state most likely has the proton configuration $(\pi f_{7/2})^2_0$ $(\pi 2p_{3/2})$ with the neutron shell closed. This assignment agrees with that of Schwager (S6) who studied the γ rays following neutron capture by V^{50}.

The assumption that the $1f_{7/2}$ neutron shell is closed for the 2.42 Mev state in V^{51} is supported by the position of the level in Ti^{50} (which also has 28 neutrons) with the neutron configuration $[(\nu f_{7/2})^6_0 (\nu 2p_{3/2})^2_0]_{0+}$. This level, located by the $Ti^{48}(t,p)Ti^{50}$ reaction, occurs at an excitation energy of 3.88 Mev (H3). Thus the 2.42 Mev level in V^{51} seems to lie at too low an energy to have a large admixture of the configuration with the two neutrons, transfered in the $Ti^{48}(\alpha,p)V^{51}$ reaction, in the $2p_{3/2}$ shell.

The energies of single particle states in this region are shown in Figure 6.5 (This figure was obtained from reference E2). It is apparent

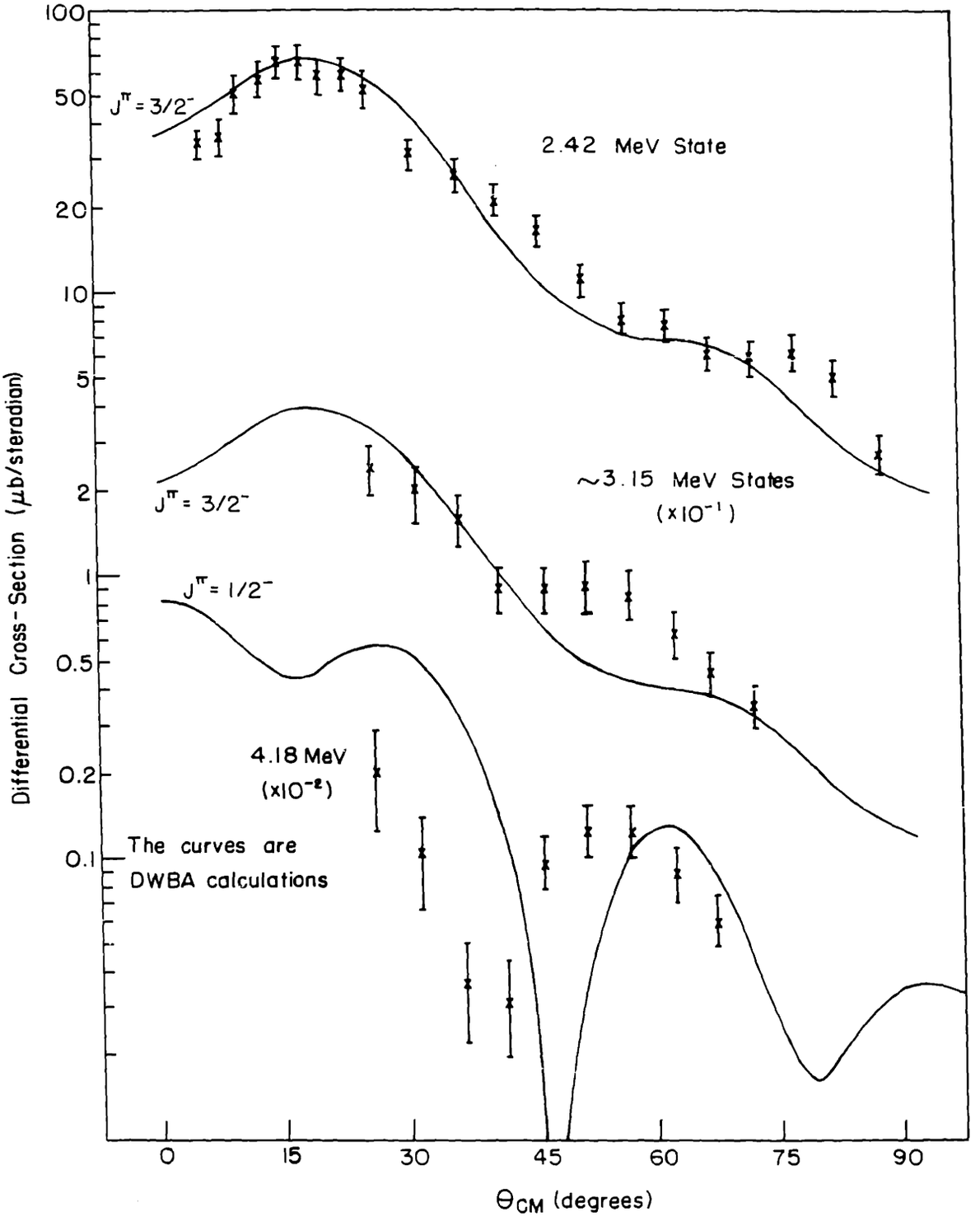

Figure 6.4 $Ti^{48}(\alpha,p)V^{51*}$ Differential Cross-Sections

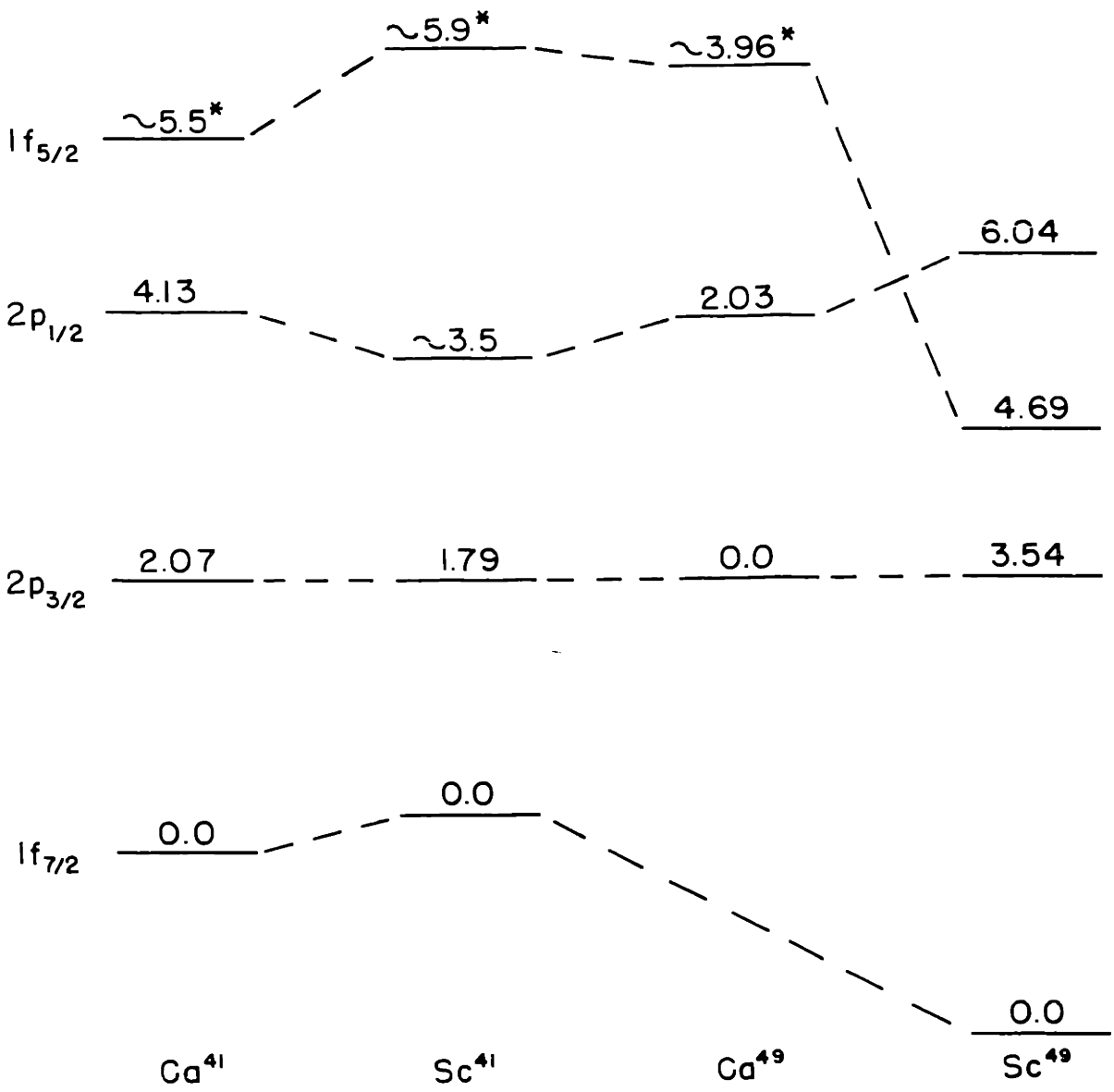

*Lower Limit

The Numbers are Excitation Energies in MeV.

Figure 6.5 Single Particle States

that 2.42 Mev is resonable for the $1f_{7/2} - 2p_{3/2}$ splitting in V^{51} although it is somewhat less than the 3.54 Mev value for Sc^{49}.

The experimental angular distribution of the (α,p) reaction to the V^{51} 2.42 Mev state is shown again later (Figure 6.24) compared to the angular distributions for other assumed 3/2- states studied in this experiment. The similarity of these experimental curves lends further support to the spin assignments.

The peak in the V^{51} spectrum corresponding to the state at 2.42 Mev usually had about the same width as the ground state peak and it was therefore assumed that the 2.545 Mev state was weakly excited (see Figure 6.3). This apparently contradicts the assignment by Schwager (S6) of the proton configuration $(\pi f_{7/2})^2_0(\pi f_{5/2})$ since calculations for this state, using good seniority spectroscopic factors, predict that at 30 degrees the cross-section should be about 60% of the cross-section to the 2.42 Mev state.

Most of the peaks in the V^{51} spectrum corresponding to states above 2.42 Mev clearly contain contributions from more than one state. However, angular distributions were obtained for several prominent groups. The group due to states at about 3.15 Mev excitation is shown in Figure 6.4 with the DWBA curve for $(f_{7/2})^2_0$ neutron transfer and $2p_{3/2}$ proton transfer. The fit is not good and no assignments are made for the spins of the states involved.

The angular distribution for the state(s) at 4.18 Mev excitation (Figure 6.4) has a deep minimum at about 40 degrees and a pronounced secondary maximum. This structure very strongly resembles the calculated curve for $2p_{\frac{1}{2}}$ proton transfer (and $(1f_{7/2})^2_0$ neutron transfer) which is shown with the data. The calculated curve seems to be shifted out by 8 to 10

degrees compared to the data, and thus the overall agreement is not too good. However, this is the only DWBA curve found with the pronounced oscillatory structure and thus $2p_{\frac{1}{2}}$ proton transfer is suggested for the 4.18 Mev peak.

The J dependence of (α,p) angular distributions has been discussed by Lee et al. (L5). Their results for L = 1 are similar to those shown in Figure 6.4. Their calculations required the use of a radial cutoff on the matrix element to produce the oscillatory sturcture of the $2p_{\frac{1}{2}}$ transition. For the calculations presented here no cutoff was used. Since there is no J dependence in the shape of form factor (see Section 5.2, equations 5.6 and 5.13), the difference in shape between the cross-sections for $J = L + \frac{1}{2}$ and $J = L - \frac{1}{2}$ must be produced by the spin - orbit coupling in the proton optical potential.

The calculated curves in Figure 6.4 were done using a form factor for 1f neutron and 2p proton transfer. However, very similar results were obtained using a form factor for $(1f)^3$ L = 1 (see Figure 5.3).

Lee et al. obtained qualitative agreement between theory and experiment for $J\pi = 3/2-$ and $J\pi = \frac{1}{2}-$ transitions in the reactions $Ni^{58}(\alpha,p)Cu^{61}$ and $Ni^{60}(\alpha,p)Cu^{63}$ (2p proton transfer). Specifically, the 3/2- angular distributions were rather smooth while the $\frac{1}{2}-$ ones showed pronounced oscillatory structure. Similar results were obtained by Nolan (N3) for (p,α) reactions on Zn isotopes.

Thus, although no known $J\pi = \frac{1}{2}-$ angular distributions were obtained in this experiment, they may be expected to be at least qualitatively similar to the calculation shown in Figure 6.4.

The calculated J dependence for L = 3 is not as pronounced as that

for L = 1. Figure 6.6 shows the DWBA calculations for $J\pi = 5/2^-$ and $J\pi = 7/2^-$. The latter is shown compared to the experimental ground state angular distribution, and the former is shown compared to the data for the broad peak at about 3.71-3.85 Mev excitation energy. Since there are uncertainties in the theory and the data, no definite assignments were made for these states.

The experimental angular distribution for the (α,p) reaction to the 7.12 Mev state is also shown in Figure 6.6. This curve is unlike all of the present calculated ones and therefore no assignment was made.

6.3.2 $Ca^{44}(\alpha,p)Sc^{47}$

Figure 6.7 shows the experimental $Ca^{44}(\alpha,p)Sc^{47}$ spectrum at 30 degrees LAB and a summary of the known levels in Sc^{47} (from B9, H2, P2, Y1). Also shown are the levels calculated for Sc^{47} by MBZ (M1) and the MBZ spectroscopic factors (equations 5.8 and 5.19) for the (α,p) reaction to the various levels. (The length of each arrow is proportional to the spectroscopic factor for the state opposite the arrow.) The present excitation energy measurements have probable errors of $\pm$ 25 kev for the state at .80 Mev and $\pm$ 50 kev for the rest of the states in Sc^{47}.

As shown in Figure 6.7, the MBZ calculations predict weak excitation of the $f_{7/2}$ shell configuration excited states relative to the ground state. The MBZ spectroscopic factor for the lowest $11/2^-$ state, for example, is only 3% of the ground state value. For the excited states with $J \neq 7/2$ the relatively small spectroscopic factors are a direct result of the lack of an $I = 0$ (I = angular momentum of transfered neutron pair) contribution. This affects the calculation in two ways: 1) the factor $(2I + 1)^{-\frac{1}{2}}$ in equa-

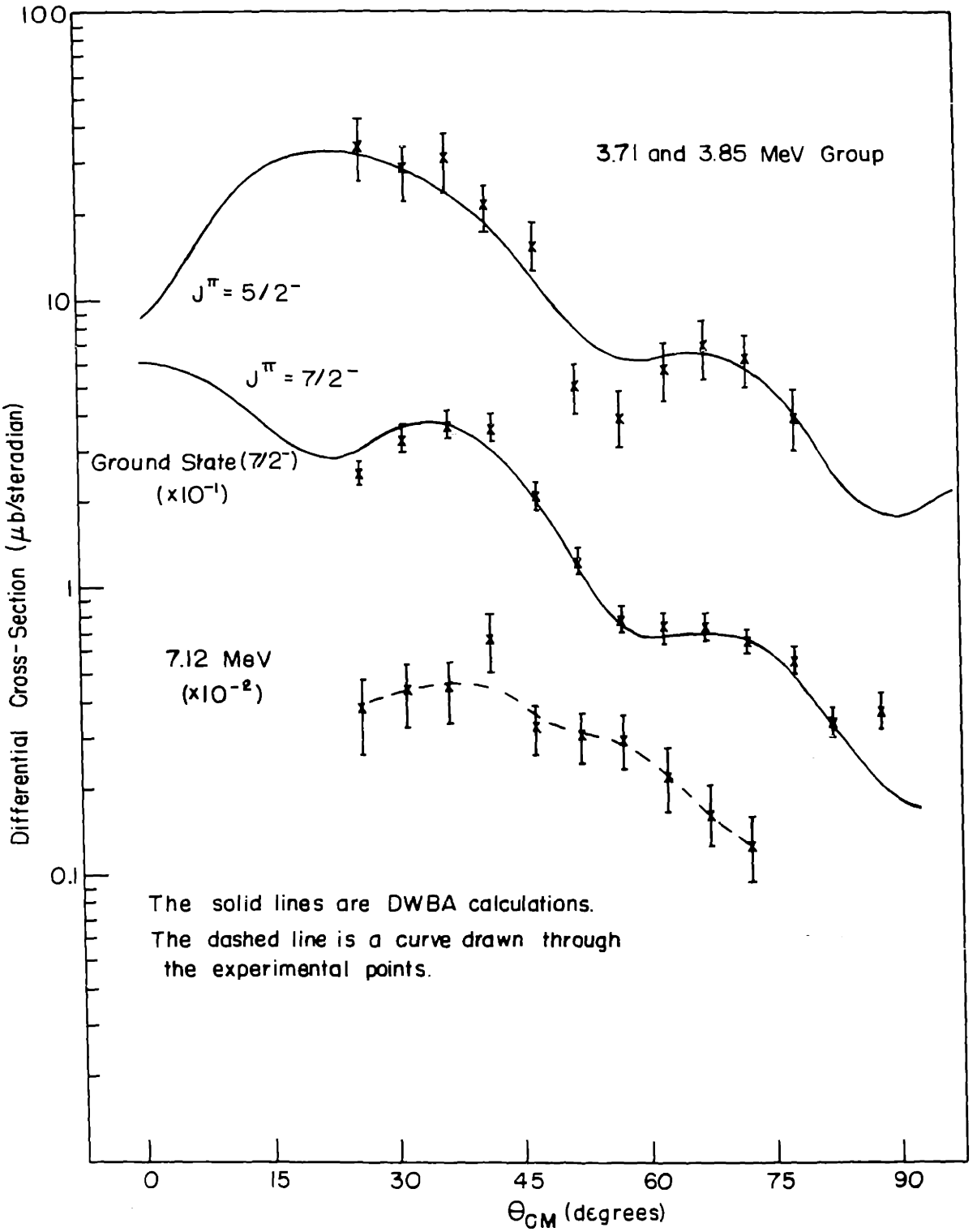

Figure 6.6 $Ti^{48}(\alpha, p)V^{51*}$ Differential Cross-Sections

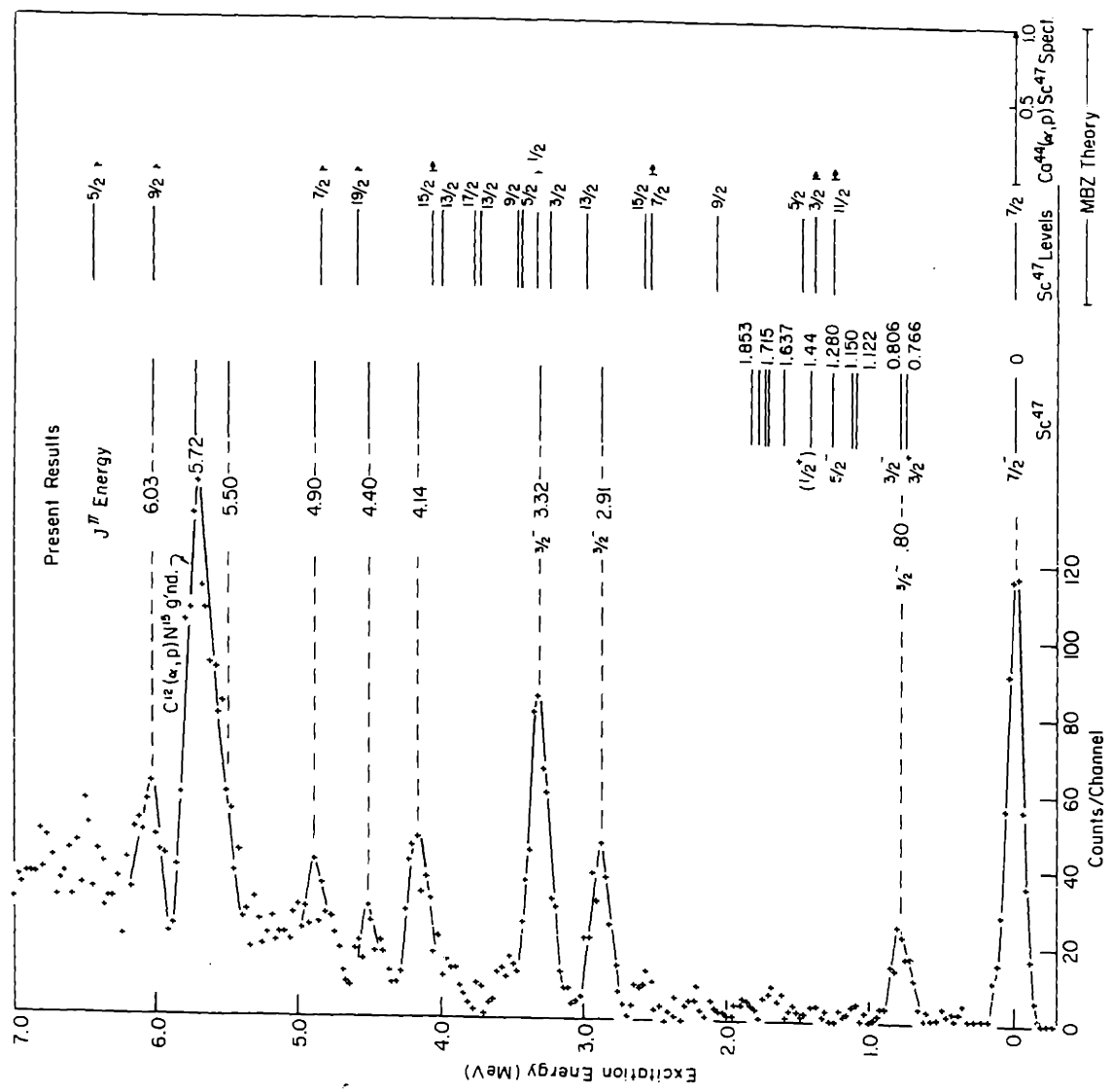

Figure 6.7 $Ca^{44}(\alpha,p)Sc^{47}$ Proton Spectrum at 30°_{LAB} and Sc^{47} Energy Levels

tion 5.8 causes a reduction by a factor of 5 for the I = 2 case compared to the I = 0 case. 2) The two particle fractional parentage coefficients (in equation 5.19) for Sc^{47} (6 neutrons) is a factor of 3 smaller for I = 2 than it is for I = 0. This reduces the spectroscopic factor by a factor of 9. Thus, for these states ($J \neq 7/2$), the large reduction compared to the ground state is independent of the MBZ amplitudes of the components of the wave function for these states. Thus, the (α,p) reaction cannot test these MBZ wave functions, but it can in some cases test the configuration purity of the states and the (α,p) model used. This point was discussed in Section 6.3.1 with reference to the $Ti^{48}(\alpha,p)V^{51}$ reaction.

The excited 7/2- MBZ states can have an I = 0 component and thus can, in principle, be excited by the (α,p) reaction. However, the reduction described above still applies because of the relatively small MBZ amplitude for the I = 0 components of the wave functions. The smallness of these I = 0 amplitudes can, in principle, be tested by the (α,p) reaction, but since these levels have not been found in Sc^{47} only general conclusions may be drawn.

The experimental (α,p) spectrum (Figure 6.7) shows very weak excitation of levels below 2.8 Mev in agreement with the calculations based on $f_{7/2}$ shell wave functions and the direct interaction stripping model for the (α,p) reaction. An exception to the above statement is the state at .80 Mev. From the spectrum alone it is not clear whether this peak corresponds to the 3/2- state at .806 Mev, the 3/2 + ($d_{3/2}$ hole) state at .766 Mev, or contains contributions from both.

The experimental angular distribution for the .80 Mev state is shown in Figure 6.8 along with those for the $Ti^{48}(\alpha,p)V^{51}$ 2.42 Mev (3/2-, see Section 6.3.1) and the $Ca^{44}(p,\alpha)K^{41}$ ground state (3/2+). An (α,p) $J\pi$ =

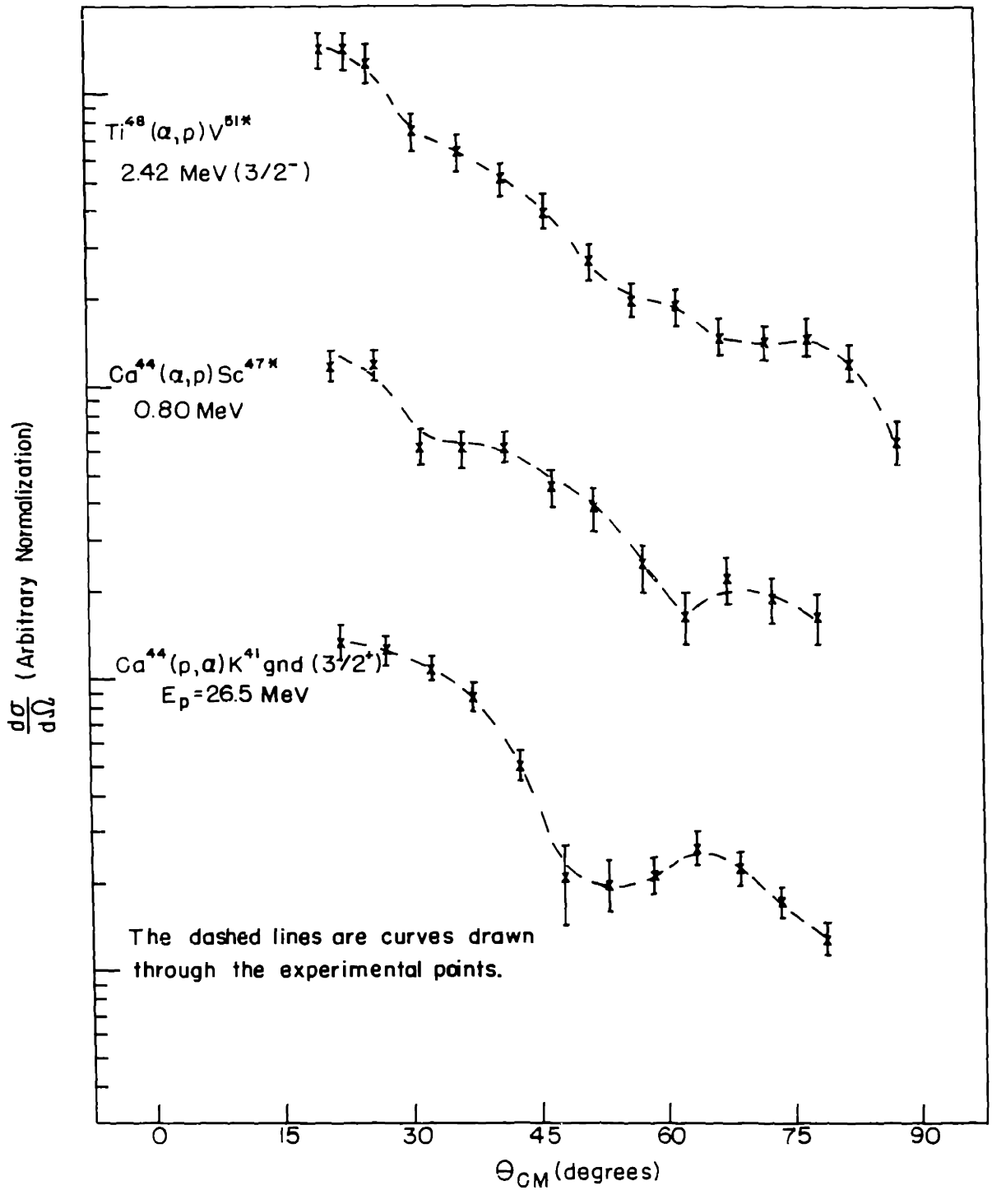

Figure 6.8 $Ca^{44}(\alpha,p)Sc^{47*}$ 0.80 MeV Compared to $3/2^+$ and $3/2^-$ Angular Distributions

3/2+ angular distribution would be expected to be very similar to the latter (see Figure 6.2 and the discussion in Section 6.2.1). The angular distribution of the .80 Mev peak is later (Figure 6.24) compared to the angular distributions of other 3/2- states. These comparisons indicate that at least the major contribution is from the 3/2- state at .806 Mev. Also, this assignment is consistent with the weak excitation of the $d_{3/2}$ hole states in Sc^{45} (see Section 6.2.1) and Sc^{43} (Section 6.2.4) by the (α,p) reaction.

Figure 6.9 shows the DWBA calculation for $(f_{7/2})^2_0$ neutron transfer and $2p_{3/2}$ proton transfer compared to the angular distributions of the (α,p) reaction to states in Sc^{47} at 0.80 Mev, 2.91 Mev and 3.32 Mev. From the angular distributions these states all appear to have spin and parity 3/2-. Since the MBZ spectroscopic factors for all the $1f_{7/2}$ shell configuration 3/2- states are very small (independent of the MBZ amplitudes) it appears that the excitation of these states occurs via admixtures of $2p_{3/2}$ proton configuration (with the neutrons coupled to zero) in the wave functions of these states. Such admixtures have been postulated by MBZ to explain why many observed 3/2- states lie lower in energy than the calculation for pure $1f_{7/2}$ configuration predicts (M1).

Using good seniority spectroscopic factors, and assuming the wave function of the .80 Mev state is

$$\Psi_{(.80)} = \alpha \left[(\pi f_{7/2})(\nu f_{7/2})^6\right]_{3/2^-} + \beta \left[(\pi 2p_{3/2})(\nu f_{7/2})^6_0\right]_{3/2^-}$$

the observed magnitude of the (α,p) cross-section to the .80 Mev state, compared to the ground state, suggests the value of β should be about 0.5. Due to the uncertainties in the calculation, however, this number must be regarded as merely a rough estimate. An obvious uncertainty arises because

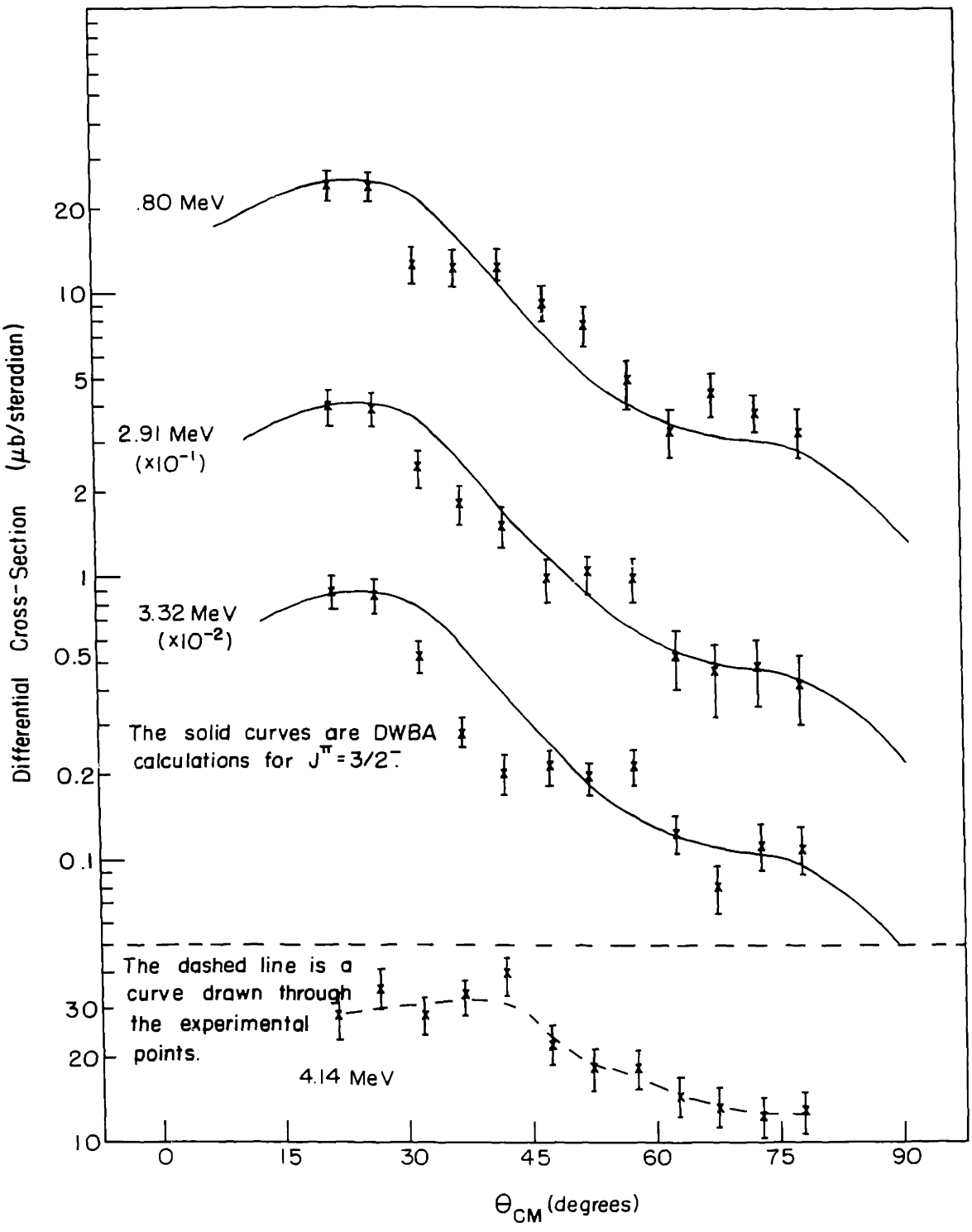

Figure 6.9 $Ca^{44}(\alpha,p)Sc^{47*}$ Differential Cross-Sections

neutron admixtures have not been included. Due to the enhancement of the (α,p) cross-section for 2p neutron transfer (see Section 6.2.3) such admixtures could have a large effect.

The experimental angular distribution of the (α,p) reaction to the 4.14 Mev state, shown in Figure 6.9, is unlike all of the present calculations and so no assignment was made.

The states above 4.14 Mev were identified by the excitation energy in Sc^{47}, but no worthwhile angular distributions were obtained. The peaks corresponding to the states at 5.72 and 5.50 were obscured at small angles the (α,p) ground state peak from the C^{12} impurity (see Figure 6.7), but at larger angles peaks were identified with these excitation energies.

6.3.3 $Ca^{42}(\alpha,p)Sc^{45}$

The experimental $Ca^{42}(\alpha,p)Sc^{45}$ proton spectrum is shown in Figure 6.10 along with a summary of known levels in Sc^{45} (from B9, P2 and Y2). Also shown are the $f_{7/2}$ shell levels calculated by MBZ, and the calculated spectroscopic factors for these levels. The length of eacharrow is proportional to the spectroscopic factor for the (α,p) reaction to the level opposite the arrow. The present results for excita tion energies in Sc^{45} and spin assignments (uncertain assignments are shown in brackets) are given opposite each peak. The probable errors in the present excitation energies are $\pm$ 30 kev for levels below 2 Mev and $\pm$ 50 kev for the rest.

The situation is considerably more complicated in Sc^{45} than it was in Sc^{47} and V^{51}. In contrast to the latter two nuclei, observable but still rather weak (α,p) excitations are predicted for several of the low lying

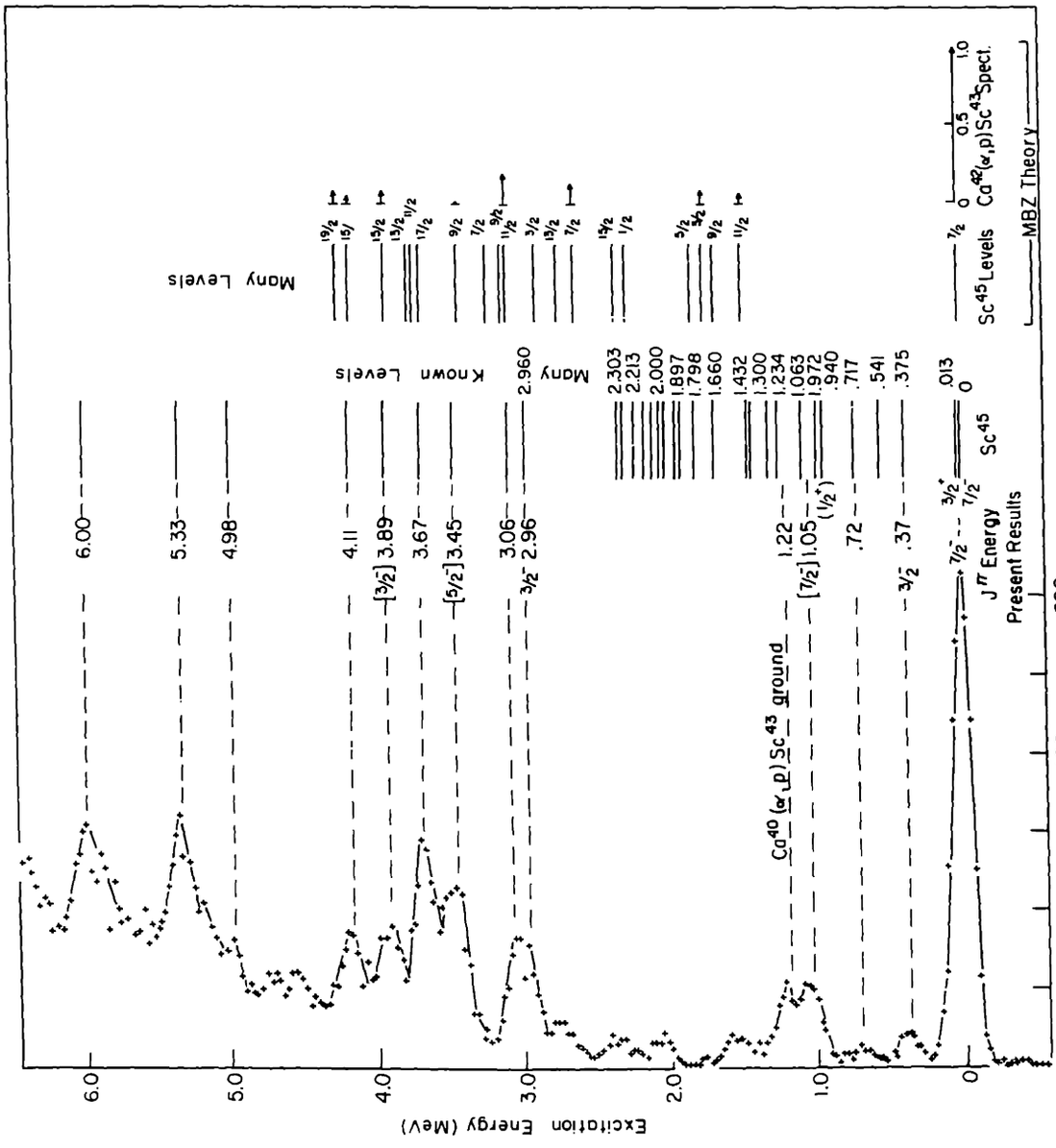

Figure 6.10 $Ca^{42}(\alpha,p)Sc^{43}$ Proton Spectrum at 35°_{LAB} and Sc^{45} Energy Levels

$f_{7/2}$ shell (MBZ) states in Sc^{45}. In addition, many levels are known in Sc^{45} but very few spins and parities are known.

The weak excitation of the 3/2+ ($d_{3/2}$ hole) state at 13 kev was discussed in Section 6.2.1. As pointed out there, the weak excitation of this state supports the assumption that the mechanism for the (α,p) reaction is stripping.

The differential cross-section for the (α,p) reaction to the state at 0.37 Mev is shown in Figure 6.11 along with the DWBA calculation for $J\pi = 3/2-$. This curve was calculated for the transferred neutrons and the proton all going into the $f_{7/2}$ shell, but it is very similar to the curve for $(f_{7/2})^2$ neutron transfer and $2p_{3/2}$ proton transfer (see Figure 5.3).

The experimental angular distribution for the 0.37 Mev state is shown again in Figure 6.24 compared to the angular distributions for other assumed 3/2- states. The similarity with the other curves and with the calculation suggests that the spin and parity of the 0.37 Mev state is 3/2- even though the experimental angular distribution oscillates somewhat more than the calculated curve. This 3/2- assignment is supported by the β decay scheme of Ti^{45}. The branching ratio for the β decay of Ti^{45} to the 0.37 Mev level in Sc^{45} is less than 0.1% of the ground state decay (R1). This suggests spins and parities of 7/2- for the ground state of Ti^{45} and 3/2- for the 0.37 Mev level in Sc^{45}.

The angular distribution for the (α,p) reaction to the 1.05 Mev level is also shown in Figure 6.11 along with the calculated curve for $J\pi = 7/2-$. The fit is quite good except at small angles, but the experimental cross-section may contain contributions from more than one state and thus this spin assignment is rather uncertain.

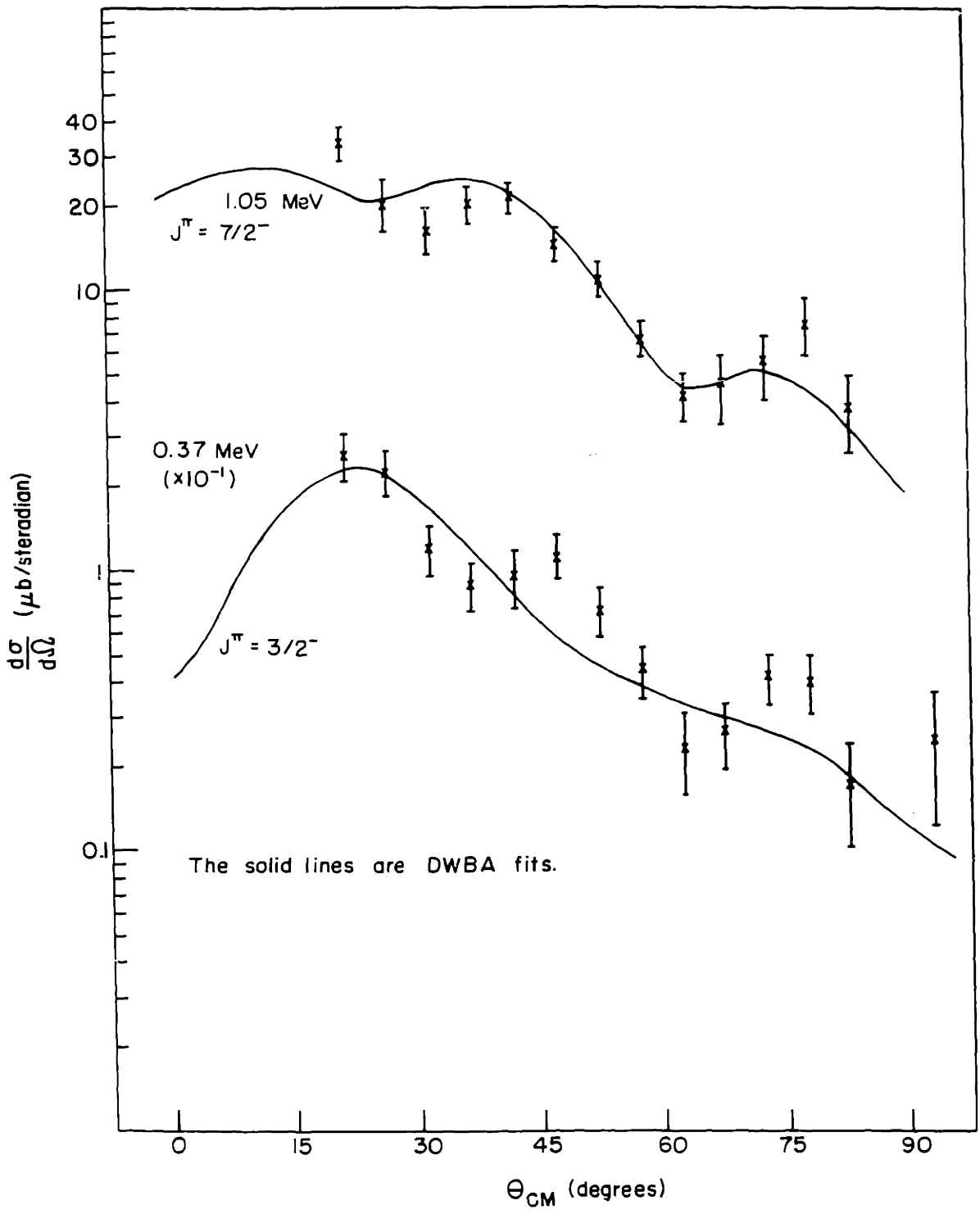

Figure 6.11 $Ca^{42}(\alpha,p)Sc^{45*}$ Differential Cross-Sections

The angular distribution of the peak at 1.22 Mev is shown at the top of Figure 6.12. This peak occurs at very nearly the same place as the $Ca^{40}(\alpha,p)Sc^{43}$ ground state peak from the Ca^{40} impurity in the Ca^{42} target. The contribution to the cross-section from the Ca^{40} impurity was calculated from the known $Ca^{40}(\alpha,p)Sc^{43}$ ground state cross-section and the amount of Ca^{40} (5%) in the target. The lower curve in Figure 6.12 is the result of subtracting the Ca^{40} contribution (roughly 50%) from the original cross-section. The DWBA curve for $J\pi = 11/2-$ seems to fit the data, but, due to the large theoretical and experimental uncertainties, this suggested assignment should not be taken too seriously unless additional data becomes available.

The next highest prominent peak in the Sc^{45} spectrum contains contributions from at least two states, and excitation energies of 2.96 Mev and 3.06 Mev were assigned to this peak. At small angles, the 2.96 Mev state dominated, but at larger angles (greater than 30 degrees) the peak was analysed as two states.

The differential cross-sections are shown in Figure 6.13. The one for the 2.96 Mev state is shown with the calculation for $2p_{3/2}$ proton transfer, and based on the fit, the state was assigned the spin and parity 3/2-. The angular distribution for the 3.06 Mev state is incomplete, and no spin assignment was made.

The next group of peaks was analyzed as four states, and angular distributions, shown in Figures 6.13 and 6.14, were obtained for three of them. The 3.45 Mev state has an angular distribution similar to that calculated for $J\pi = 5/2-$ (Figure 6.13), but, since no known 5/2- states have been observed in the present experiment, this assignment is uncertain.

The angular distributions for the 3.67 and 3.89 Mev states are shown

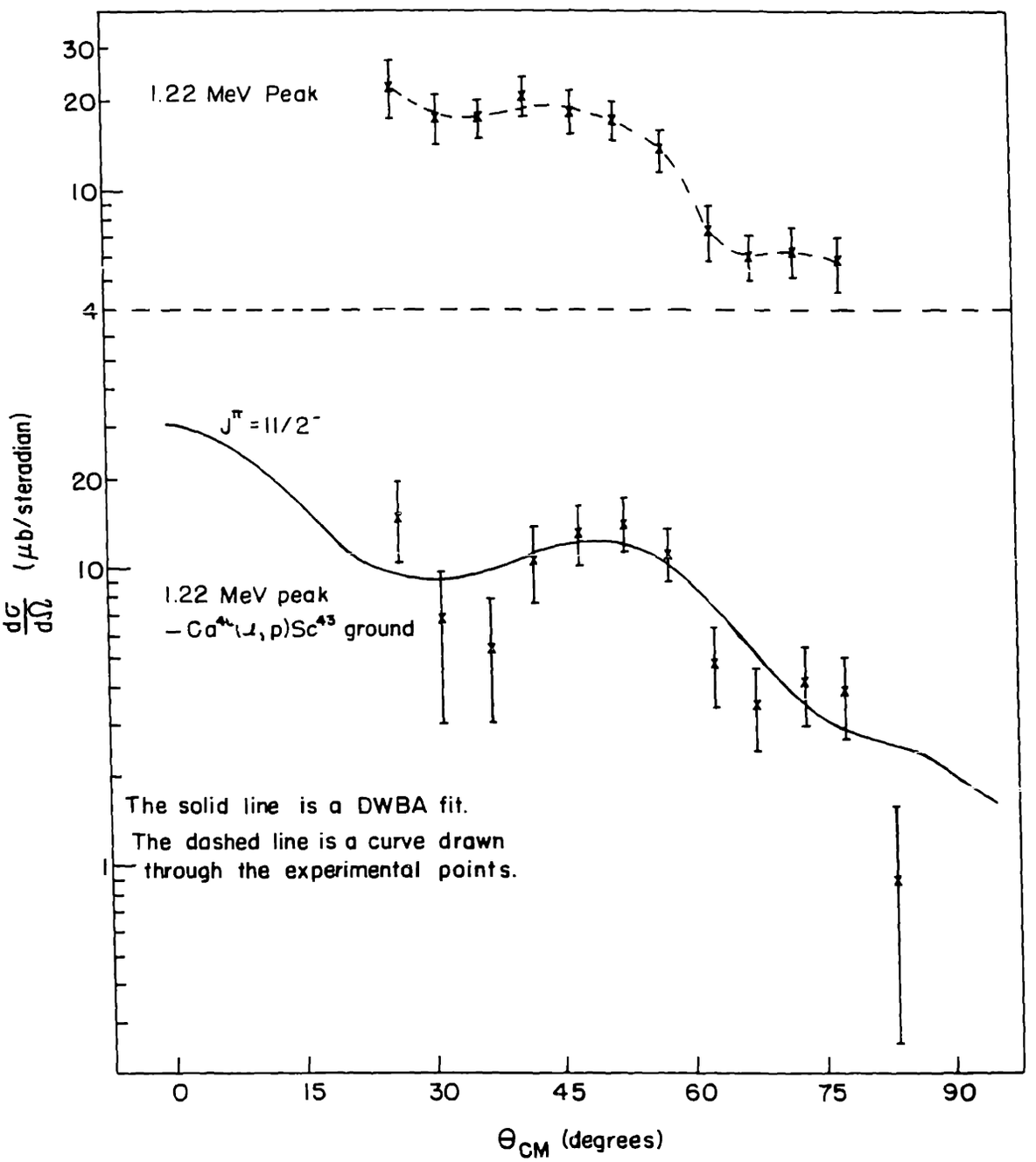

Figure6.12 $Ca^{42}(\alpha,p)Sc^{45*}$ 1.22 MeV Differential Cross-Section

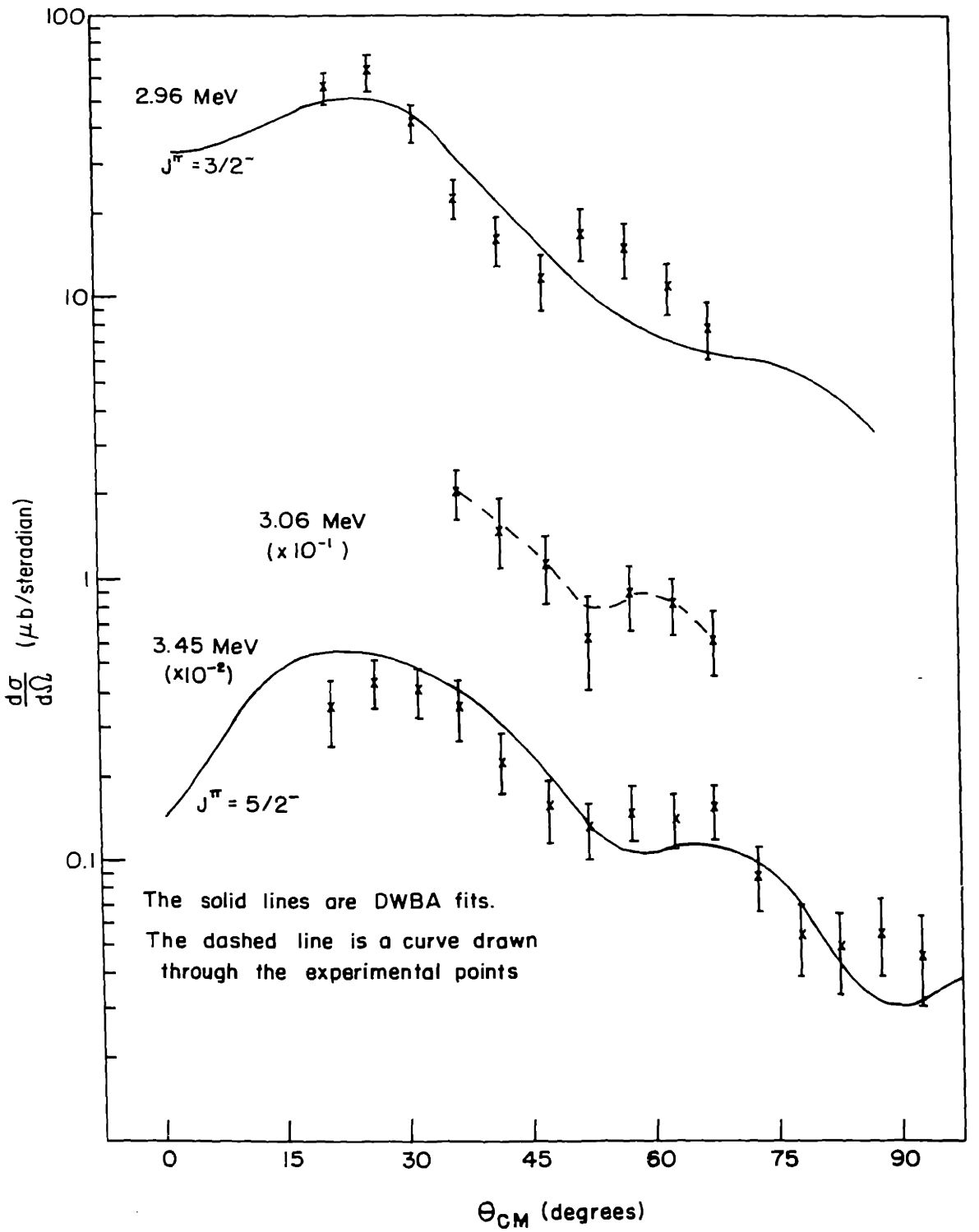

Figure 6.13 $Ca^{42}(\alpha,p)Sc^{45*}$ Differential Cross-Sections

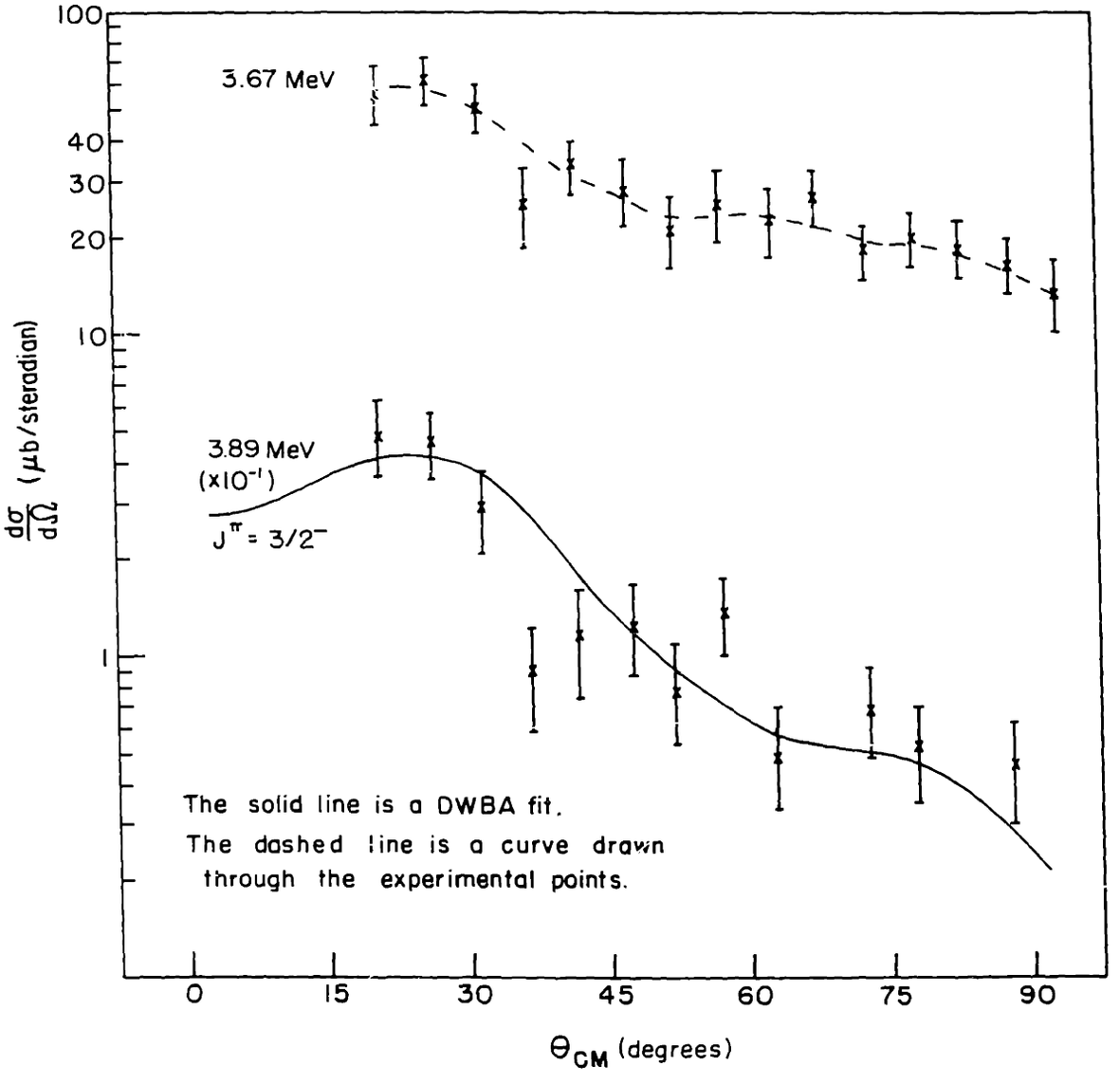

Figure 6.14 $Ca^{42}(\alpha,p)Sc^{43*}$ Differential Cross-Sections

in Figure 6.14. The former is unlike any of the present calculations, and no conclusions were drawn. The latter is shown compared to the DWBA curve for $2p_{3/2}$ proton transfer. Although the fit is not too good, it is better than any of the other calculations, and so this assignment is suggested.

The four states above 4 Mev were identified by the excitation energies in Sc^{45}, but no worthwhile angular distributions were obtained.

6.3.4 $Ca^{40}(\alpha,p)Sc^{43}$

The experimental $Ca^{40}(\alpha,p)Sc^{43}$ proton spectrum is shown in Figure 6.15 along with experimental and theoretical (MBZ) Sc^{43} levels. To the right of each peak is shown the present spin and parity assignment (uncertain assignments are in brackets) and the excitation energy in Sc^{43}. The probable errors in the measured excitation energies are $\pm$ 30 kev for states below 3 Mev and $\pm$ 50 kev for states above 3 Mev. The level scheme to the right of the present results is a summary of the known levels in Sc^{43} (from Al, B10, I6, P2 and S7). The separate results from each of these references are compared to the present results in Figure 6.16.

Also shown in Figure 6.15 are the excitation energies and L values obtained by the $Ca^{42}(He^3,d)Sc^{43}$ reaction (S7). Finally, the MBZ results for the energies of the $f_{7/2}$ shell states, the (α,p) spectroscopic factors, and the (He^3,d) spectroscopic factors are shown. The length of each arrow is proportional to the spectroscopic factor for the MBZ level opposite the arrow.

The γ decay scheme for the low lying levels (from Al and B10) is shown in Figure 6.17. The levels marked with short arrows were strongly

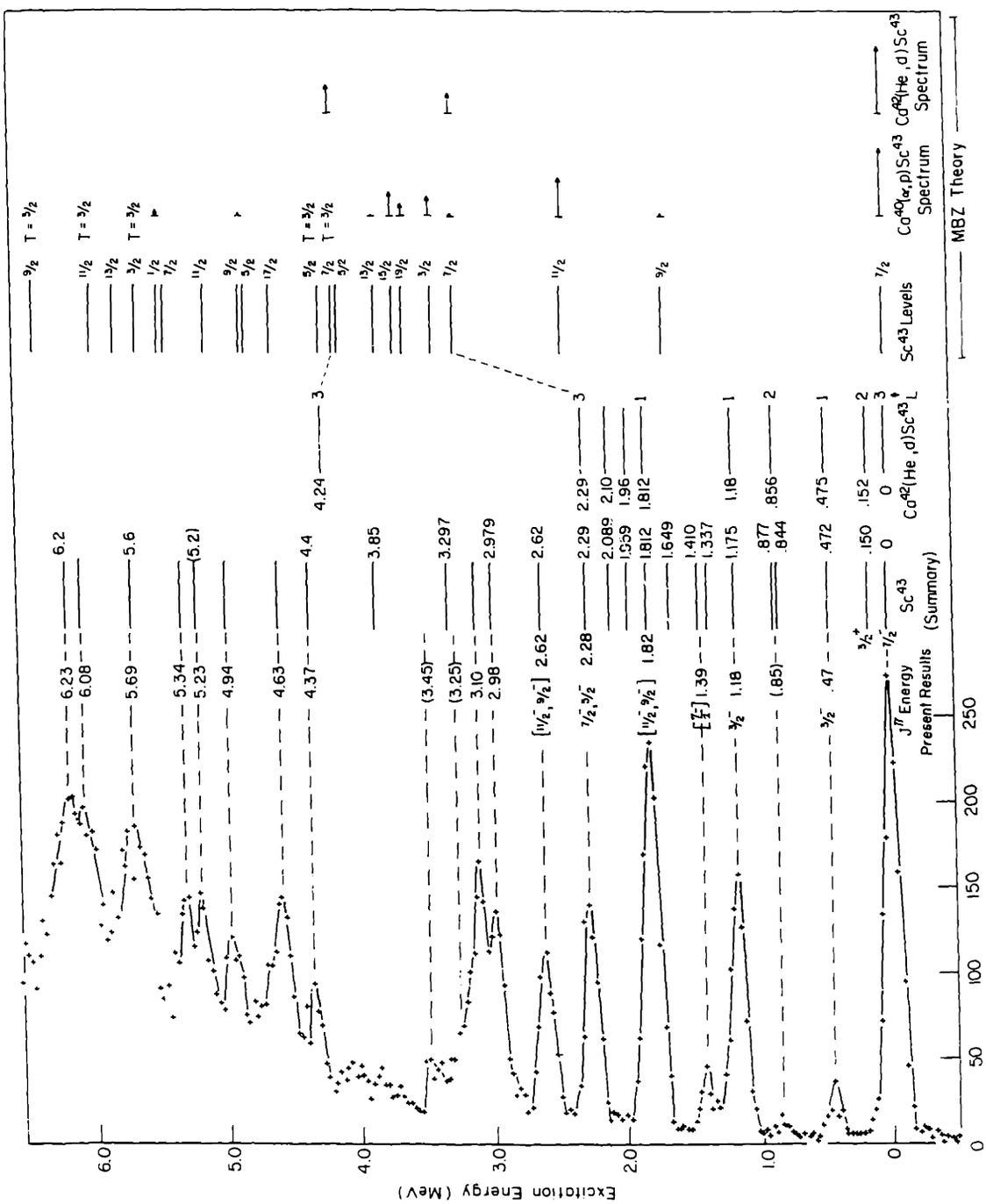

Figure 6.15 $Ca^{40}(\alpha,p)Sc^{43}$ Proton Spectrum at 45°_{LAB} and Sc^{43} Energy Levels

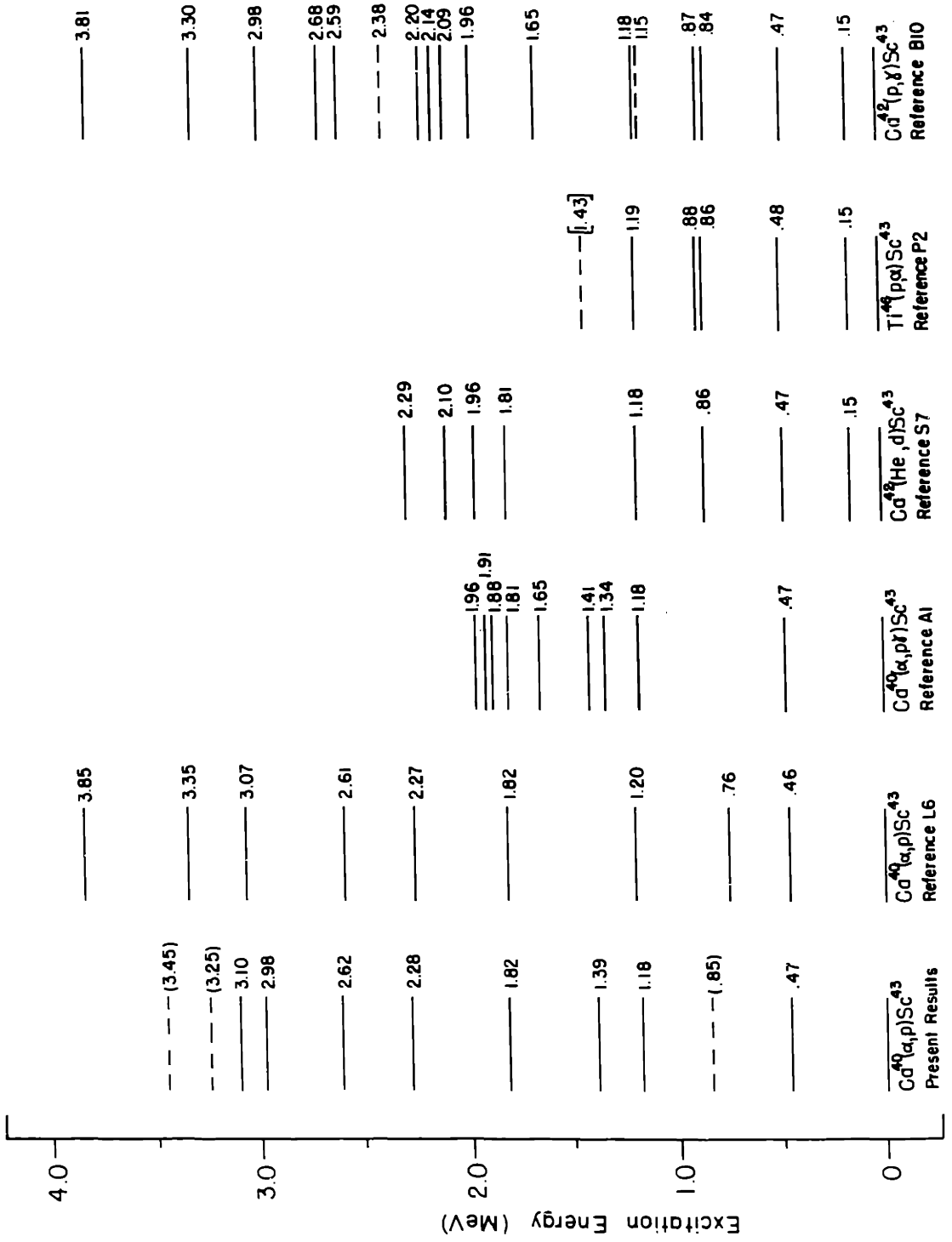

Figure 6.16 Sc^{43} Energy Levels

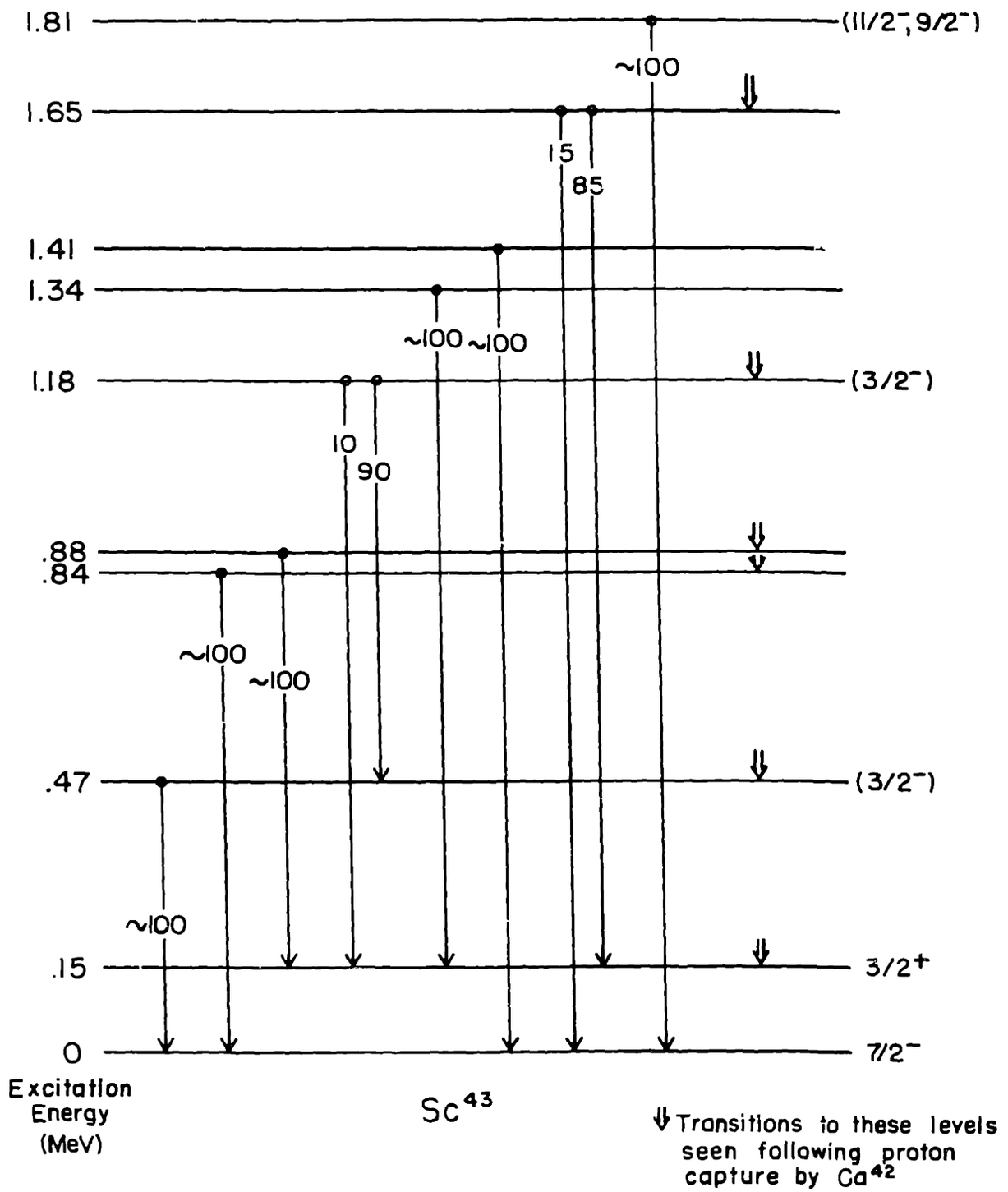

Figure 6.17 Sc^{43} γ decay Scheme

populated by the γ rays from the resonance levels in the $Ca^{42}(p,\gamma)Sc^{43}$ reaction. Since no direct transitions from the resonance levels to the 7/2- ground state were seen, the strongly populated levels most probably have J equal to or less than 5/2 (B10). The γ ray data will be referred to again later when each spin assignment is discussed.

From the experimental energy spectrum in Figure 6.15, it is clear that the first excited state (3/2+ at .150 Mev) in Sc^{43} is very weakly (if at all) excited by the (α,p) reaction. The excellent agreement between the present and previous results for the energies of the levels at .47, 1.18, 1.82 and 2.28 Mev indicates that the mean position of the ground state peak is not significantly affected by any contribution from the .15 Mev state. Also, by fitting the ground state peak with two gaussian curves separated by .15 Mev, it was found that the contribution from the .15 Mev state was less than about 5 - 10% of the ground state at all angles.

The .15 Mev state in Sc^{43} is believed to be a $d_{3/2}$ hole state (formed by promoting a $d_{3/2}$ proton to the $f_{7/2}$ shell) (B7, H2). The inhibited M2 γ decay to the ground state, with a lifetime of 656 μsec or 190 times the single-particle estimate (H2), implies that the major part of the wave function is

$$\psi(3/2^+) = \alpha_0 \left[(d_{3/2})^{-1}(f_{7/2})^4_0\right]_{3/2^+} + \alpha_2 \left[(d_{3/2})^{-1}(f_{7/2})^4_2\right] \qquad (6.2)$$

with a core excitation probability, α_2^2, of about 0.4 (L7). The second term on the right hand side of equation 6.2 was necessary to explain the large inhibition of the M2 decay to the ground state.

As explained in Section 6.1, the fact that the hole states are weakly excited by the (α,p) reaction is evidence that the dominant reaction

mechanism is stripping and that the admixtures of the proton configuration $(d_{3/2})^{-2}(f_{7/2})^2$ in the ground states of the Ca isotopes are relatively small. A 15 - 20% admixture of $(1d_{3/2})^{-2}(1f_{7/2})^2$ configuration in the ground state of Ca^{40} has been suggested by Belote, Sperduto and Buechner from the $Ca^{40}(d,p)Ca^{41}$ reaction (B11), assuming that the 2.017 Mev level in Ca^{41} is a $d_{3/2}$ hole state. The present (α,p) results do not contradict an admixture of this magnitude.

Two low lying states in Sc^{43}, at 0.47 and 1.18 Mev, have (α,p) angular distributions, shown in Figure 6.18, consistent with $J\pi = 3/2-$ assignments. The experimental angular distribution of the 1.18 Mev state is shown again in Figure 6.24 with angular distributions from other assumed 3/2- states. These assignments are both consistent with the L = 1 assignment from the $Ca^{42}(He^3,d)Sc^{43}$ data (S7).

The 0.47 Mev level γ decays almost entirely to the ground state (see Figure 6.17). The branch to the .15 Mev state is less than 5%. The decay of the 0.47 Mev state seems inconsistent with the 3/2- assignment since a 3/2- state can decay by E2 radiation to the ground state and E1 radiation to the 3/2 + state, and unless the latter is inhibited for some reason, it should dominate. However, an inhibition of the decay to the 3/2+ state is not unreasonable in this case because of the hole configuration of the .15 Mev state. As explained above, the M2 decay of this state to the ground state is strongly inhibited. However, single particle estimates favor the transition to the .15 Mev state by a factor of about 10^5, and thus a very large inhibition would be necessary to explain the decay if the spin of the .47 Mev state is 3/2-.

Assuming the L = 1 assignment from the $Ca^{42}(He^3,d)Sc^{43}$ reaction is

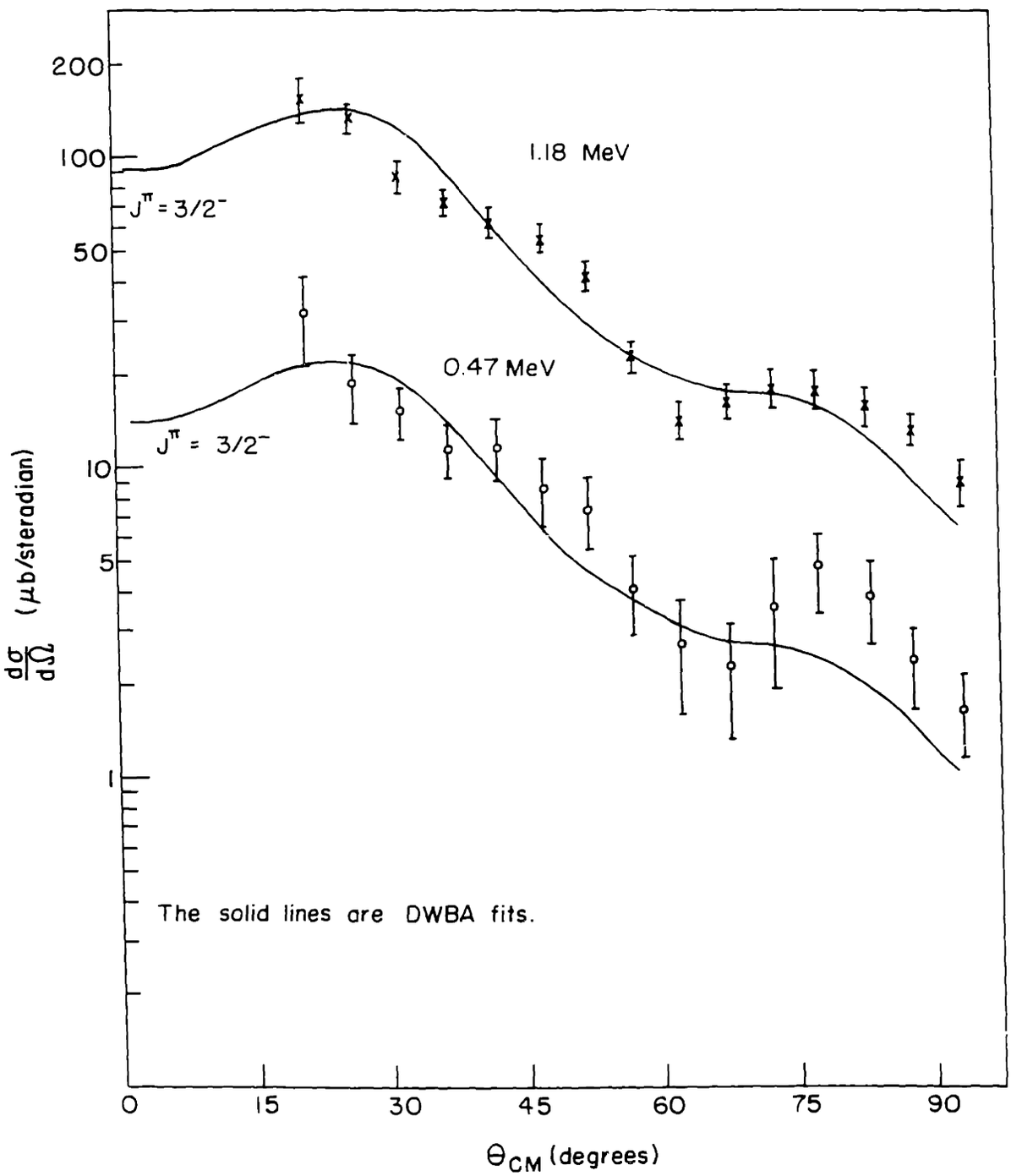

Figure 6.18 $Ca^{40}(\alpha,p)Sc^{43*}$ Differential Cross-Sections

correct, the 0.47 Mev state might have spin and parity $\frac{1}{2}$-. This assignment is inconsistent with the (α,p) angular distribution which agrees quite well with the calculation for $J\pi = 3/2-$. Also, the angular distribution for a $\frac{1}{2}$- state is expected to have pronounced oscillatory structure (see Section 6.3.1) and thus should be easily recognized. Also, based on the γ decay, a $\frac{1}{2}$- assignment for the 0.47 Mev state is less probable than 3/2- since the former implies that M3 radiation (to the ground state) is dominating over E1 radiation (to the 3/2+ level).

The situation for the 1.18 Mev state is similar to the 0.47 Mev state. 3/2- assignments to both states imply that the 1.18 Mev state can decay by M1 or E2 radiation to the 0.47 Mev state and by E1 radiation to the 3/2+. Single particle estimates for this case favor the decay to the .15 Mev state by a factor of about 120. Due to the possible inhibition (described above), lack of strong transitions to the .15 Mev state was not considered conclusive evidence to refute the 3/2- assignments.

The above reasoning also suggests that the states which decay mostly to the 3/2+ state are also hole states and thus the decay to the $d_{3/2}$ hole state would not be strongly inhibited. The assumption of hole configurations for these states is supported by the fact that none of them were strongly excited by the present (α,p) reaction.

The 1.39 and 2.28 Mev states in Sc^{43} exhibit angular distributions, shown in Figure 6.19, which are quite similar to the ground state angular distributions and the $J\pi = 7/2-$ calculations. The calculation for $J\pi = 5/2-$ is also shown in Figure 6.19. Judging from this figure, a distinction between 7/2- and 5/2- states cannot be made on the basis of the present fits to the (α,p) data.

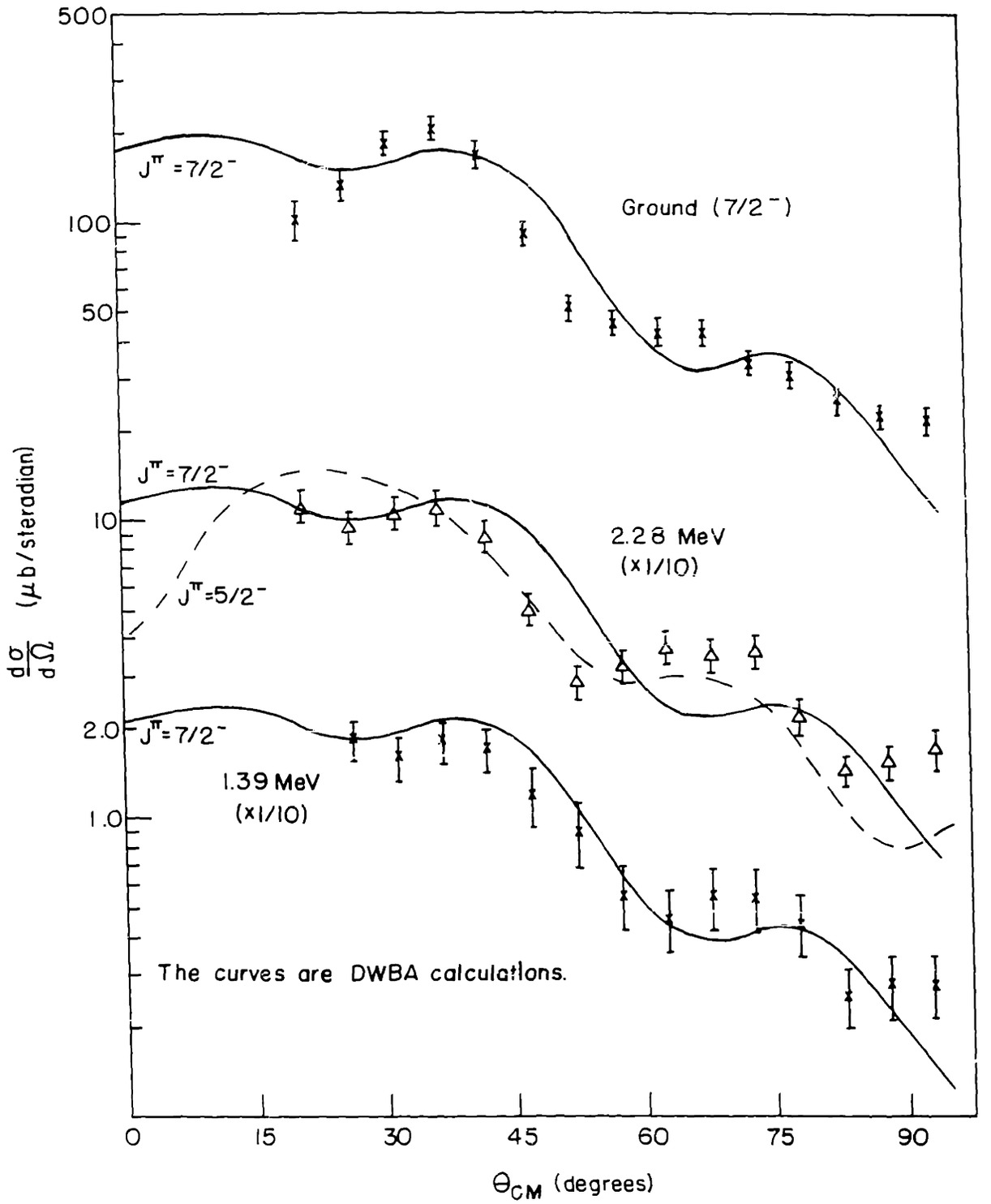

Figure 6.19 $Ca^{40}(\alpha, p)\, Sc^{43\,*}$ Differential Cross-Sections

The fact that the 1.39 Mev state was not seen following proton capture by Ca^{42} suggests $J \geq 7/2$. If this state is identified with the 1.41 Mev state (from Al) then the γ decay mostly to the ground state also favors the higher spin.

The 7/2- or 5/2- assignment to the 2.28 Mev state agrees with the L = 3 assignment from the (He^3,d) experiment. As shown in Figure 6.15, the MBZ theory predicts the excitation of three 7/2- (L = 3) states by the $Ca^{42}(He^3,d)Sc^{43}$ reaction: the ground state, a state at about 3 Mev and the analog of the Ca^{43} ground state at about 4.2 Mev. The analog state (T = 3/2) should not be excited by the $Ca^{40}(\alpha,p)Sc^{43}$ reaction since the (α,p) reaction can only change T by $\frac{1}{2}$. The experimental state at 4.24 Mev in the $Ca^{42}(He^3,d)Sc^{43}$ spectrum is apparently the Ca^{43} analog, and so the state at 2.29 Mev may be the other MBZ 7/2-state. The (α,p) spectroscopic factor for this state is, however, quite small while the 2.28 Mev state is strongly populated by the (α,p) reaction. There are two factors which could cause the MBZ spectroscopic factor to be too small. 1) The smallness of the MBZ spectroscopic factor is due to a cancellation between the I = 0 and I = 2 terms in equation 5.8. Thus, relatively small changes in the MBZ amplitudes in the wave function could make the calculated spectroscopic factor considerably greater. 2) In addition, an admixture of other neutron configurations might lead to stronger excitation than that predicted considering only the $f_{7/2}$ shell. Thus, the 7/2- assignment to the 2.29 Mev state is favored although it could be a 5/2- state which is excited via a $1f_{5/2}$ proton admixture in the wave function.

The angular distributions of the (α,p) reaction to the 1.82 Mev and 2.62 Mev states are shown in Figure 6.20 with DWBA fits for $J\pi = \frac{1}{2}-$. Also

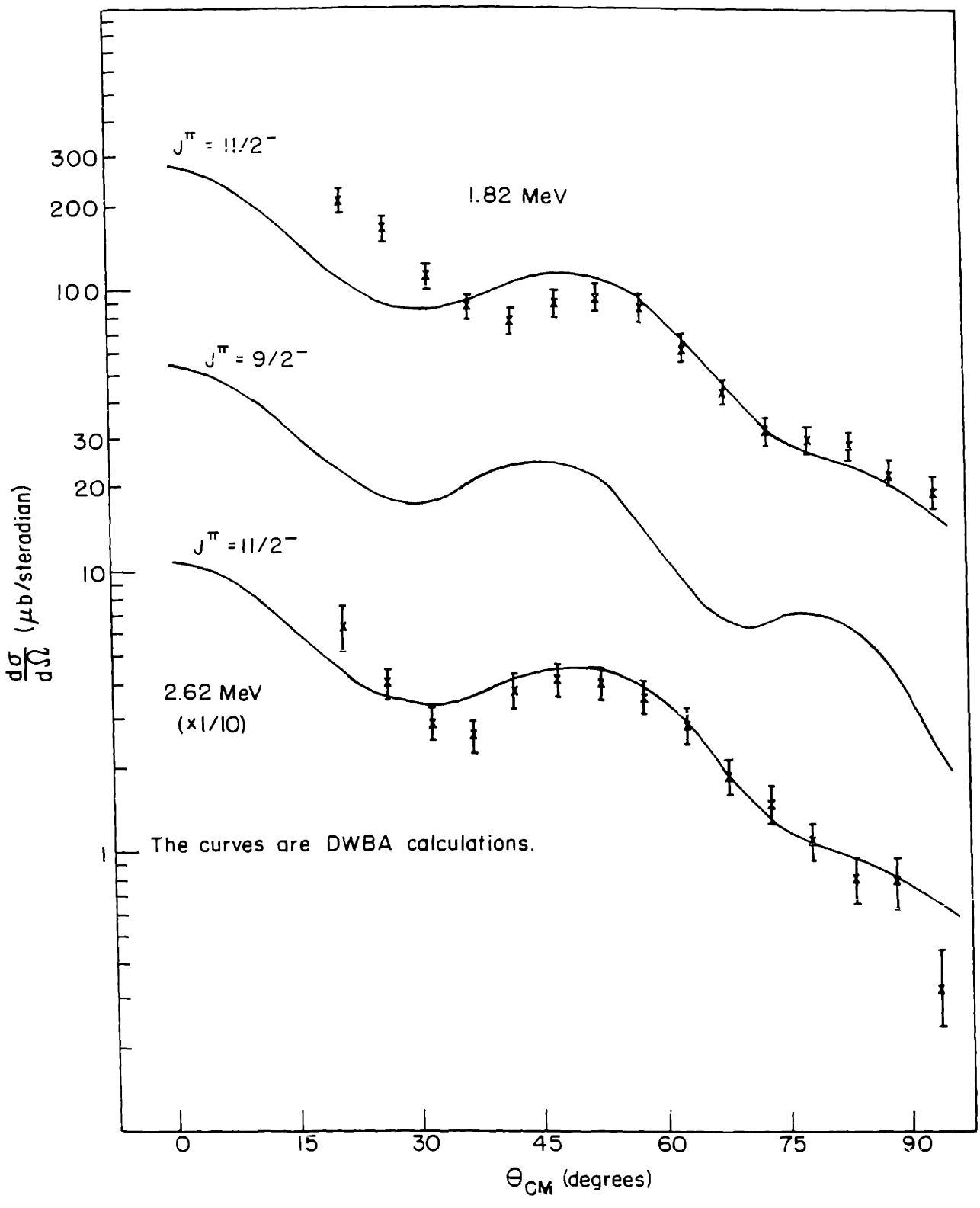

Figure 6.20 $Ca^{40}(\alpha,p)Sc^{43*}$ Differential Cross-Sections

shown, for comparison, is the calculated curve for $J\pi = 9/2-$. Due to the lack of known (α,p) or (p,α) $L = 5$ transitions these assignments are considered somewhat uncertain. Also, from the similarity between the two calculated curves it appears impossible to tell the difference between 9/2- and 11/2- transitions on the basis of the (α,p) angular distributions.

The present $L = 5$ assignment for the 1.82 Mev state disagrees with the (He^3,d) assignment of $L = 1$. However, the fact that this state is not seen in the $Ca^{42}(p,\gamma)Sc^{43}$ reaction and the γ decay almost completely to the ground state both support a spin assignment of $J \geq 7/2$. If the 1.82 Mev state corresponds to either the 9/2- or 11/2- MBZ states it is not clear how it is excited by the (He^3,d) reaction or why it was assigned $L = 1$. Also, if it corresponds to the 9/2- MBZ state it is not clear why it is so strongly excited by the (α,p) reaction.

The experimental angular distributions for the 2.98 Mev and 3.11 Mev states are shown in Figure 6.21. No fits are shown since these curves are not very similar to any of the calculations. However, the deep minimum at about 50 degrees in the angular distribution for the 2.98 Mev state is suggestive of the calculation for $J\pi = \frac{1}{2}-$ (see Section 6.3.1).

The levels above 3.10 Mev were identified by the excitation energy in Sc^{43}, but no worthwhile angular distributions were obtained for them.

The assumed level scheme for Sc^{43} is shown in Figure 6.22 along with the Sc^{43} levels calculated by two different methods. For the first method, using a cluster model (S8), the negative and positive parity states are shown separately. The low lying (below about 3.5 Mev) negative parity states are described by unexcited Ca^{40} and triton clusters, while the positive states are described by unexcited K^{39} and He^4 clusters.

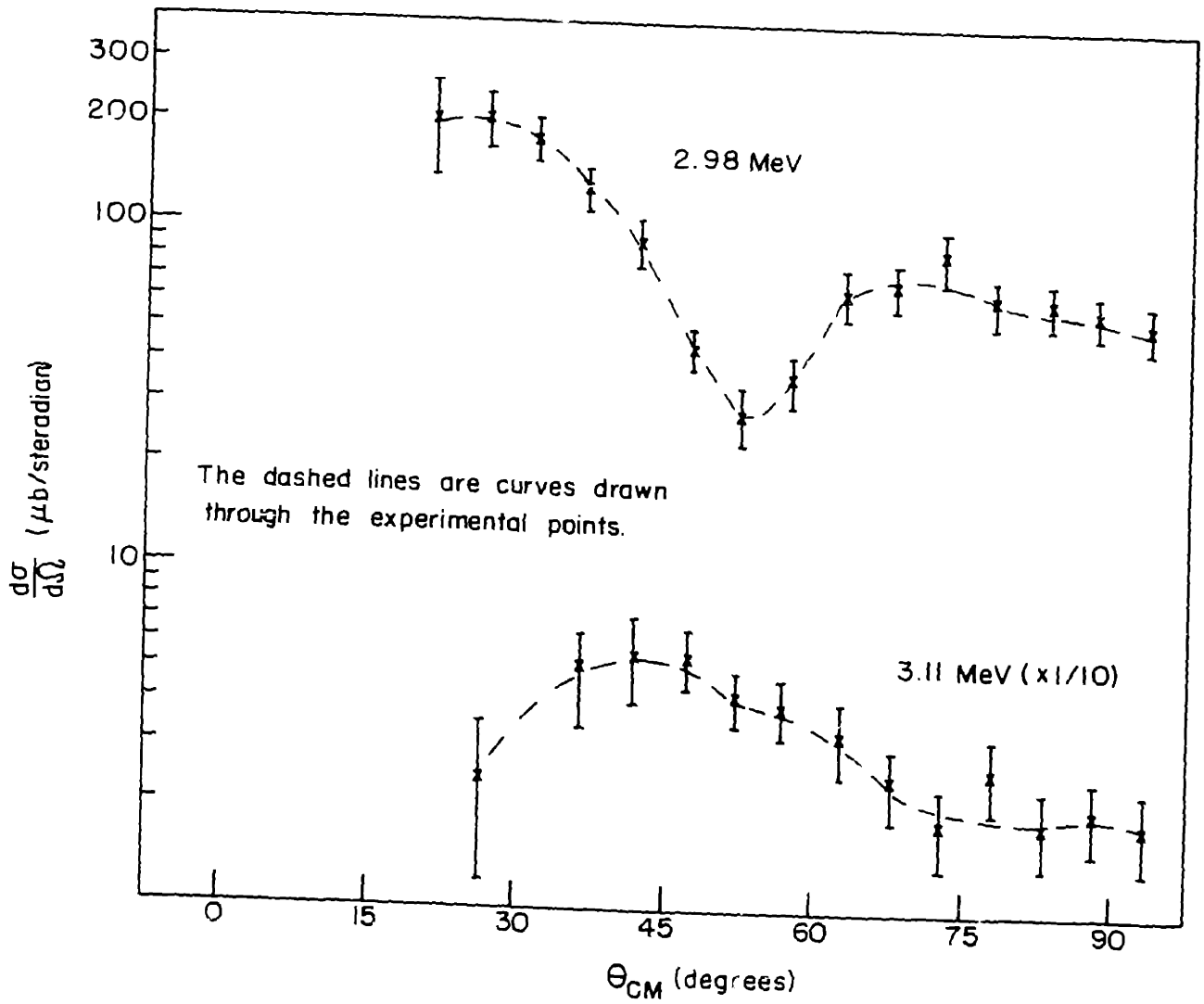

Figure 6.21 $Ca^{40}(\alpha,p)Sc^{43*}$ Differential Cross-Sections

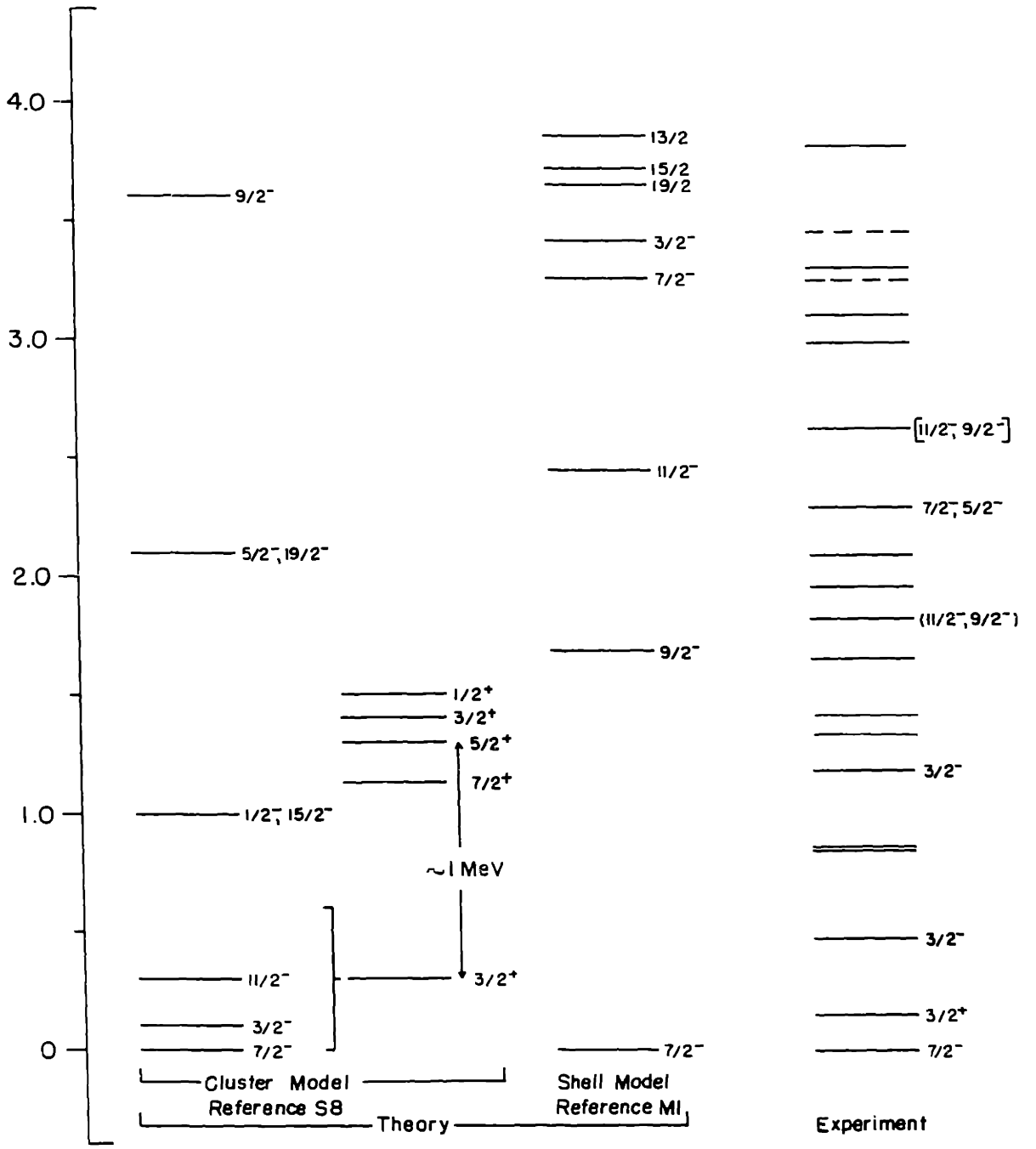

Figure 6.22 Theoretical and Experimental Sc^{43} Energy Levels

The other calculated spectrum shown in Figure 6.22 is that of MBZ (M1). For this calculation, Ca^{40} was taken to be a core, and the energy levels were assumed to arise from the residual interaction between the three nucleons in the $1f_{7/2}$ shell. The two body residual interaction was taken from the experimental levels in Sc^{42}.

Neither model provides good quantitative agreement with the experimental levels. The cluster representation has the feature that low lying levels of both parities are predicted, in qualitative agreement with the experimental results. The MBZ shell model calculation only predicts negative parity states since the Ca^{40} core was assumed to have closed neutron and proton shells. The low lying 3/2+ state clearly indicates a case where this assumption is not correct. There are also many more negative parity low lying states in Sc^{43} than the MBZ calculation predicts, indicating the participation of higher shells (e.g. $2p_{3/2}$, $1f_{5/2}$, $2p_{\frac{1}{2}}$) in at least some of these states.

6.3.5 $Ca^{48}(\alpha,p)Sc^{51}$

The experimental $Ca^{48}(\alpha,p)Sc^{51}$ proton spectrum is shown in Figure 6.23. The present results for the excitation energies are shown opposite the experimental peaks. The probable errors in these energies are ± 30 kev for states below 2 Mev and ± 50 kev for the rest. The Sc^{51} energy level diagram is also shown in Figure 6.23, with the energies observed by Erskine and Marinov (E2) shown to the right of the levels.

The large peaks (note the change of scale at 3.5 Mev) at 3.95 Mev and 5.62 Mev are believed to be due to protons, and thus correspond

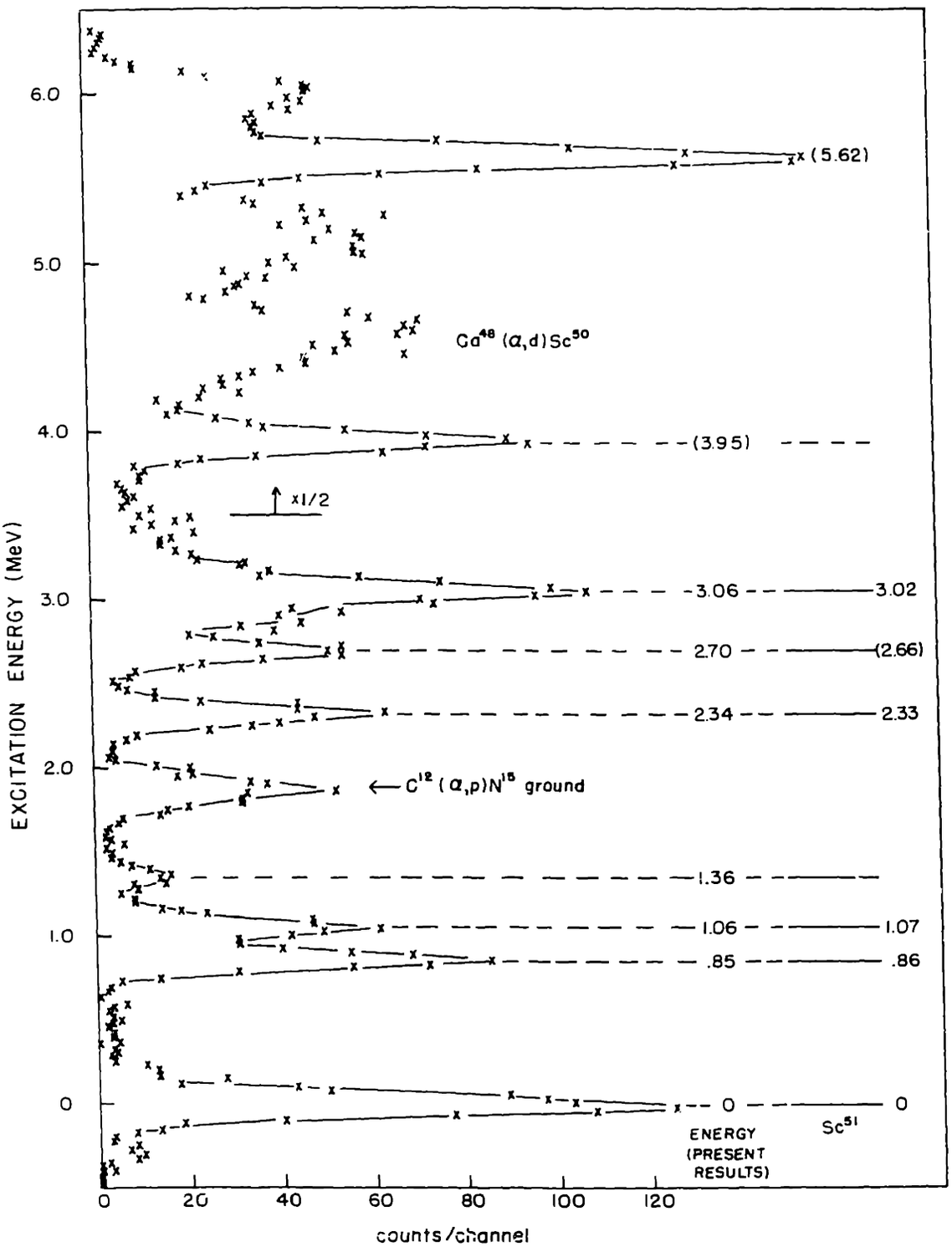

Figure 6.23 $Ca^{48}(\alpha,p)Sc^{51}$ Spectrum at 35°_{LAB} and Sc^{51} Energy Levels

to states in Sc^{51}. However, this is the region where deuteron peaks from the $Ca^{48}(\alpha,p)Sc^{50}$ reaction occur, and there is some doubt that all such peaks were eliminated by the simple method of particle identification used (see Section 3.1). Further work will be done using better particle identification and no definite conclusions about these states will be made until the new results are available.

As explained in Section 6.2.3, the angular distribution for the $Ca^{48}(\alpha,p)Sc^{51}$ ground state transition could not be satisfactorily accounted for using the present DWBA calculations. In addition, the calculation for the transfered neutrons coupled to spins other than zero could only be carried out for 1f neutrons (using the form factor code at M.I.T.). Therefore, no meaningful calculations are available at present for the (α,p) reaction to the excited states in Sc^{51}.

However, from the experimental similarity between the $Ca^{48}(\alpha,p)Sc^{51}$ ground state angular distribution and those for the other nuclei studied (see Figure 6.1) it seems possible that the difference in neutron configurations may not significantly affect the shapes of the (α,p) angular distributions to excited states. Thus, whenever possible, the $Ca^{48}(\alpha,p)Sc^{51}$ angular distributions will be compared to those (from other nuclei) which are similar in shape. The spin assignments suggested by this procedure must be regarded as uncertain.

One such comparison is shown in Figure 6.24 for the 0.85 Mev state in Sc^{51}. The other four states whose (α,p) angular distributions are shown in Figure 6.24 are all assumed to have spin and parity 3/2-. The similarity between these curves suggests that the 0.85 Mev state may have $J\pi = 3/2-$.

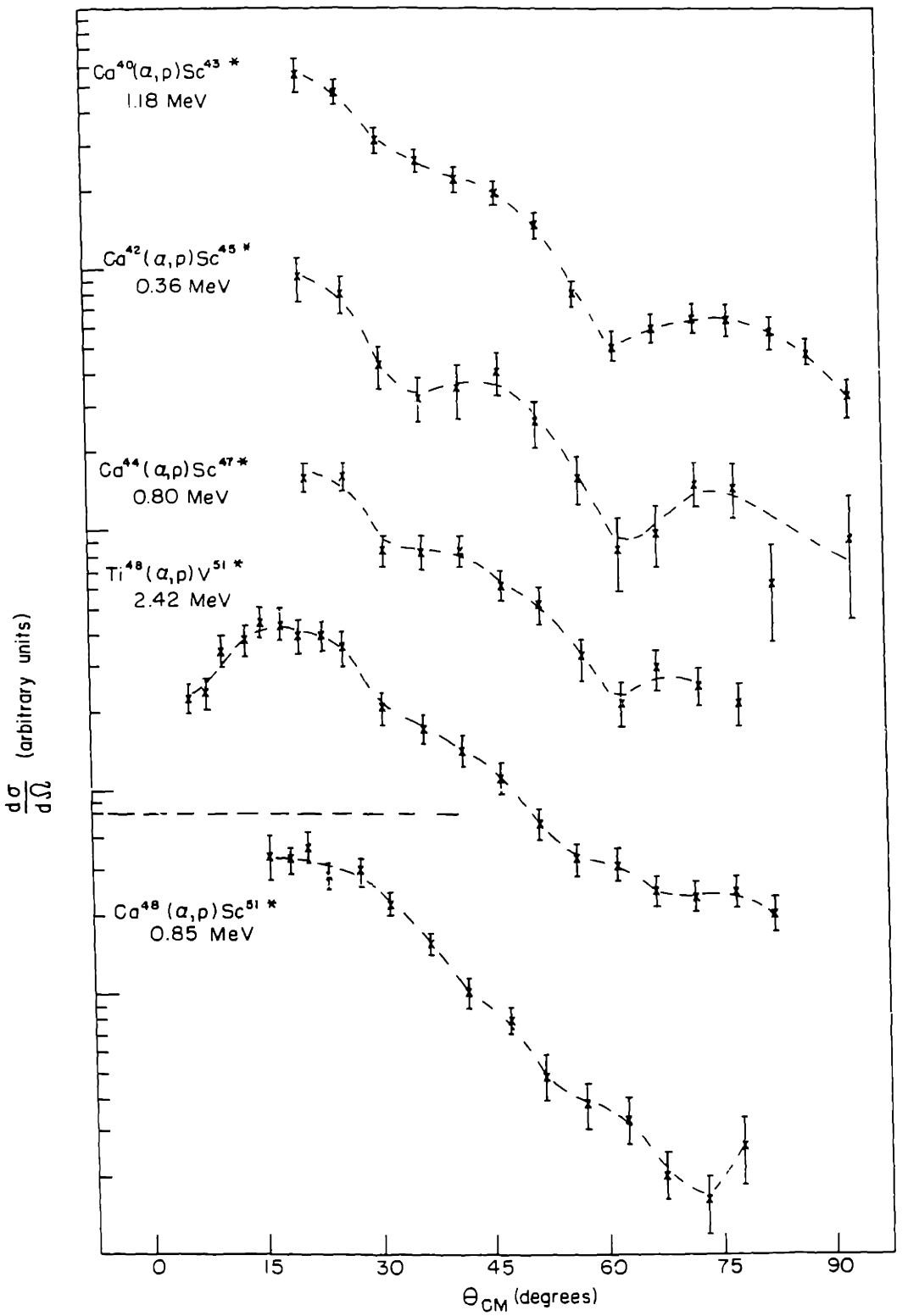

Figure 6.24 Experimental $J^{\pi} = 3/2^{-}$ Angular Distributions

The angular distribution for the 0.85 Mev state in Sc^{51} is shown again in Figure 6.25 with those for the 2.70 Mev and 3.06 Mev states. The similarity between the angular distributions for the 0.85 Mev and 2.70 Mev states suggests that they may have the same spin and parity. No conclusions were drawn for the 3.06 Mev state, since the angular distribution is not very similar to any for which spin assignments were suggested.

The angular distribution for the 1.06 Mev state in Sc^{51} was found to be very similar to that for the 2.62 Mev state in Sc^{43}. Both curves are shown in Figure 6.26. The Sc^{43} 2.62 Mev state was assigned L = 5, but with some uncertainty since no known 11/2- or 9/2- experimental (α,p) or (p,α) angular distributions are available for comparison (see Section 6.3.4 and Figure 6.20).

Also shown in Figure 6.26 is the differential cross-section for the 2.34 Mev state in Sc^{51}. The pronounced oscillatory structure of this cross-section is suggestive of the calculated curve for $J\pi = \frac{1}{2}-$ (see Figure 6.4 and Section 6.3.1). In this respect, the angular distribution is somewhat similar to those for the 2.98 Mev state in Sc^{43} (Figure 6.21) and the 4.18 Mev state in V^{51} (Figure 6.4).

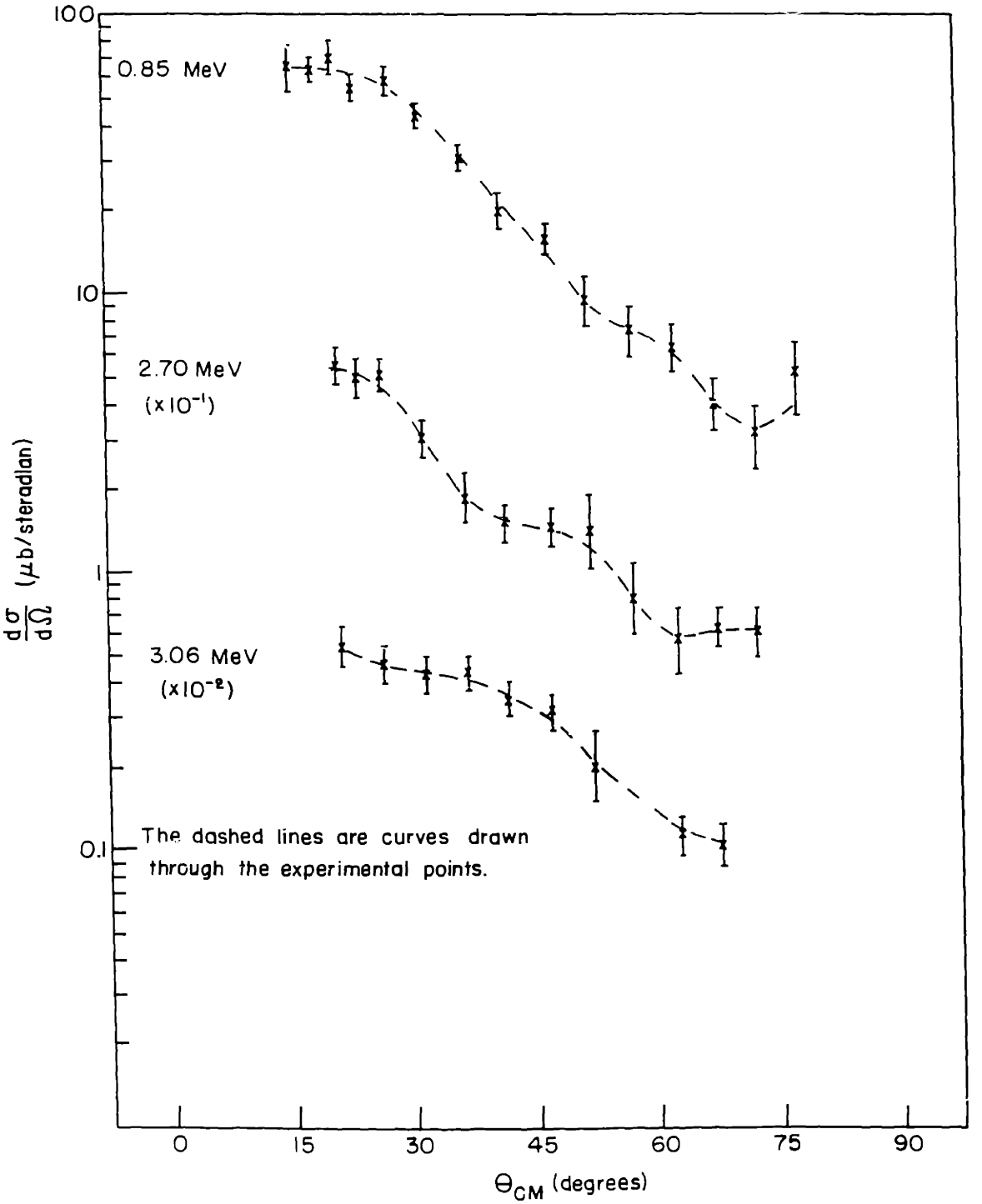

Figure 6.25 $Ca^{48}(\alpha,p)Sc^{51*}$ Differential Cross-Sections

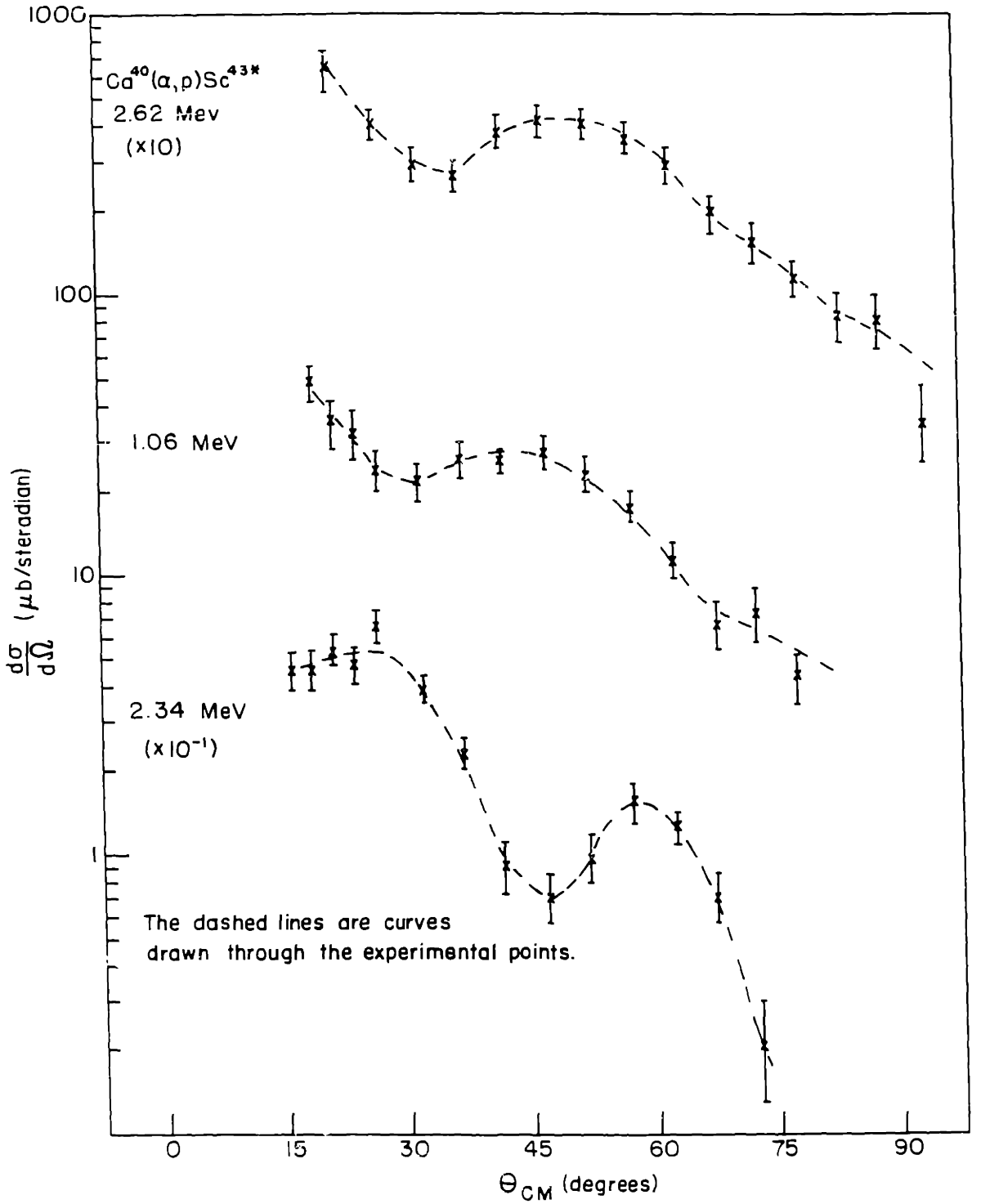

Figure 6.26 $Ca^{48}(\alpha,p)Sc^{51*}$ Differential Cross-Sections

CHAPTER 7

CONCLUSIONS

Presented in this chapter are some of the more general conclusions based on the present study of the (α,p) reaction on Ca^{40}, Ca^{42}, Ca^{44}, Ca^{48} and Ti^{48}, at an alpha particle energy of 30.8 Mev. Some of the experimental evidence for each conclusion will be mentioned in this chapter but more details can be found in chapter 6. The conclusions regarding the nature of the (α,p) reaction are supported by the extent to which the present results agree with the predictions of the (α,p) model discussed in chapter 5. Therefore, the important aspects of the model will be reviewed here.

The model, originated by B. F. Bayman and E. Rost, was based on the assumption that the two neutrons and the proton, transferred during the (α,p) reaction, were stripped from the incident alpha particle and entered shell model orbitals to form the final nucleus. In order to use a standard DWBA code (JULIE), several simplifying assumptions were made. It was assumed that the interaction involved in the (α,p) reaction depends only on the separation between the proton and the center of mass of the transferred triton cluster. Also, oscillator wave functions were assumed for the transferred nucleons, and a simple wave function was used for the alpha particle. Finally, the zero range approximation was used.

The calculations of the triton cluster wave function were performed by integrating out the relative coordinates of the product of the three oscillator wave functions and the alpha particle wave function. The resultant form factor was used as input to the DWBA code JULIE.

The (α,p) spectroscopic factors were calculated using two types of wave functions for the target and final nuclei. The first type was based

on the assumption that the neutrons and protons were separately in states of good seniority. The other wave functions used were the shell model wave functions of MBZ (M1).

The two most basic assumptions inherent in the above theory are: (1) that the (α,p) reaction proceeds by a direct reaction and not by the formation of a compound nucleus, and (2) that the mechanism for the reaction is stripping and not knockout (i.e. the incident α particle interacting with a proton in the target, ejecting it, and subsequently being captured). The strong forward peaking in the cross-sections observed in the present experiment is characteristic of direct reaction processes. Also, the similarity between the five ground state angular distributions and the non-excitation of the proton seniority 3 states in V^{51} (in agreement with the direct interaction model), provide further evidence that compound nuclear contributions to the present (α,p) cross-sections are small. The assumption that stripping is the dominant reaction mechanism is supported by the weak excitation of the hole states is Sc^{43}, Sc^{45}, and Sc^{47} by the (α,p) reaction. In addition, the stripping model predictions for the relative magnitudes of the ground state (α,p) cross-sections are in good agreement with the experimental results for the $f_{7/2}$ shell nuclei. For the $Ca^{48}(\alpha,p)Sc^{51}$ ground state transition the agreement is not too good, but this transition may be affected by coherent contributions from different neutron shells.

For the $f_{7/2}$ shell ground state transitions, both the good seniority and the MBZ spectroscopic factors were compared to the experimental results. For the Ca^{42} and Ca^{44} targets (relative to Ti^{48}) the two models gave the same predictions. For Ca^{40}, the MBZ spectroscopic factor was a factor of 1.4 larger than the good seniority one, and the agreement with experiment was improved by using the MBZ wave function for Sc^{43}.

Essentially the same model as used here has been applied to (p,α) reactions in the $f_{7/2}$ shell by Sherr et al. (S4) and to Y^{89} and Zr^{90} by Fulmer and Ball (F2). They obtained satisfactory agreement with the experimental results which were therefore interpreted as being consistent with triton pickup as the dominant mechanism for direct interaction (p,α) reactions at 18–22 Mev.

The DWBA calculations gave satisfactory fits to the $f_{7/2}$ shell ground state ($J\pi = 7/2-$) angular distributions observed in this experiment. The oscillator parameter for the transferred nucleon wave functions was chosen to give the best fit to the $Ca^{40}(\alpha,p)Sc^{43}$ ground state angular distribution. The present $L = 1$ calculations showed a pronounced J dependence similar to that observed by Lee et al. (L5) and Nolan (N3). The 3/2− curves were rather smooth, and the $\frac{1}{2}-$ ones showed pronounced oscillations in angle. Several experimental angular distributions, for states suspected of having spin and parity 3/2−, were found to be quite similar to the $J\pi = 3/2-$ calculations. Also, several angular distributions were observed which had pronounced oscillatory structure, similar to that calculated for $J\pi = \frac{1}{2}-$, but since no other evidence was available for the states involved, the spin assignments were considered uncertain.

The present calculations for $L = 3$ showed little J dependence, and those for $L = 5$ showed almost no J dependence. Experimental angular distributions were found which were similar to the calculations for $J\pi = 5/2-$ and $\frac{11}{2}-$ or 9/2−, but since there was no conclusive evidence supporting the spin assignments they were regarded as uncertain.

The (α,p) spectra for the five nuclei studied in this experiment showed an interesting variation with the number of neutrons in the unfilled shell. For the closed neutron shell targets, Ca^{40} and Ca^{48}, many low lying levels in Sc^{43} and Sc^{51} were strongly excited by the (α,p) reaction. For

the $Ca^{42}(\alpha,p)Sc^{45}$ reaction, with two neutrons in the target $f_{7/2}$ shell, many low lying levels were apparent in the (α,p) spectrum but they were all considerably weaker than the ground state transition. Also, many fairly strong states were seen at higher excitation energies, the lowest being at about 3 Mev excitation. In Sc^{47}, with 6 neutrons in the $f_{7/2}$ shell, only one state (besides the ground state) below 2.9 Mev was significantly excited by the (α,p) reaction. Above 2.9 Mev a few states were excited with almost the same intensity as the ground state. In V^{51}, where the final neutron shell is closed, no states between the ground state and 2.42 Mev were significantly excited by the (α,p) reaction. At 2.42 Mev a state was excited with about the same intensity as the ground state, and several higher states were strongly excited also. Thus we see that, as the final $f_{7/2}$ neutron shell fills, the main strength of the (α,p) reaction shifts from the low lying states to higher states (above about 2.4-3 Mev).

This experimental trend of the (α,p) strength to low lying states is in excellent qualitative agreement with the calculations for $f_{7/2}$ shell excited states. The theoretical (α,p) spectra presented in chapter 6 were calculated using MBZ wave functions, but for states of spin other than 7/2 the variation of the (α,p) spectroscopic factors with neutron number would be qualitatively the same for any wave functions for pure $f_{7/2}$ shell configurations.

The strongly excited states above about 3 Mev presumably consist mainly of configurations higher than the $f_{7/2}$ shell. Thus, the strong excitation of the higher states and the non-excitation of the low lying states in V^{51} indicate very little mixing of higher configurations in the low lying states (below about 2 Mev). Similarly, the strong excitation of the low lying states in Sc^{43} and the lack of significantly stronger states above a few Mev suggests that there is considerable mixing of the higher

configurations in the low lying Sc^{43} levels. Such mixing would also account for the large number of low lying negative parity states in Sc^{43} compared to the $f_{7/2}$ shell calculations. The negative parity assignments are based on the (α,p) excitation, since hole states (positive parity) are weakly excited by the (α,p) reaction. Thus it appears that there is strong mixing of higher configurations in the low lying states of Sc^{43} and this mixing decreases as the $f_{7/2}$ neutron shell fills. In V^{51} where the $f_{7/2}$ neutron shell is full, no significant mixing in the levels below 2 Mev was observed.

The present study has shown that, despite the possible complexity of the (α,p) reaction, its selectivity makes it a useful tool for nuclear spectroscopy. The coherence of the spectroscopic factors makes the (α,p) reaction useful in determining the relative signs of components of the nuclear wave functions involved, and the pronounced J dependence of the $L=1$ angular distributions makes it useful in assigning spins to $L=1$ states. Finally, the (α,p) reaction was useful also in reaching the nucleus Sc^{51} which is inaccessible by simpler reactions.

BIBLIOGRAPHY

A1 W.P. Alford, private communication

B1 H. Bichsel, R. F. Mozley, and W. A. Aron, Phys. Rev. 105, 1788 (1957)

B2 G. H. Briggs, Rev. Mod. Physics 26, 1 (1954)

B3 B. F. Bayman, private communication

B4 B. F. Bayman, Nuclear Spectroscopy with Direct Reactions, Vol. II, ANL-6878 335 (1964)

B5 B. F. Bayman, F. P. Brady, and R. Sherr, Proceedings of the Rutherford Jubilee International Conference, 533 (1962)

B6 H. W. Broek, J. L. Yntema, B. Buck, and G. R. Satchler, Nucl. Phys. 64, 259 (1965)

B7 R. K. Bansal and J. B. French, Phys. Letters 11, 145 (1964)

B8 R. H. Bassel, G. R. Satchler, R. M. Drisko and E. Rost, Phys. Rev. 128, 2693 (1962)

B9 J. H. Bjerregaard, P. F. Dahl, O. Hansen and G. Sidenius, Nucl. Phys. 51, 641 (1961)

B10 L. Broman and J. Dubois, Nucl. Phys. 72, 529 (1965)

B11 T. A. Belote, A. Sperduto, and W. W. Buechner, Phys. Rev. 139, B80 (1965)

D1 R. M. Drisko, G. R. Satchler and R. H. Bassel, Phys. Letters 5, 347 (1963)

E1 J. R. Erskine and A. Marinov, B.A.P.S. 10, 479 (1965)

E2 J. R. Erskine, A. Marinov, and J. P. Schiffer, Phys. Rev. 142, 633 (1966)

F1 H. Frank, D. Hass and H. Prang, Phys. Letters 19, 391 (1965)

F2 C. B. Fulmer and J. B. Ball, Phys. Rev. 140, B330 (1965)

H1 C. E. Hunting, Ph. D. Thesis, M. I. T., Jan. 1958

H2 R. E. Holland, F. J. Lynch, and K. E. Nysten, Phys. Rev. Letters 13, 241 (1964)

H3 S. Hinds and R. Middleton, Atomic Weapons Research Establishment, Aldemaster, Berkshire, England (unpublished)

H4 C. E. Hunting and N. S. Wall, Phys. Rev. 108, 901 (1957) and Phys. Rev. 115, 956 (1959)

K1 W. J. Kossler, private communication

K2 P. R. Klein, N. Cindro, L. W. Swenson and N. S. Wall, Nucl. Phys. 16, 374 (1960)

L1 M. S. Livingston, J. Appl. Phys. 15, 2 and 128 (1944) and E. P. Lippincott, Ph. D. Thesis, M. I. T., June 1966

L2 E. P. Lippincott, A. Bernstein and G. Sample, private communication, and E. P. Lippincott, Ph. D. Thesis, M. I. T., June 1966

L3 J. C. Legg and E. Rost, PUC - 1963 - 120

L4 L. L. Lee, Jr., J. P. Schiffer, B. Zeidman, G. R. Satchler, R. M. Drisko, and R. H. Bassel, Phys. Rev. 136, B971 (1964)

L5 L. L. Lee, Jr., A. Marinov, C. Mayer-Boricke, J. P. Schiffer, R. H. Bassel, R. M. Drisko, and G. R. Satchler, Phys. Rev. Letters 14, 261 (1965)

L6 N. O. Lassen and Clive Larsen, Nucl. Phys. 42, 183 (1963)

L7 R. D. Lawson and M. H. Macfarlane, Argonne National Laboratory (preprint)

L8 N. O. Lassen and Clive Larsen, Nucl. Phys. 56, 259 (1964)

M1 J. D. McCullen, B. F. Bayman and L. Zamick, Phys. Rev. 134, B515 (1964) and the Princeton University Technical Report NYO-9891

M2 H. J. Mang, UCRL - 8931 Law. Rad. Lab. (1959)

M3 J. H. E. Mattauch, W. Thiele, and A. H. Wapstra, Nucl. Phys. 67, 1 (1965) (1964 Mass Table)

N1 Nuclear Data Sheets (May 1963), compiled by K. Way et al., Printing and Publishing Office, National Academy of Sciences-National Research Council, Washington 25, D. C.

N2 1960 Nuclear Data Tables, Part I, National Academy of Sciences-National Research Council, Washington 25, D. C.

N3 J. A. Nolen, Ph. D. Thesis, Princeton Univ. August 1965

P1 F. G. Perey, Phys. Rev. 131, 745 (1963)

P2 M. S. Plendl, L. J. Defelice, and R. K. Sheline, Nucl. Phys. 73, 131 (1965)

R1 M. K. Ramaswamy, Current Sci. (India) 32, 13 (1963)

S1 R. M. Sternheimer, Phys. Rev. 115, 137 (1959)

S2 E. Segre, Editor, Experimental Nuclear Physics, Vol. I p. 243

S3 G. R. Satchler, Nucl. Phys. 55, 1 (1964)

S4 R. Sherr, Proceedings of the Conference on Direct Interactions and Nuclear Reaction Mechanisms, Padua (Gordon and Breach, New York, 1963) p. 1025

S5 S. Smith, private communication

S6 J. E. Schwager, Phys. Rev. 121, 569 (1961)

S7 J. J. Schwartz and W. P. Alford, Bull. Am. Phys. Soc. 10, 479 (Apr 1965)

S8 R. K. Sheline and K. Windermuth, Nucl. Phys. 21, 196 (1960)

T1 H. T. Tu and N. B. Gove, Ground State Q Values, October 1956 to December 1963 (See reference N1)

T2 A. deShalit and I. Talmi, Nuclear Shell Theory (Academic Press Inc., New York, 1963) pp. 293 and 530

Y1 J. L. Yntema and G. R. Satchler, Phys. Rev. 134, B976 (1964)

Y2 J. L. Yntema and J. R. Erskine, Phys. Letters 12, 26 (1964)

Y3 T. Yamazaki, M. Kondo, and S. Yamabe, J. Phys. Soc. Japan 18, 620 (1963)

Z1 W. H. Barkas and M. J. Berger, Paper No. 7 in Studies in Penetration of Charged Particles in Matter, National Academy of Sciences - National Research Council Publication 1133. p. 103

BIOGRAPHY

The author, Robert O. Ginaven, spent 4 years as an undergraduate at Ohio Wesleyan University where he majored in Physics and minored in Mathematics. He received his B.A. degree in June 1961, graduating fourth in his class. While at Ohio Wesleyan he was a member of Omicron Delta Kappa, Phi Beta Kappa, and Pi Mu Epsilon (Mathematics honorary). He won a Sigma Xi prize for his senior project. In addition he played soccer and lacrosse, receiving varsity letters in each.

After graduation he married another Ohio Wesleyan graduate, Wilhelmina Good, and came to M. I. T. where he remained until the present time (May 1966). He studied under a National Science Foundation fellowship for 4 years and had a research assistantship during the last year. He was elected to Sigma Xi in May 1965. He has two children, a daughter Karen and a son Scott.